Electrical Impedance Tomography/Spectroscopy (EITS)

A Code Division Multiplexed (CDM) Approach

Presented by:

Mohohlo Samuel Tšoeu

Submitted to the Department of Electrical Engineering at the University of Cape Town in fulfillment of the academic requirements for a Degree of Doctor of Philosophy in Electrical Engineering.

Supervisor:

Prof. M. Inggs
Dept. of Electrical and Electronics Engineering
University of Cape Town

November 18, 2016

Declaration

1. I know that plagiarism is wrong. Plagiarism is to use another's work and pretend that it is one's own.
2. I have used the IEEE convention for citation and referencing. Each contribution to, and quotation in, this report from the work(s) of other people has been attributed, and has been cited and referenced.
3. This report is my own work, and has not been submitted to another institution for a Degree.
4. Parts of this report are based on work that has been published in the IEEE Transactions of Biomedical

5. I have not allowed, and will not allow, anyone to copy my work with the intention of passing it off as their own work

Circuits and Systems and IEEE AFRICON 2015.

Tšoeu

M. S.

Signed by candidate

Signature:. . . . . .

List of Publications

[1] M.S. Tsoeu, M.R. Inggs, "Electrical impedance tomography using code division multiplexing," in *AFRICON 2015*, pp.1-5, 14-17 Sept. 2015

[2] M.S. Tsoeu, M.R Inggs, "Fully Parallel Electrical Impedance Tomography Using Code Division Multiplexing," in *IEEE Transactions on Biomedical Circuits and Systems*, vol.10, no.3, pp.556-566, 2016.

Abstract

Electrical Impedance Tomography and Spectroscopy (EITS) is a noninvasive imaging technique that creates images of cross-sections "*tomos*" of objects by discriminating them based on their electrical impedance. This thesis investigated and successfully confirmed the use of Code Division Multiplexing (CDM) using Gold codes in Electrical Impedance Tomography and Spectroscopy. The results obtained showed 3.5% and 6.2% errors in determining the position and size of imaged anomalies respectively, with attainable imaging speed of 462 frames/second. These results are better, compared to those reported when using Time Division Multiplexing (TDM) and Frequency Division Multiplexing (FDM).This new approach provides a more robust mode of EITS for fast changing dynamic systems by eliminating temporal data inconsistencies. Furthermore, it enables robust use of frequency difference imaging and spectroscopy in EITS by eliminating frequency data inconsistencies. In this method of imaging, electric current patterns are safely injected into the imaged object by a set of electrodes arranged in a single plane on the objects surface, for 2-Dimensional (2D) imaging. For 3-Dimensional (3D) imaging, more electrode planes are used on the objects surface. The injected currents result in measurable voltages on the objects surface. Such voltages are measured, and together with the input currents, and a Finite Element Model (FEM) of the object, used to reconstruct an impedance image of the cross-sectional contents of the imaged object. The reconstruction process involves the numerical solutions of the forward problem; using Finite Element solvers and the resulting ill-posed inverse problem using iterative Optimization or Computational Intelligence methods. This method has applications mainly in the Biomedical imaging and Process monitoring fields. The primary interests of the author are, in imaging and diagnosis of cancer, neonatal pneumonia and neurological disorders which are leading causes of death in Africa and world-wide.

Acknowledgements

To my supervisors: gratitude is in order for my academic supervisor Prof. Mike Inggs and former supervisor Prof. J. C. Tapson.

To my family: Thank you all for the support they gave me throughout. You are the reason I have made it this far. *Kea leboha bataung, Molimo ale atisetse mahlohonolo.*

To my friends: Thanks to all of you without specific mention for your undying moral support during the trying period of my PhD. Special thanks to Mphakiseng Masuabi for the constant support and motivation, and for reading and weeding out mistakes in this report.

To the University of Cape Town: I would like to offer my gratitude for giving me the opportunity to pursue my PhD while, developing my career as an Academic at the University.

Contents

List of Figures

List of Tables

Chapter 1

Introduction

This chapter provides a brief motivation for conducting the research work in this thesis. The motivation cites applications of this work and their importance in both biomedical and industrial realms. A short review of literature around the research field is given to put the research hypothesis, objectives, questions and limitations, that follow, in context. Thereafter, the chapter presents a summary of the methodology employed. A section discussing the contributions of this work and lastly an outline of this thesis document are presented.

1.1 Electrical Impedance Tomography

Electrical Impedance Tomography (EIT) is a form of imaging used for biomedical and process imaging. Medical Imaging is an integral part of diagnosing injury, physiological changes and monitoring of medication given to patients. It provides position, size and shape information about internal contents of a subject. These may be organs or anomalous tissue, such as: cancer tumors and blood clots. Some of the most common forms of imaging are: X-ray, Computed Tomography (CT), Magnetic Resonance Imaging (MRI), Electrical Tomography [1] and Ultrasound. Most of the former techniques are slow and utilize large machinery that are not ideal for on-the-go use such as in ambulances. EITS provides a unique imaging tool from the other methods, since it is the only method that provides information about the electrical impedance of objects.

Electrical Tomography take one of four modalities being Electrical Resistance Tomography (ERT), Electrical Capacitance Tomography (ECT), Electromagnetic Inductance (EMT)

and Impedance Tomography. In each of these imaging methods, an electrical property of the constituents of some object is used to create a distribution map of that property across the cross-section of the entity. These are conductivity, permittivity, permeability, and a combination of the first two giving rise to impedance [1; 2; 3]. Spectroscopy on the other hand, exploits the frequency dependence of object impedances to discriminate them.

The different modalities have their advantages and disadvantages, but EIT is by far the most advantageous and generic method. ERT is the simplest and requires minimal electronic instrumentation. However, this method does not allow the use of Spectroscopy and frequency difference imaging, as resistance is independent of frequency. ECT solves some of the problems posed by ERT. EIT combines both modes at the expense of complex electronics instrumentation.

In EITS, electrodes are placed along a cross-section of the imaged object. Some or all of these electrodes are used for injecting known current patterns into the object, while some or all are used for measuring resulting surface voltages. Figure 1.1 shows a configuration where 15 currents referenced to ground are applied on single electrodes (odd numbered electrodes) and resulting differential surface voltages are measured between each pair of even numbered electrodes. All the injected currents are returned through a single grounded electrode.

The geometry of the object, the location of the electrodes, the injected currents and measured surface voltages are then used to determine the distribution of the electrical property of the object in the plane of the cross-section. This is achieved using Finite Difference (FD) or Finite Element Methods (FEM) to solve the Partial Differential Equation (PDE), that governs the electromagnetic behavior inside and on the boundary of the imaged object, and using reconstruction algorithm s that solve the resulting inverse problem. While any number of electrodes can be used in EIT, it is common practice to use 8, 16, 32 and 64 . . . electrodes in tomography systems, and the spatial resolution of reconstructed images improves with increasing number of electrodes.

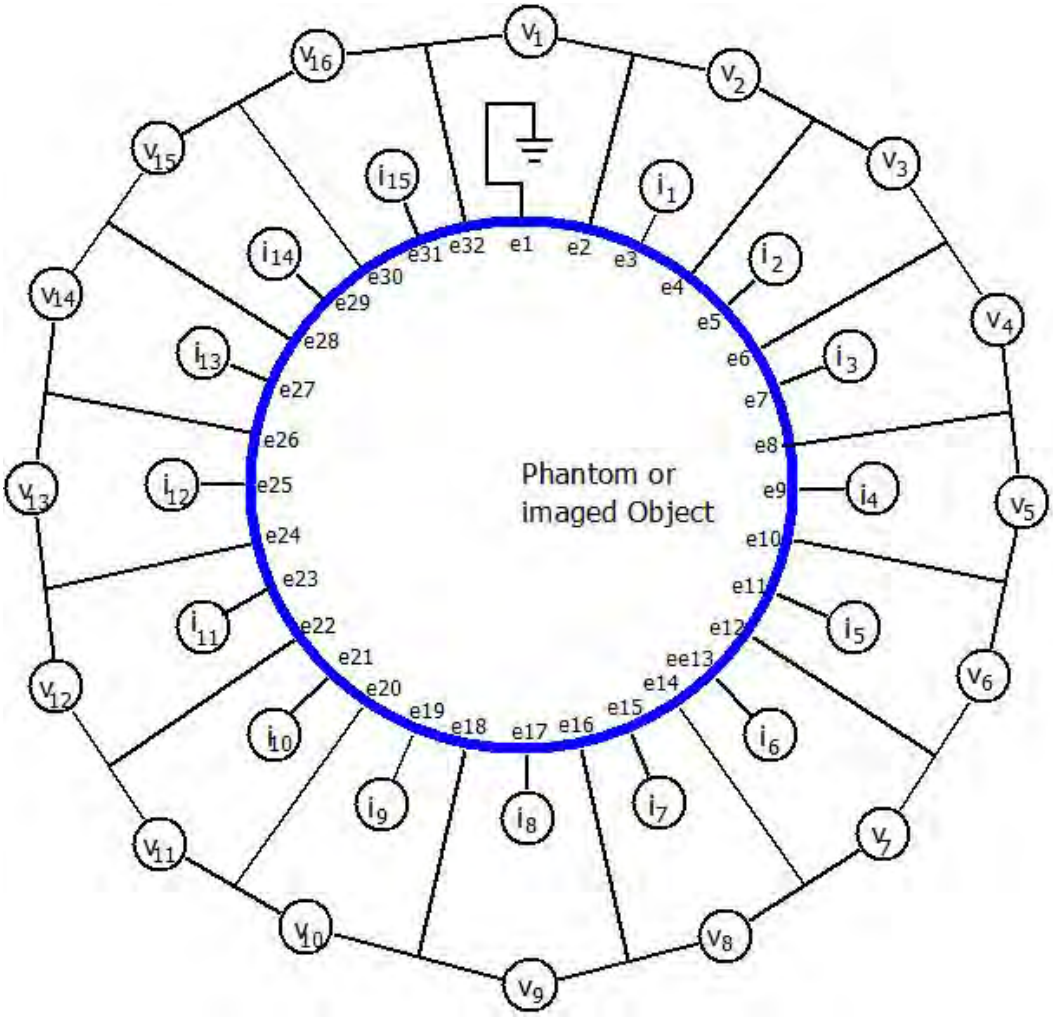

Figure 1.1: A EITS configuration showing simultaneous single electrode current injections (odd electrodes), with a single grounded current return path and simultaneous differential voltage measurements between all even numbered electrodes.

If one cross-section is used a 2-Dimensional (2D) system results. Otherwise, if more cross-sections are interrogated, a 3-Dimensional (3D) implementations of EITS is realized. Both 2D and 3D implementations have been successfully researched and reported [1; 4]. Static applications of EIT collect a single set of measurements to create the distribution image, and have also been successful. Difference methods require a reference measurement, which is subtracted from another measurement taken at a different time or frequency to reconstruct a distribution of admittivity, conductivity or permittivity changes. Dynamic applications of EITS are those concerned with imaging changes in objects. These pose a challenge regarding required image frame rates to cope with the rate of change of the imaged objects.

The attainable frame rates are limited by a number of factors, namely: data acquisition

multiple access schemes used, bandwidth of used electronics, and speed of reconstructing EIT images. The first factor is of prime interest to the research work proposed in this thesis. Previous applications, research and published works have to the best of the authors knowledge all focused on two main multiple access methods which are, Time Division Multiplexing (TDM) and Frequency Division Multiplexing (FDM). In the application of TDM Wilkinson and colleagues reported an Electrical Resistance Tomography (ERT) system that could capture and process 1000 frames/second using one iteration of the Newton-Raphson reconstruction algorithm [4]. FDM was reported by [2; 5], with up to 280 frames/second. The challenges facing EITS systems are: inaccurate and low bandwidth electronics instrumentation, slow reconstruction software, and the ill-posed nature of the reconstruction problem arising, which result in errors and lower spatial resolution of images compared to other imaging modalities such as X-ray, Magnetic Resonance Imaging (MRI) and Computed Tomography (CT).

1.2 Multiplexing in EITS

Electrical impedance tomography has received wide research attention, both in the medical imaging field and Process tomography. It has a number of advantages over the other imaging modalities in that, tomography systems used are small in physical size, it is non-intrusive, cost-effective and relatively fast. However, due to the size and budget constraints of the systems, multiplexing has been researched to come up with a method that offers a cost-effective, accurate and high frame rate option. These multiplexing techniques include Time Division Multiplexing (TDM), which allocates time slots to current sources and voltmeters in a mutually exclusive manner. By design this method provides data from excitation currents and surface voltages measured at different times. This introduces temporal data inconsistencies which may deteriorate the accuracy of reconstructed images, especially for fast changing dynamic systems.

The second approach is Frequency Division Multiplexing (FDM). In FDM several non-overlapping frequency bands are allocated to each current source within the allocated bandwidth. It has been found that in general FDM gives higher frame rates of about 280 frames/s in [2], while TDM offers lower frame rates under common implementations. Wilkinson and colleagues reported an optimized Electrical Resistance Tomography used to obtain frame rates of about 1000 frames/s [4]. Because FDM excites different injection electrodes with sinusoidal currents at different frequencies, the measured resultant surface voltages maybe inconsistent if complex impedances (frequency dependent) are imaged. This results in poor reconstruction results, especially if some of the excitations occur on

the amplitude roll-off of the frequency response of the imaged impedances. Another multiple access method is the Code Division Multiplexing (CDM), in which pseudo random (PN) codes are used to modulate the input current patterns. This approach has the benefit of frequency re-use and is popular in communication systems. One reported use of CDM in sensing can be found in [6].

It was observed in [7] that in the vicinity of of 128 kHz, the impedance of a banana was indistinguishable from that of the background saline solution. This means if time difference imaging were to be used with a sinusoidal stimulus signal at 128 kHz, the imaging results would be poor. Electrical Impedance Spectroscopy (EIS) can be used to achieve better results in imaging. This is achieved by sweeping the frequency of the injected excitation signals within some frequency range and making use of the frequency that yields optimum discrimination of contents. Alternatively, multisine inputs can be used to simultaneously inject currents at different frequencies. In addition to that, multiple frequency imaging can be used in difference imaging, as opposed to using measurement sets taken at different times and subtracting them. The sets can be taken at different frequencies of the same spectroscopic data set. This doubles the temporal resolution of EIT, as only one measurement is needed as opposed to two for time difference imaging. Furthermore, this provides a means of difference imaging where time reference measurements are not available. Alternatively, applications in Biomedical Engineering have made use of EIS for tissue identication/classication [8]. Other reported works on EITS can be found in [9; 10].

Works reported to date used TDM and FDM [4; 2; 5]. McEwan *et al* [7], used pseudo-random binary codes on a tomography system for time and frequency difference imaging of a banana object. However, this work does not fully employ the Code Division Multiplexing principle, as it only used two simultaneous codes implemented on a reprogrammed UCL Mark 2.5 system. Gevers and colleagues in [11], used Walsh-Hadamard codes to modulate sinusoidal inputs in their system.

1.3 EITS Reconstruction Methods

Reconstruction methods used in EITS imaging can be grouped into three different classes. The first is static imaging in which only a single voltage measurement set $\mathbf{v}_m$ is required. A Finite Element Model of the imaged object is used with an initial estimate of the admittivity distribution $\gamma(\mathbf{r})$ within the object; where $\mathbf{r} = (x, y, z)$ is a 3-dimensional position of the admittivity, to compute surface voltages $\mathbf{v}_c = \mathbf{f}(\gamma(\mathbf{r}))$. The errors between

computed and measured voltages are used to iteratively update the estimated admittivity distribution with computed increments $\Delta\gamma(\mathbf{r})$, until a chosen measure of error between the computed and measured surface voltages (often the sum of squared errors at each electrode) is minimized below a set level σ. A candidate algorithm that minimizes a scalar cost function (1.3-1) can be used to solve the reconstruction problem. Detailed accounts of alternative reconstruction algorithms can be found in [12; 13; 14].

$$min_{\Delta\gamma(\mathbf{r})} J = \| \mathbf{v}_m - \mathbf{f}(\gamma(\mathbf{r})) \|^2_{\mathbf{Q}} + \| \Delta\gamma(\mathbf{r}) \|^2_{\mathbf{R}} \tag{1.3-1}$$

The set $\Delta\gamma(\mathbf{r})$ that minimizes the cost is then used to update the initial guess of admittivities, and the minimization process is repeated until the error value is below the desired value.

$$\gamma(\mathbf{r}) = \gamma(\mathbf{r}) + \Delta\gamma(\mathbf{r}) \tag{1.3-2}$$

The matrix $\mathbf{Q}$ is a penalty matrix used to emphasize the importance of minimizing the errors at each measurement electrode. The weights are usually chosen based on the calibrated measurement accuracies on the individual measurement electrodes, because it would be unreasonable to require minimization of voltage errors beyond the accuracy of measurement on the respective electrodes. $\mathbf{R}$ is the regularization matrix, that contains prior information to constrain the computed increments $\Delta\gamma(\mathbf{r})$ based on the known geometrical structures. This matrix improves the conditioning of the matrix computations involved in minimizing (1.3-1). A result of this method is an absolute admittivity distribution that is used to create a tomogram in the case of 2-dimensional imaging. The accuracy of this method relies heavily on knowledge of contact impedances between electrodes and the imaged object as well as the prior geometrical information regarding impedance changes. Such knowledge is often not available, overlooked or limited in practical applications. This method provides absolute admittivities which may provide vital information on the imaged object or industrial process. Research reported in [15], presents different models for electrodes to be included in this reconstruction method, placing emphasis on the improved performance offered by the use of the complete electrode model (CEM).

The second approach first measures a reference measured voltage data set $\mathbf{v}_r$, and another data set $\mathbf{v}_m$ acquired after admittivity changes have occurred. The dependence of this approach on temporal changes in admittivity renders it useless in situations where a

reference can not be obtained due to lack of temporal change in admittivity, such as imaging of static biological tissue distribution. The two measurement sets are then subtracted from each other and the difference used with in reconstruction algorithms such as the Sheffield back projection [16], Gauss-Newton [17] and sensitivity method initially proposed by Kotre in [18].

Advantages of this method are that it results in a linearized and simpler reconstruction problem under the assumption of small admittivity changes. Furthermore, the differencing of measured voltage sets alleviates the effects of contact impedances between electrodes and imaged object since they cancel out. The disadvantage is that time-differential data only provides images of temporal changes, which means parts of the imaged object that are static can not be detected even if they have different admittivities such as bone and fatty tissue.

The third method takes a single measurement set, through application of currents that stimulate a range of different frequencies or two data set obtained at different frequencies of excitation currents. The two data sets taken from different frequencies are subtracted from each other and used in a similar manner to $\mathbf{v}_r$, and $\mathbf{v}_m$ in time difference imaging. However, this provides frequency difference imaging since the used measurement sets are obtained at different frequencies (possible at the same time). This approach can identify static admittivities if they have different impedances (frequency dependent) and can be used to locate bones and fatty tissue due to their different frequency responses [19]. The disadvantage and a factor that has been overlooked in most reported works is that subtracting measurement sets at different frequencies no longer alleviates the effects of contact impedances between electrodes and imaged object, as achieved by time difference imaging. This is because such contact impedances are frequency dependent, and it has been reported that if they change by as much as 20%, they can render reconstructed images meaningless [20]. Consequently, the complete electrode model (CEM) has to be used along with a measurement of the electrode contact impedances [15; 21].

A systematic deficiency in most reported research works in EITS is that standardized performance measures that allow comparison among different system implementations and methods are not provided. Proposals of such performance measures have been presented in [22]. Another problem with most simultaneous current injection and voltage measurement systems is that they use different injection and measurement electrodes which increases the total number of used measurement electrodes. This is because the use of the same electrodes for both injection and measurement places stringent performance requirements on each current source used as discussed by Tapson and colleagues [23], along with their proposal of circuits to achieve the task. Some research has placed the blame

of poor performance on electrodes geometrical structure and placement, and conducted research to determine optimal electrodes [24].

1.4 Statement of Hypothesis

The main objectives of this research work are to investigate the application of CDM to Electrical Impedance Tomography/Spectroscopy (EITS). This is based on the hypothesis that, *if orthogonal (or nearly so) pseudo-random binary codes (PN) are simultaneously applied as excitation current to the electrodes of a tomograph, and respective voltages are measured, the cross-correlations of the injected PRN code currents and measured voltages will give the impulse responses, whose fast Fourier transforms can be used to reconstruct images of complex impedances of the imaged object contents.* Such object characterizing information will provide direct frequency response data of the contents of the object for contents classification and monitoring. Frequency difference imaging is also an important aspect of this approach, allowing diagnostics that can not be performed where baseline conductivity data of contents is not available, such as in stroke patients [25]. This approach is also followed due to its ability to inject higher excitation signal energies, evenly distributed over the bandwidth of a broadband EITS system. The method can achieve high frame rates, and better discrimination at multiple frequencies. In order to confirm this hypothesis, the following questions have to be answered:

1. Can simultaneously injected pseudo-random binary codes be used to extract usable channel impulse response (impedance) data in a shared medium (phantom) that can provide enough information to enable reconstruction of impedance distribution within the phantom?
2. Can impulse responses from imaging biological specimen provide enough impedance variation with frequency to enable frequency difference imaging?
3. Will the developed EITS system enable spectroscopy and wide-band EIT?
4. What imaging quality is attainable through CDM EITS as compared to TDM and FDM?
5. What are the achievable advantages and disadvantages of CDM EITS over TDM and FDM if any?

A fully functional 16 electrode Tomography system using CDM and capable of capturing at least 10 image frames per second has to be designed and implemented. Phantom tests

to verify the functionality of the developed system have to be performed. An approach for computing standard performance measures on reconstructed images using only the actual .jpeg or .png etc. images and not the raw reconstruction data should be developed to allow comparison of the developed system and other reported works.

1.5 Contributions

While code division multiplexing (CDM) and system identification using pseudo-random binary codes have been used in Communications and Control Systems Engineering, these concepts have not been deployed on a complete simultaneous current injection and voltage measurement system before. This work extends these concepts in that manner and provides proof of their applicability as well as uncovering some of the challenges, weaknesses and advantages when compared to the currently used TDM and FDM. Using TDM, it is possible to inject either a *chirp*, or pseudo-random code signals in a manner reported in [26] and [7]. However, TDM produces low frame rates due to its sequential manner of current injection. It is established in this research that the use of CDM in EIT for simultaneous injection of currents increases the speed of imaging, and provides an alternative to TDM. The injection of a *chirp* signal using TDM can be used for wide-band spectroscopy as reported in [26].

For fast changing dynamic imaging applications however, the serial injection of the stimulus signal captures the system data in different times for each separate injection. The time lag between injections of a single data set collection can introduce temporal inconsistencies that may render TDM based spectroscopy useless in such fast changing systems. Due to the simultaneous nature in which injection is done in the current work, and its ability to achieve spectroscopy, such temporal data inconsistencies are eliminated making it ideal for spectroscopy on fast changing systems.

FDM provides a means of achieving simultaneous injection of currents. However, such currents being injected at different frequencies means they excite different sections of the frequency spectra of the imaged object contents. If these frequencies are selected over a range of frequencies in which the impedances of the contents change drastically, this introduces data inconsistencies (spectral) between different channels which can result in poor imaging quality. However, because CDM allows frequency re-use among all channels, all the injected currents in CDM EITS excite the same frequency range resulting in consistent measurements data.

1.6 Limitations

While the motivation for this study was to develop a device that can be used for Biomedical imaging, it is beyond the scope of this work to take the study to human testing. The tomography system developed in this work is aimed at verifying the research hypothesis. It is not intended to be the best design in terms of hardware capabilities, as it is limited by budget constraints. Part of the study investigates possible applications of the device, but it is not part of the scope that such applications be pursued. The performance of the ultimate device depends heavily on reconstruction methods used, it is however, not an objective of this study to develop new reconstruction tools and software, but rather to use and integrate existing ones if available. Some parts of this study which are mechanical in nature may be outsourced as they fall outside the author's area of expertise.

1.7 Research Approach

To the author's knowledge at the present time there is no reported, fully functional wide band CDM tomograph system using simultaneous Gold codes current injection and measurement of surface voltages. Tapson and colleagues [27] implemented a two electrode serial injection tomograph using the UCL Mk 2.5 platform reprogrammed to produce two gold codes. In this study, a 32 electrode CDM tomograph was designed and constructed. This system was interfaced with a saline phantom for phantom testing. Gevers and colleagues [11] reported a narrow-band system which used Walsh-Hadamard codes to modulate a sinusoidal excitation input on 8 simultaneous current injection electrodes. Their system provides improved interference immunity between different inputs. However, due to the fact that the used codes do not have Dirac delta auto-correlation, they are not ideal for the CDM approach presented and tested in this research work.

The complete system was calibrated using a homogeneous saline solution in the phantom to enable Time Difference (TD) imaging. Experiments were performed by placing an object inside the phantom filled with a saline solution, and both homogeneous and inhomogeneous data sets measured at different time instances. These data sets were used for time difference and frequency difference imaging. The imaging results obtained were compared to results of equivalent FDM and TDM tomography systems reported in literature, through a set of defined performance indices. Figure 1.2 shows the author's mind map and break-down of activities in conducting the research work and Figure 1.3

shows a critical path analysis. Simulations of a full CDM EIT system were performed as proof of concept for the proposed simultaneous current injection and voltage measurement system. The simulations were done using the EIDORS software [28] running on MATLAB. Analysis of the resulting images was done and comparisons made between them and reported results of EIT systems.

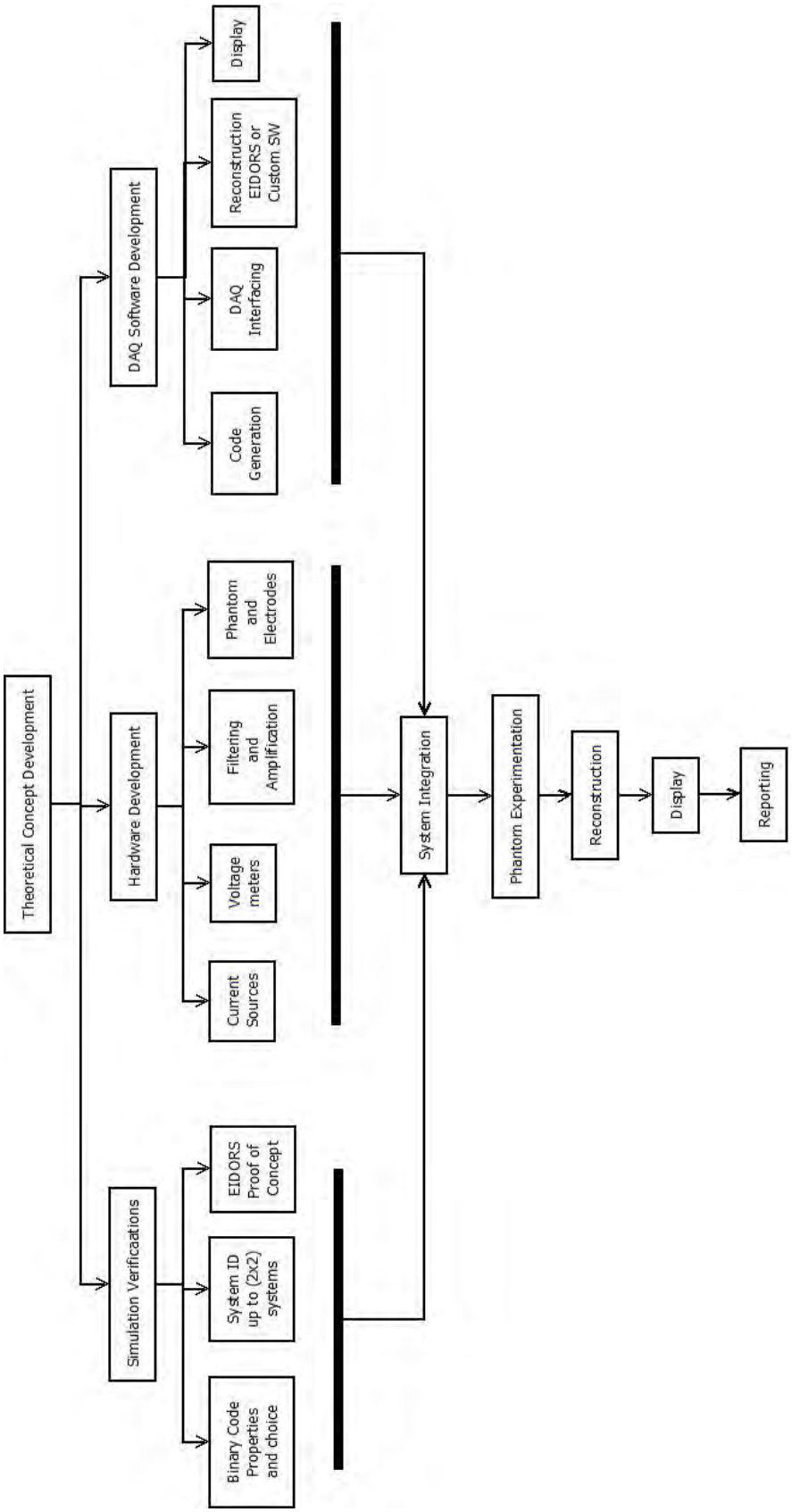

Figure 1.2: Figure shows the plan of activities and how they combine to produce the ultimate answer to hypothesis.

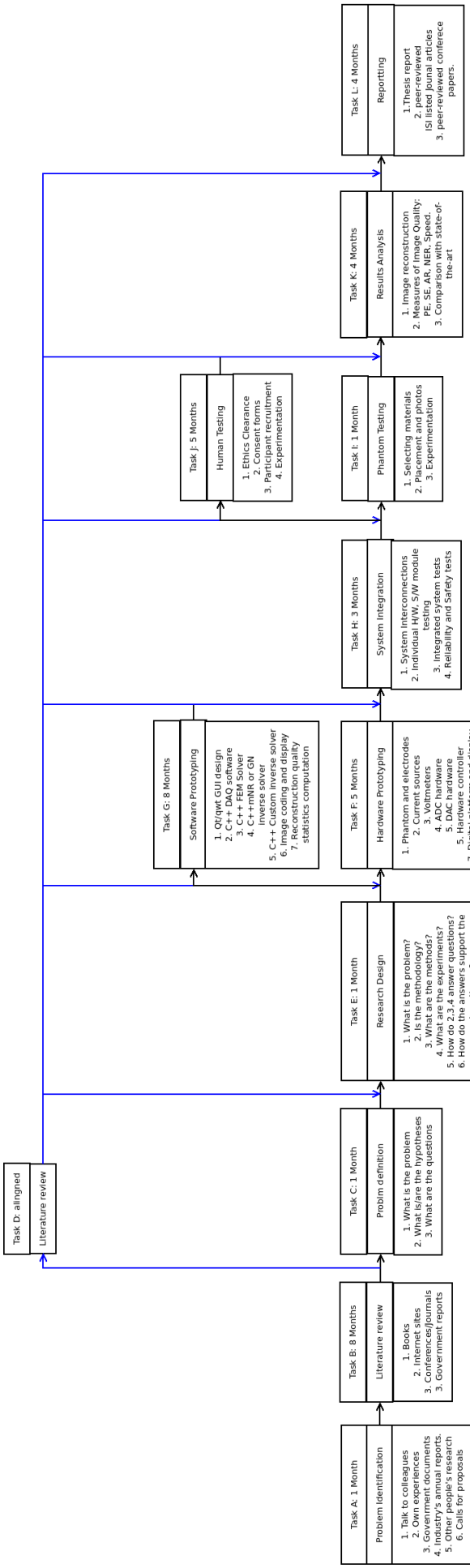

Figure 1.3: A critical path of the research project showing different tasks of the project and details involved at each stage. The project is projected to take 35 months when performed on a full-time basis.

1.8 Thesis Organization

Chapter 1 - Introduction
This chapter gives a brief account of the theory of EITS, and presents the hypothesis statement, research questions, objectives and limitations of this research work. The problem of simultaneously exciting the imaged object with equal bandwidth, broadband current patterns is presented. Such current patterns are proposed in the hypothesis to be pseudo-random binary codes used in a Code Division Multiplexed manner. To confirm the hypothesis, a plan to develop a prototype hardware and software tomography system is presented, along with a research approach and contributions of the research work.

Chapter 2 - Electrical Impedance Tomography/Spectroscopy (EITS)
This chapter is aimed at broadly introducing the field of Impedance Tomography with emphasis on its variants, and extensions to Spectroscopy (EITS). The different forms of electrical tomography: ERT, ECT and EIT are qualitatively explained. The simplicity of ERT and its inability to provide frequency-difference imaging and spectroscopy are discussed. Configurations of ECT and EIT and explanations of how they addresses the limitations of ERT are also given. EITS which is a hybrid of ERT and ECT is discussed, with its major disadvantage being the increased number of electrodes and complex electronics. The chapter further presents different multiplexing methods used in EITS, their advantages and limitations. TDM and FDM are reviewed along with their inherent temporal and frequency data inconsistencies, which motivate the investigation of this study.

Biomedical safety and conformance standards critical in the biomedical application of EITS are given in this chapter. Discussions of the instrumentation configuration used in EITS systems are presented and the details of the subsystems that may be used in designing and integrating the hardware system covered. The preferred four-electrode impedance measurement system is discussed and its disadvantage of increasing the number of electrodes. For simultaneous current injection, a challenge of ring connected current sources arises. This problem imposes stringent requirements on the design of such sources and contributes towards low quality of attainable results in EITS, along with the effects of parasitic electronic components, signal-to-noise ratio and attainable bandwidth. The discussions of electronic instrumentation in this chapter are mainly based on the popular, current injection and voltage measurement type of tomography system. Choices of materials used to make electrodes and their geometrical structures are discussed. The choice and structure of these electrodes is based on their conductivity, corrosion resistance and to avoid injecting toxic metal ions into the imaged subject.

A mathematical formulation of the Elliptic partial differential equations (PDE) that govern the EITS problem, discussions of the Finite Difference Method and Finite Element Method used in solving the resulting PDE (forward problem) are presented. These are followed by the algorithms used to compute the impedance image of the imaged object from the forward solution, the measured surface voltages and geometrical data of the hardware system (inverse problem). Popular algorithm used for the inverse problem are: the Newton-Raphson, back-projection, sensitivity method and Neural networks. Overviews of how these algorithms work and their salient strengths and weaknesses are presented as a prelude to the choice of the algorithm to be used in this work.

Chapter 3 - The Proposed Approach: CDM EITS
This chapter presents the formulations of EITS using CDM, on which the fully parallel EITS system developed in this Thesis is based. These confirm that theoretically it is possible to extract impulse responses of input-output channels on the tomography systems, and that they can be used to reconstruct EITS images. In addition to these formulations, a presentation of the mathematical models (Poisson equation and boundary conditions) governing the EITS problem is given. Formulations of a Finite Element (FEM) solution method for solution of the governing PDE is also given in this chapter. FEM offers accurate solutions of the *weak form*, without strict smoothness requirements on the trial solutions. Furthermore, FEM can model irregular boundaries accurately through the use of small, isoparametric elements. Finally, a presentation of the algorithm used to reconstruct the admittivity images is provided. This is a modified version of the Newton-Raphson method that includes regularization using prior information and error weighting based on the noise-error-ratios on each measurement electrode of the tomography system. While the presented formulations have already been published by the author and his former supervisor, this research is the first confirmation of these concept, using a broadband simultaneous injection EITS system.

The research is classified under applied quantitative research, that requires the design of an experimental tomography prototype, simulations of the proposed method and experimentation for data generation. This chapter gives details of performance measures that are used to compare the developed method with other reported EIT approaches: TDM and FDM. These performance measures are the size error (SE), position error (PE), amplitude response (AR), noise-error-ratio (NER), shape deformation, detectability, frame rate, ringing, distinguishability, repeatability, accuracy, reciprocity, and low frequency drift. These provide a standard platform for comparison of different EIT systems, despite their infrequent of use in previously reported works.

Chapter 4 - Simulations and proof of concepts

Here simulations that confirm the hypothesis of this research work are reported. Properties of pseudo-random binary codes are discussed and their use tested on simple system identification problems. The lack of sufficient numbers of maximal length and small set of Kasami codes of the same length, non-impulse auto-correlation and perfect cross correlation properties of Walsh-Hadamard codes are also discussed. Gold codes are discussed and found to be good compromise codes due to their correlation properties, multiplicity of codes with the same length and ease of processing. Simulation results of EITS using Gold codes are presented and analyzed. These simulations confirm the hypothesis and are found comparable to reported works using FDM and TDM. Simulation results show 9.7% position error, 18.7% size error, 26.4% noise-error-ratio, and 17.6% distinguishability. This chapter is based on a paper presented in the IEEE AFRICON 2015 conference [29].

Chapter 5 - EITS System Design

This chapter documents the design of the prototype EITS system (hardware and software) that is used in this investigation. The needs for a new device, functional and non-functional requirements are given. These include: the sampling rates, bit resolution of data acquisition devices at more than 16 bits, signal levels and compliance at 0.1 mA for injected currents and 10V for measured voltages and number of electrodes. Furthermore, design concepts using different technologies such as microprocessors, FPGA, special purpose data acquisition cards, personal computers and industrial computers are presented. Based on their ability to meet the technical specifications, complexity, cost and portability, these concepts are compared. A prototype concept using special purpose data acquisition cards is chosen for this work, and a more expensive concept that offers the best technical performance based on an FPGA, industrial computer system is chosen for ultimate implementation beyond the scope of this Thesis.

Chapter 6 - EITS System Testing

The designed system is tested for proper performance in this chapter and its limitations and possible improvements discussed. Measurement noise levels are analyzed and found acceptable at 25% of the smallest anticipated measurement and 0.25% of the voltage compliance of the system. Ghosting due to the multiplexed and high frequency nature of the system is also reported in this chapter with possible remedies, and effects on attainable performance. Phantom tests are performed using the prototype system and results and presented. Several biological objects are successfully imaged in a saline phantom. Different Gold code lengths are also investigated in an effort to increase imaging speed but it is found and reported in this chapter that shorter codes result in lower quality results. The effects of the chosen current injection protocol, using one

ground electrode is discussed, and its uneven current density distribution pointed out. Frequency difference imaging was also successfully experimented, but showed limitations due to the low bandwidth of the electronics hardware used. In general this chapter reports successful functionality of the proposed method using Gold codes in CDM for a broadband EITS system.

Chapter 7 - Results Analysis and Discussions

In this chapter, results of phantom tests performed are analyzed to extract some of the performance measures used to compare CDM EITS using Gold codes to other EIT modalities namely: TDM and FDM. The findings of this chapter have been published in a Journal article, in the IEEE Transactions of Biomedical Circuits and Systems [30]. Analysis reveals that the method proposed here yields results that are better than most reported works as follows: 3.5% position error, 6.2% size error, 31.3% noise-error-ratio, and 13.7% distinguishability. The hardware used in this work was low cost and significantly impaired the performance of the system compared to most reported works. Frequency difference imaging results analysis presented in this chapter confirmed its successful use in CDM EITS, with 4.9% position error, 11.5% size error and 30.4% noise-error-ratio, but also revealed the need for higher hardware bandwidth, which was not available due to budget constraints. The proposed simple image processing approach of extracting performance measures presented in the Simulations chapter is also successfully used in this chapter. Analyses presented in this chapter provide concrete answers to the research questions and confirm the Thesis hypothesis.

Chapter 8 - Conclusions

Conclusions are drawn based on the obtained results and discussions presented in Chapters 3 to 7. These conclusions are drawn in line with the hypothesis, questions and objectives of this research work articulated in the Introduction chapter. Based on the findings of this research, recommendations for improvement and future work activities are also given in this chapter. All the questions of this research are answered positively through simulation, experimentation and results analysis. The only question with an implied answer is that of use of CDM EITS for spectroscopy. This is due to the fact that the low cost prototype system used did not provide enough bandwidth to enable conclusive assertion. The conclusions state a confirmation of the hypothesis, that indeed simultaneous injection of pseudo-random binary (Gold) codes can be used to extract data necessary to reconstruct impedance images of subjects. However, injection of multiple codes suffers from cumulative errors, due to cross-correlation non-idealities. Recommendations and directions for further work are to implement a fully functional high bandwidth system with higher bit resolution for data acquisition, and to investigate methods of reducing the errors arising in signal processing (correlation) and acquisition (noise and ghosting).

Chapter 2

Electrical Impedance Tomography/Spectroscopy (EITS)

This chapter gives a qualitative description of Electrical Impedance Tomography and its workings. Different modalities: Electrical Resistance Tomography (ERT), Electrical Capacitance Tomography (ECT), and Electrical Impedance Tomography/Spectroscopy (EITS) are discussed. Their advantages, weaknesses and reported applications are given. These are presented here to provide context within which the proposed method is developed. Different modalities and technologies of EITS may be preferable based on the intended applications.

Electronic instrumentation used in the design of Tomographs is a first integral part towards a working system. In a large number of reported works, instrumentation is often reported as a culprit for poor performance. This is because of accuracy, bandwidth, tolerance, parasitic effects, input and output impedances and cost associated with it. An overview of critical considerations in Tomography instrumentation is given in this chapter. Most of the discussion is biased towards the more popular current injection type of systems. Correct implementation of electronics instrumentation sets a platform for a successful system.

Following successful hardware implementation, the reconstruction problem has to be solved in software to generate tomograms. Some of the factors that affect the quality of reconstruction achieved in EITS are reviewed. The chapter describes the forward problem in reconstruction which can be solved using Finite Difference (FD) Methods or Finite Element Methods (FEM). The inverse problem is then reviewed, and some of the most popular algorithms used for solving it namely: the Sheffield back-projection, the

sensitivity method, Newton-Raphson and Neural Networks presented. The reconstruction problem is nonlinear and ill-posed, and is the main reason for the low quality in EITS imaging.

2.1 Electrical Impedance Tomography/Spectroscopy

Electrical Tomography is a non-invasive technique used to obtain cross-sectional images of objects by interrogating the electrical and electromagnetic properties of the internal constituents of such objects. The name "Tomography" was derived from a Greek word *tomos*, which means section. These properties are the electrical conductivity, electrical permittivity and electromagnetic permeability [31] of the constituents individually, or combined to give impedance.

Electrodes are mounted in a plane around the cross-section to be imaged. Designed current patterns are injected between some electrodes while potential differences are measured across some. Bipolar alternating currents (AC) are used in order to avoid polarization of the contents of the object under investigation. Alternatively, voltages are applied across pairs of electrodes and currents measured from others. Voltage input is particularly used for capacitance tomography, as it yields poor results for other modes [1]. When such electrodes are mounted in a single plane, a 2-dimensional image of the object in question sliced along that plane is obtained. Multiple electrode planes can also be used in order to create 3-dimensional images.

The spatial resolutions of EIT images is considerably lower than the common imaging modalities, such as X-ray and MRI, however the temporal resolution is much higher for EIT. Furthermore, EIT is less dangerous compared to these alternative methods as it does not utilize destructive and ionizing radiation energy to interrogate the imaged object. An important disadvantage of EIT, which is also responsible for its low spatial resolution is that, unlike high energy radiation such as X-rays, electrical current does not necessarily travel in straight lines through the imaged body, nor is it confined to the imaging plane, which complicates the reconstruction process significantly and turns it into an ill-posed inverse problem.

2.1.1 EITS Modalities

In resistance tomography, current is injected between a pair of electrodes. Potential differences are measured between all other adjacent electrodes. This approach produces a resistance/conductance map of the object's cross-section by discriminating among the conductivities of the different types of contents. This form of Electrical Tomography is more intrusive in many of its applications, as direct contact is needed with the imaged object. Figure 2.1, illustrates the type of measurement arrangement. Furthermore, resistance/conductance is a frequency independent property, which removes the option of spectroscopy and frequency difference imaging. This is a major disadvantage as such techniques can enhance image quality and temporal resolution.

The choice of current patterns to be used in ERT is not restricted, especially if such currents are not injected simultaneously into the imaged object. This enables the method to use short duration signals, and increase the attainable temporal resolution such as 1000 frames/s reported in [4]. Short duration signals have low excitation energy that may reduce the system accuracy. In applications where conductivity is a dominant property of the imaged medium, and high frame rates are required, this method is preferable.

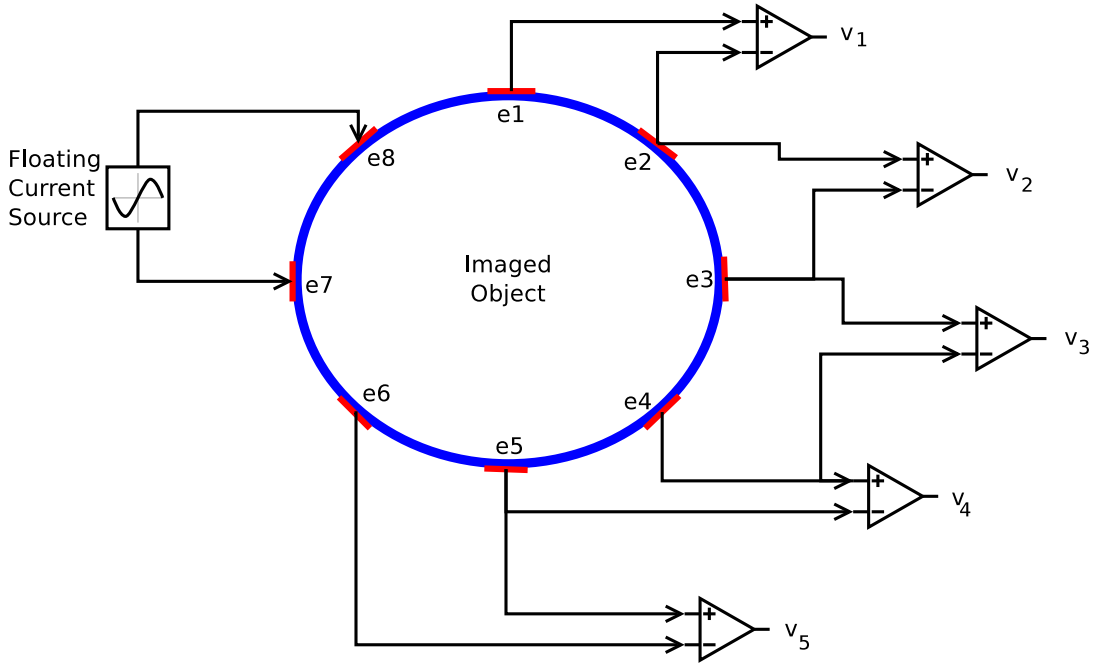

Figure 2.1: This figure illustrates a typical measurement arrangement in Resistance Tomography. It can be seen that AC current is injected between a pair of electrodes e7 and e8. Potentials are then measured across all other adjacent electrodes.

In ECT, contents of an entity can be differentiated based on their dielectric properties. This is a form of capacitive sensing that is based on the fact that the capacitance between

any two plates depends on the dielectric distribution between them. Hence, forming a number of capacitors around the object in question, a map of the dielectric profile of the object's contents can be established [32], by applying a voltage across a pair of electrodes and measuring the currents in other electrodes. An illustration is given in Figure 2.2.

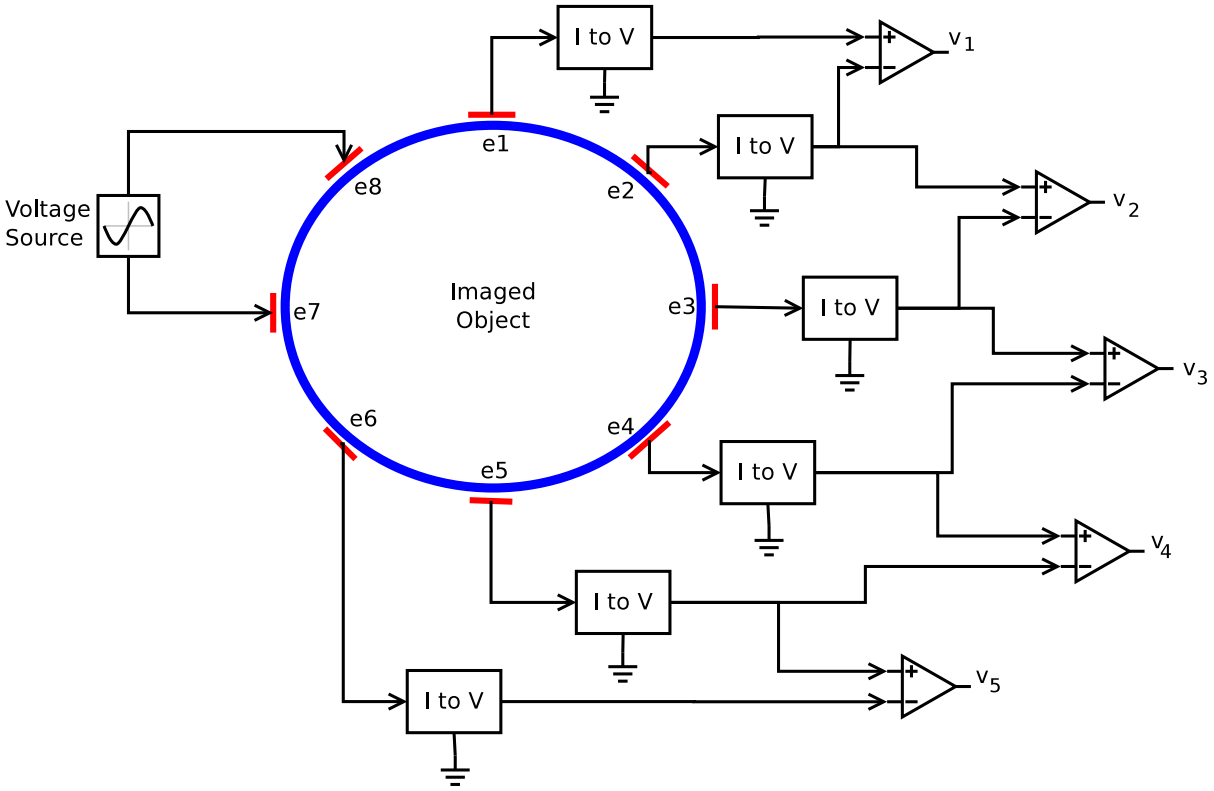

Figure 2.2: This figure illustrates a typical measurement arrangement in Capacitance Tomography. In it, a voltage is applied across electrodes e7 and e8 (transmitter node) and currents measured from all other electrodes, converted to a voltage (I to V) and transmitted for processing in differential form.

This method is less intrusive, and provides the option of spectroscopy and frequency-difference imaging as the interrogated property is frequency dependent. However, in exploiting the frequency dependence of reactance, the choice of excitation signals is limited, in order to excite a wide frequency range. Most systems use sinusoidal current patters at discrete selected frequencies for this in order to avoid complexity. *Chirp* signals, multi-sine, and pseudo-random binary sequences can be used for the excitation [33; 34]. Discrete interval random binary sequences (DIRBS) offer optimized energy over the signal bandwidth [34]. These signals, however only guarantee this an even distribution on the discrete frequencies for which they are optimized. This requires *a priori* knowledge of frequencies of interest which may not be available in EITS. Furthermore, while correlation properties of a single code are known, information on the multiplicity of equal length codes and their cross-correlation properties is not available in literature.

A more detailed discrimination of contents of an object can be obtained by interrogating both its capacitive and resistive properties. This gives rise to a dual-mode type of Electrical Tomography, Impedance Tomography. This modality carries the advantages of the other two methods while also suffering from an increased number of needed electrodes, more complex electronics and subsequent signal processing. Literature has reported the use of separate electrodes for interrogating resistivity and permeability [2] and other published works have used the same set of electrodes for both [23]. A similar configuration to that of Resistance Tomography can be used for EITS.

2.1.2 Multiplexing Methods in EITS

In order to establish which injected current is responsible for voltages observed on the measuring electrodes, it is necessary to to use multiplexing in EITS. Different multiplexing schemes are explained in this section, as they apply to EITS. Some of their applications and achievements are also discussed in this section.

The simplest way of avoiding interference between, or distinguishing among multiple transmissions through a shared transmission medium and within the same frequency band is to use time division multiplexing (TDM). Unfortunately, while this is an appealing approach which has enjoyed, and is still seeing wide deployment in the field of tomography, it mainly suffers from low frame rates, due to lengthy voltage measurement times [2; 6]. Wilkinson and colleagues [4], developed an optimized ERT system using TDM and achieved up to 1000 frames/s. Furthermore, other problems have been identified pertaining to this scheme, one of them is caused by induced impulses on the injected currents due to the switching process. TDM offers the least interference between injecting electrodes, however it lengthens measurement times if longer current patterns are used to increase excitation energy. Furthermore, it results in temporal data inconsistencies when imaging fast changing systems.

The challenges outlined for TDM, and the need for higher frame rates at relatively low complexity in dynamic imaging brought about a move in research to Frequency Division Multiplexing [2; 5]. The work reported by Teague [2] reported a temporal resolution of 280 frames/s when using FDM. This migration to FDM however, comes at a price of a higher electrode count for EITS systems. This is because injection of currents and measurement of voltages using the same set of electrodes suffers from errors introduced by contact impedances between the electrodes and imaged object [35]. Furthermore, this places stringent performance requirements on the current sources used as they are

connected in a ring [23]. Even more important, is the change in tissue impedance with frequency in biomedical applications. This therefore, prompts a careful selection of a frequency band with a more gentle change in impedance and allocating the different FDM channels within it [1; 5].

2.2 Instrumentation in EITS

The choices and design of electronic hardware are influenced by the application at hand. For biomedical applications, it is required that total injected currents be less than 1 [mA] [36]. Furthermore, all electronic devices used on the same subject should have a common ground to avoid unwanted leakage currents. Leakage currents may also arise due to parasitic circuit components and electromagnetic coupling between separate sub-circuits [1; 35]. It is desirable that live subjects be isolated from the electronic equipment. Galvanic isolation is often achieved through diode protected broadband inductors. It is important that application specific considerations be given to the design for EITS instrumentation.

The problem of identifying the impedance of an object is formed around two alternative procedures. One is to pass a known current through the object and measure the resulting potential drop in order to compute the impedance, a method used by Barber and Brown [37]. The other is to apply a voltage across the object and measure the resulting current flowing through the object [38]. Between the two approaches current injecting and voltage measurement has seen wide deployment in EITS systems due to performance deterioration if imaged object impedances are of comparable magnitudes to the output impedance of voltage sources. Furthermore, most measurement boards take voltage inputs and require a transimpedance stage, which alters the measurement, and requires calibration [39]. This is mainly due to the fact that the performance of voltage stimulation is heavily affected by the impedance of the object being imaged, due to the relatively small output impedances of voltage sources resulting in voltage divider configurations [1; 35].

Configurations of EITS systems differ according to technology choices, starting from Current vs Voltage excitation, the number of sources used at the same time and whether the sources are single-ended or floating. Pedro and colleagues used mirrored single-ended current sources and reported an improvement in output impedance [40], over the normal and modified Howland sources [41; 42]. Single-ended sources are also used in [43], with a single ground path to all. In multiple source systems instrumentation errors are cumulative and can be analyzed stochastically as done in [35]. The number

of simultaneously used measuring devices, whether or not they are single ended or differential, and whether the driving signal synthesis method is analogue or digital are also important factors.

A multiple source configuration is given in Figure 2.3 and used in the discussions that follow. It assumes current excitation and voltage measurement. If one source is used, it has to be multiplexed in time thorough all injecting electrodes of the system. Measurement of voltages is also done in a differential manner across all electrodes of the system. For the purpose of generality, digital synthesis of the driving signal is chosen as it requires more hardware stages.

Simultaneous injection of currents through multiple sources and simultaneous voltage measurement on the same or separate electrodes set, comes with substantial challenges of SNR, Common Mode signals, complexity, and accuracy. It was mentioned earlier that inaccuracies in injected currents grow cumulatively with the increasing number of sources. This therefore calls for conservative design, in which the accuracy requirements on each source are tightened in order to achieve a reasonable overall system accuracy. The most obvious approach has been to break each electrode into a part for current injection and another for voltage measurement. However, this is expensive and restricts the size of electrodes, hence the accuracy of measurement. An alternative approach has been proposed and tested in [23], using the same electrodes for the task and is a step towards reducing the complexity of EITS systems while preserving the measurement quality. The test apparatus used by the authors does not present a closed ring of current sources. The results presented are therefore, not fully representative of the emergent problems. Simultaneous injection of currents and measurement of voltages on the same set of electrodes remains a problem in EITS.

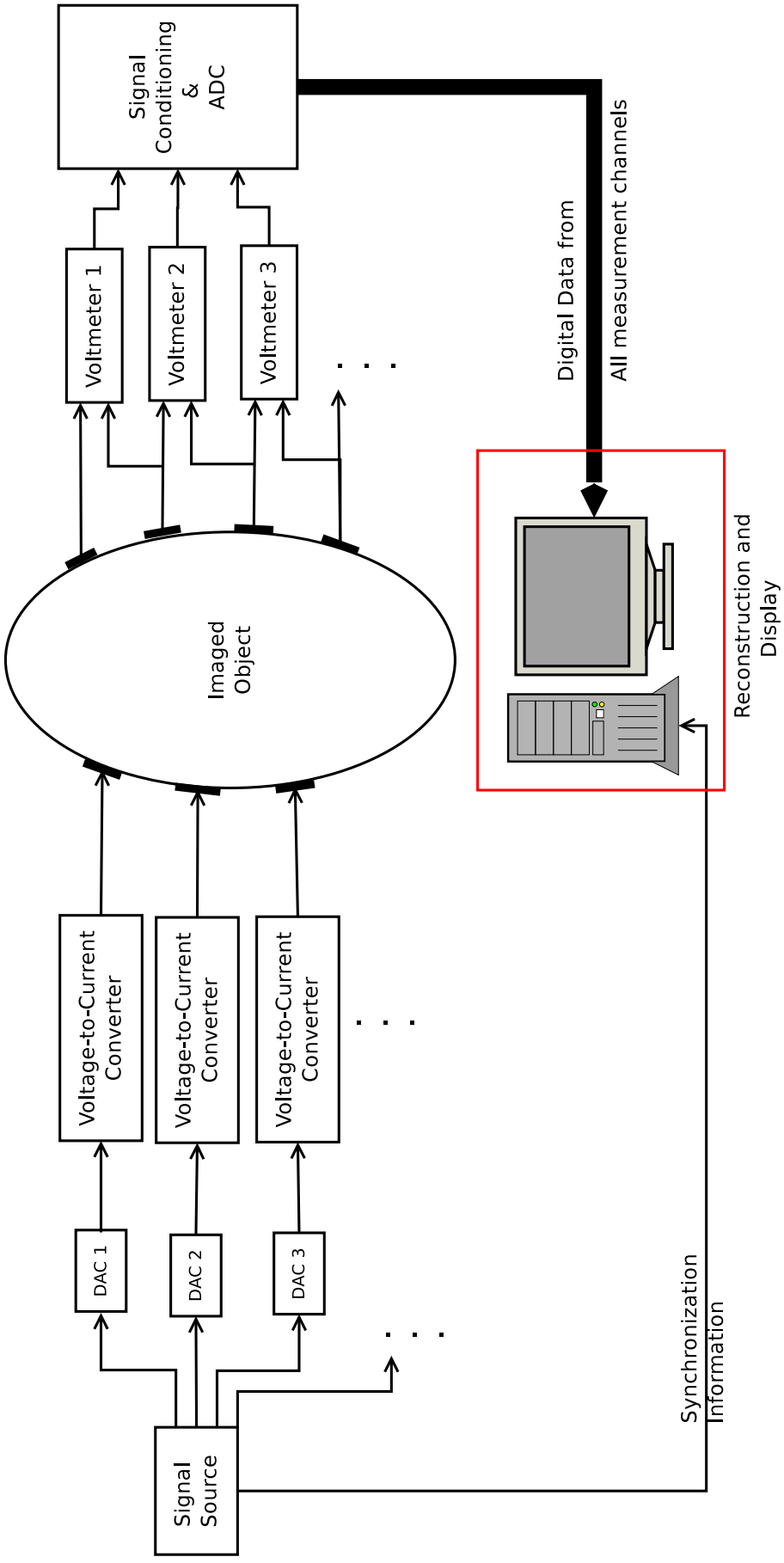

Figure 2.3: A general EITS system configuration is illustrated using digital synthesis, DAC, voltage-to-current converters, electrodes, differential voltage measurement and simultaneous injection of currents and measurement of voltages.

In EITS, a signal in the form of a voltage is generated using analog hardware or synthesized using some form of digital electronics. This signal is used to drive a current source in order to provide excitation currents injected into the imaged object. In the case of analog electronics, the hardware is straightforward in the sense that mainly oscillators are used to generate sinusoids, or some forms of pulse generators for pulse excitations. However, digital electronics is becoming a common place for producing such driving signals. Three approaches are widely adopted in digital synthesis. In the first one samples of the digital waveform are stored in FLASH devices and continuously clocked out. With appropriate logic, only half of the wavelength of the synthesized periodic waveform needs to be stored, as it contains all the information needed to re-produce the waveform. Microprocessors are commonly used for this purpose.

The second approach uses Direct Digital Synthesis (DDS) techniques in which samples are stored and a phase increment Φ is used to address the samples in a clocked manner resulting in waveforms of different frequencies depending on the size of the phase increment. It is evident that quantization of the phase increment becomes a problem, and may result in large spectral impurities. Some DDS ICs utilize phase dithering in order to deal with this problem [35]. The generated digital waveform is then passed through an Digital-to-Analog Converter (DAC), this stage introduces further signal impurities due to resolution, quantization, and signal to noise ratio. Advantages of this method are: flexibility and synchronization between the source and demodulator for digital demodulation.

As an alternative, driving functions are generated by a mathematical or logic function of time. In such a case, the signal can be generated directly in time [44]. When using pseudo-random binary sequences as proposed here, such sequences can be stored and clocked out or computed online using shift registers and feedback polynomials.

A wide range of conductive materials can be used as electrodes based on their impedances, conductivity properties, availability and toxicity to the body [1]. The most common are metal electrodes, which come in the form of silver, gold, stainless steel, copper, tin and platinum. Stainless steel is commonly used in phantom based systems due to its corrosion resistance while silver is common for biomedical applications. As an alternative to metals other materials are used such as carbon and polymers, in an effort to try and avoid injecting metal ions that may be toxic into the body.

The size, geometry and placement of these electrodes have a strong influence on the attained reconstruction quality. General guidelines dictate that current injection electrodes should be large, while voltage measurement electrodes should be small. In addition, electrodes should not be placed too closed to each other since this prevents the current

from penetrating deep into the imaged object. Corroborating research results from [10; 45] indicate that optimum performance is achieved when about $80 - 90\%$ of the imaged object's surface is covered by the electrodes. Conflicting with some of the ideas above, results reported by Wang and colleagues [24] show that there is a point where increasing electrode sizes results in poorer results. Furthermore, they argue that injecting electrode size does not have to be large, presenting FEM simulation results that show that; the spacing between compound electrodes should be large the space between the injecting and measuring electrodes should be small, and decreasing injection electrode width increases the imaging sensitivity at the center of the imaged object. A practical concern is that, the gel often used under electrodes to reduce the electrode-skin contact impedance often smears across electrodes, creating a short circuit. The investigated electrode types are given in Figure 2.4.

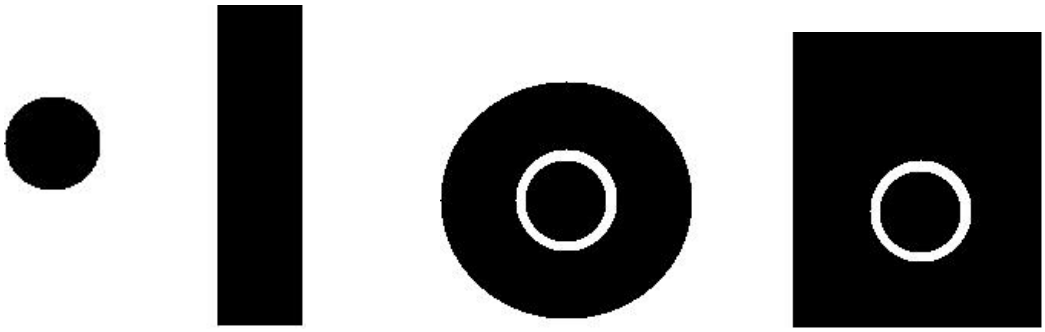

(a) Circular and rectangular line electrodes, using a single piece for injecting current and measuring voltages

(b) Circular and rectangular compound with a round center piece for measuring voltage and outer piece for injecting current

Figure 2.4: Most common electrode structures

In impedance measurements, inaccuracies often show up. These are due to inclusions of contact impedances between measuring electrodes (probes) and the specimen whose impedance is being measured. The simple form of impedance measurement setup in which this problem is eminent is the two terminal measurement, in which current is injected through and voltage measured across the same pair of electrodes. This scenario is illustrated in Figure 2.5 and the resulting measured voltage $v(t)$ depends on the contact impedances Z_{c1} and Z_{c2} as well as the load impedance Z.

$$v(t) = (Z_{c1} + Z_{c2} + Z)i(t) \tag{2.2-1}$$

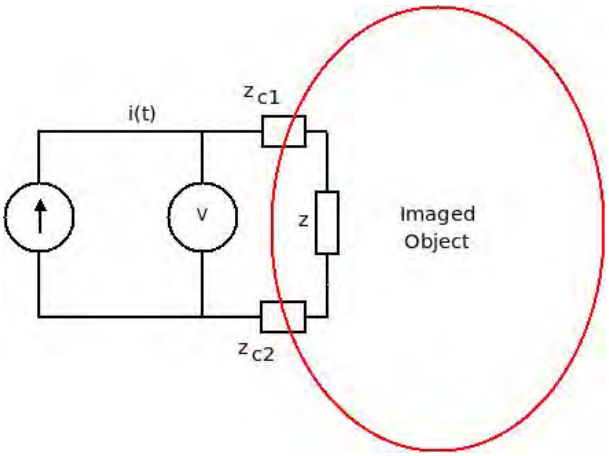

Figure 2.5: A two terminal impedance measurement, in which electrode-object contact impedances are included in the measured impedances and cause errors.

An attempt to nullify the effects of contact impedances is to have a pair of electrodes for current injection and a separate pair for voltage measurement. Due to the high input impedance of voltmeters, the current flowing through the contact impedances is negligible and renders the voltage across them negligible. This is the four terminal impedance measurement illustrated in Figure:2.6.

$$v(t) = Zi(t) \tag{2.2-2}$$

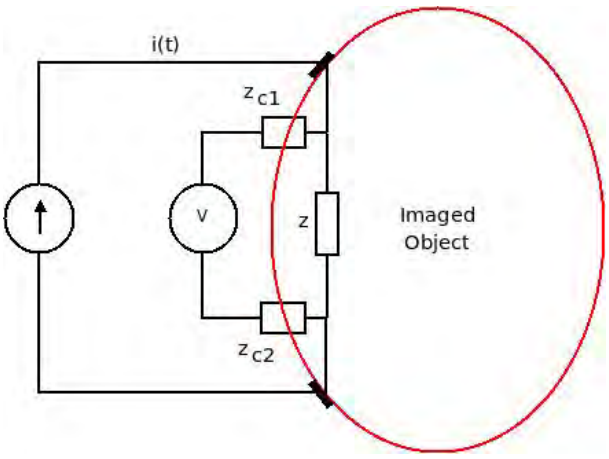

Figure 2.6: A four terminal impedance measurement, in which electrode-object contact impedances are rendered negligible by splitting current injection and voltage measurement electrodes pairs.

This configuration is used in a large number of Impedance Tomography applications,

especially ones that use multiple current sources simultaneously to inject current into an imaged object. As the number of current sources increases, this configuration results in double the number of electrodes, requiring reduced electrode sizes, which in turn reduces the image quality. An alternative method has been proposed by Tapson and colleagues [23], that allows simultaneous injection and measurement using shared electrodes, among multiple current sources and will be tested in this work.

2.3 Image Reconstruction in EITS

In single source EITS systems, one source is used to inject currents between a pair of electrodes, and resulting voltages are measured across the remaining adjacent electrode pairs. The source is time multiplexed across all electrode pairs. The voltage measurement can happen in a time multiplexed manner or simultaneously. In this scheme, two major injection protocols are dominant and these are illustrated below.

1. Adjacent Electrode Injection: In this protocol a single pair of adjacent electrodes is used to inject currents, while the remaining adjacent pairs are used to measure surface voltages. The injection and measurements are repeated using a different injection pair, and measurements until all adjacent electrode pairs are exhausted. This is illustrated in Figure 2.7, with the current injected between electrodes e15 and e16, and voltages being measured between electrodes (e1,e2), (e2,e3), ..., (e12,e13) in a 16 electrode system. Taking into account, the reciprocity of measurements, this results in $\frac{n(n-3)}{2}$ measurement for a complete measurement data set.

   Unfortunately, this measurement protocol results in more current density close to the injecting electrodes than at the interior of the imaged object, as can be seen by rotating the concentric red lines in the object to use all electrodes pairs for current injection.

2. Opposite Electrode Injection: To counter the poor current distribution of the previous protocol, an improved injection pattern involves current injected between a pair of opposite electrodes while voltages are measured between each of the remaining electrodes and a reference electrode chosen close to one of the injecting electrodes. In Figure 2.8, an illustration is made where current is injected between electrode e1 and e9 in a 16 electrode system, and voltages are measured between all remaining adjacent electrode pairs. A variant of this injection protocol places injecting electrodes at an arbitrary angle , and this is called the trigonometric injection [46].

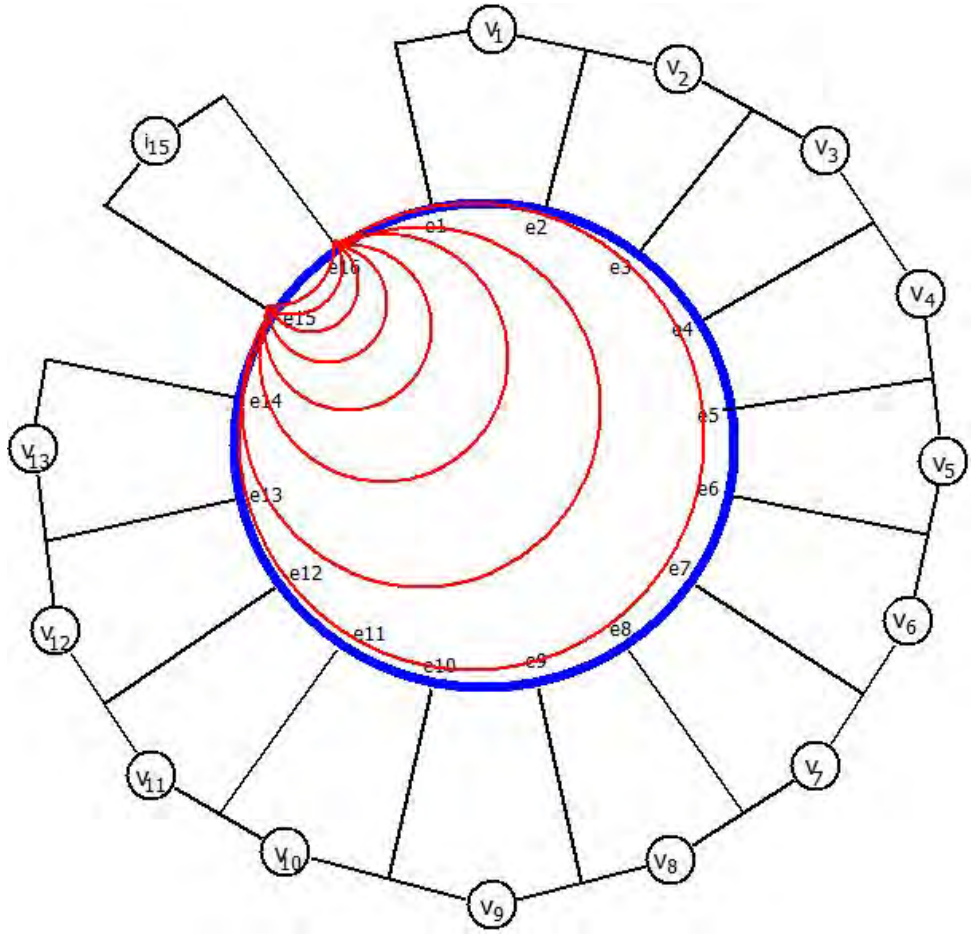

Figure 2.7: Injection of current through electrodes e15 and e16 and measuring of potentials between (e1,e2),(e2,e3), . . . , (e12, e13).

> While the current distribution is still dense close to the electrodes, this protocol results in a much more even current distribution within the imaged object (especially the center), and also results in $\frac{n(n-4)}{2}$ measurements in an n electrode system. It is reported however, that EIDORS reconstruction software does not handle this protocol well and may result in ghost mirror images during reconstruction [47].

On the other hand, some systems that have been reported use all electrodes to inject currents simultaneously and measure voltages simultaneously. These systems have the advantage of being able capture static images in which reconstruction is achieved from a data set captured at one instance. In addition, difference images taken at different time instances, or different frequencies can be reconstructed, with the advantages of being less sensitive to electrode object contact impedances. Simultaneous injection systems can result in higher frame rates enabling the imaging of objects with changing internal admittivity topologies such as oil pipelines, mineral and process applications and emptying of intestinal contents. In this approach, orthogonality is achieved by exciting the object at different frequencies or using orthogonal current patterns such as the one proposed

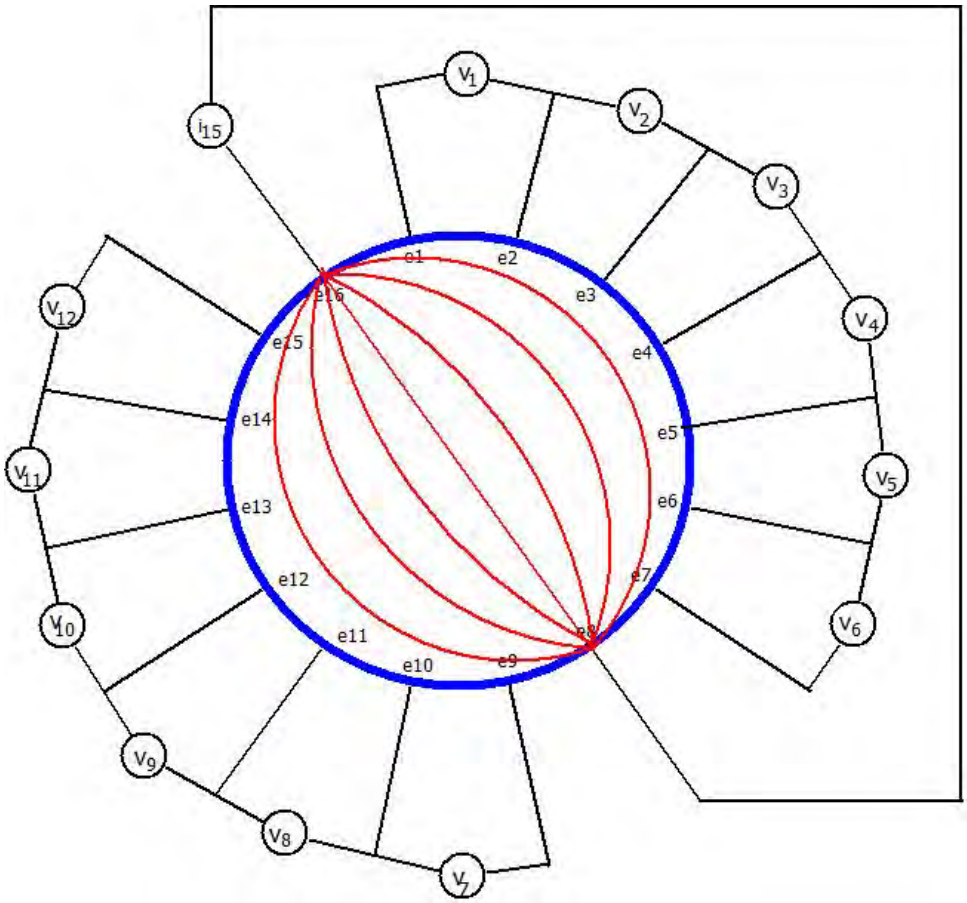

Figure 2.8: Injection of current through electrodes e16 and e8 and measuring of potentials between (e1,e2),(e2,e3), . . . , (e14, e15).

here of CDM. These are commonly referred to as Applied Current Tomography (ACT).

Variants of the above injection and measurement protocols can also exist in single ended mode. The currents can be injected in a Time Multiplexed manner on each electrode with a ground return path, or through all injecting electrodes simultaneously with single ground return electrode [43]. Furthermore, the voltages can also be measured in a multiplexed fashion or simultaneously between measurement electrodes and ground.

2.3.1 The Forward Problem

The forward problem of EITS is concerned with solving for resulting boundary potentials $\mathbf{v}_c(\mathbf{r})$ at points $\mathbf{r} = (x, y, z)$ on the surface of the imaged object with known cross-sectional conductivity distribution, when well designed current patterns are injected through it. The current patterns can be simple in TDM systems, while in FDM systems the currents injected at different electrodes (pairs) need to be at orthogonal frequencies. In CDM based

tomographs, the currents injected at different electrodes are modulated with orthogonal (or nearly so) binary random codes.

The current patterns injected on the boundary surface of the imaged object, set up current densities within the object. These current densities result in spatial potentials inside the object and on the boundary. These relationships are governed by Maxwell's laws which are summarized in the equations that follow [48; 49; 50].

$$\nabla \cdot \mathbf{E} = \frac{\rho}{\varepsilon} \tag{2.3-1a}$$

$$\nabla \times \mathbf{E} = -\frac{\partial \mathbf{B}}{\partial t} \tag{2.3-1b}$$

$$\nabla \cdot \mathbf{H} = \mathbf{0} \tag{2.3-1c}$$

$$\nabla \times \mathbf{H} = \mathbf{J} + \frac{\partial \mathbf{D}}{\partial t} \tag{2.3-1d}$$

Where $\rho[C/m^3]$ is the charge density, $\mathbf{E}[V/m]$ and $\mathbf{D} = \varepsilon\mathbf{E}[C/m^2]$ are the Electric field and Electric flux intensity respectively. $\mathbf{H}[A/m]$ and $\mathbf{B} = \mu\mathbf{H}[T]$ are the Magnetic field and Magnetic flux intensity respectively. $\varepsilon[F/m]$ is the permittivity while $\mu[H/m]$ is the permeability. $\mathbf{J} = \sigma\mathbf{E}[A/m^2]$ is the current density, and $\sigma[S/m]$ is the conductivity.

The electric field is a conservative gradient field, with its potential function being the voltage $u(\mathbf{r})$ hence: $\mathbf{E}(\mathbf{r}) = -\nabla u(\mathbf{r})$ and $\nabla \times \mathbf{E}(\mathbf{r}) \approx \mathbf{0}$ at low frequencies because of low Electromagnetic induction. By taking the Fourier Transform of the equations, it can be noted that:

$$\nabla \times \mathbf{H}(\mathbf{r}) = \mathbf{J}(\mathbf{r}) + jw\mathbf{D}(\mathbf{r}) = (\sigma(\mathbf{r}) + jw\varepsilon(\mathbf{r}))\mathbf{E}(\mathbf{r}) = \gamma(\mathbf{r})\mathbf{E}(\mathbf{r}) = -\gamma(\mathbf{r})\nabla u(\mathbf{r}) \tag{2.3-2}$$

Where $w[rad/s]$ is the frequency and $j = \sqrt{-1}$. The term $\gamma(\mathbf{r}) = \sigma(\mathbf{r}) + jw\varepsilon(\mathbf{r})$ is the complex admittivity, the inverse of whose is the complex impedance $Z(\mathbf{r}) = R(\mathbf{r}) + jwX(\mathbf{r})$. It then follows from the equation above, and the fact that the *divergence* of *curl* of a vector field is always zero $\nabla \cdot (\nabla \times \mathbf{H}) = 0$ that.

$$\nabla \cdot (\nabla \times \mathbf{H}) = -\nabla \cdot (\gamma(\mathbf{r})\nabla u(\mathbf{r})) = 0 \tag{2.3-3}$$

inside the imaged object $\mathbf{O}$. In accordance to the Fourier transformed equations the potential $u(\mathbf{r})$ is considered here as a complex phasor at a particular frequency w.

On the boundary of the imaged object, conditions can be developed for current injecting

electrodes, grounded electrode, voltage measuring electrodes as well as the free object boundary regions. Based on the findings presented in [15], the formulations of the boundary conditions are those of the complete electrode model in order to optimize the accuracy of the system. Ignoring the effects at the edges of the current injecting electrodes, the instantaneous total *normal* current at each of these electrodes can be computed as the surface integral of the current density over each electrode:

$$I_i = \int_e \mathbf{J}(\mathbf{r}, t) \cdot \mathbf{n} ds = \int_e \gamma(\mathbf{r}) \nabla u(\mathbf{r}) \cdot \mathbf{n} ds \tag{2.3-4}$$

The ground electrode is responsible for sinking the sum of all the currents injected on the other N_i current injecting electrodes, and ensuring charge conservation. Hence, the current on it is:

$$I_g = -\sum_{i=1}^{N_i} [\int_{e_i} \gamma(\mathbf{r}) \nabla u(\mathbf{r}) \cdot \mathbf{n} ds] \tag{2.3-5}$$

Equations (2.3-4) and (2.3-5), are no longer standard *Neumann* conditions. When separate injection and measurement electrodes are used, the voltage measuring electrodes ideally do not carry any current, hence:

$$I_v = \int_e \gamma(\mathbf{r}) \nabla u(\mathbf{r}) \cdot \mathbf{n} ds = 0 \tag{2.3-6}$$

Furthermore, the current density on the free sections of the object boundary is zero and therefore,

$$\gamma(\mathbf{r}) \nabla u(\mathbf{r}) \cdot \mathbf{n} = 0 \tag{2.3-7}$$

Lastly, the curl of the current density is zero at all electrodes, under the assumption of high conductivity and constant voltage in short time intervals.

$$\nabla \times \mathbf{J} \approx \mathbf{0} \tag{2.3-8}$$

If the same pairs of electrodes are used for injection and measurement, the complete electrode model incorporates the electrode contact impedance z_i, into the measured voltage equation on electrode i as follows:

$$v_i = u_i(\mathbf{r}) + z_i \gamma(\mathbf{r}) \nabla u(\mathbf{r}) \cdot \mathbf{n} \tag{2.3-9}$$

where $u_i(\mathbf{r})$ is the potential on the boundary of the imaged object in contact with the electrode. Erkki and colleagues [15] specify that conservation of charge and ground or zero potential must be specified in order to guarantee the uniqueness and existence of the

solution.

$$\sum_{i=1}^{16} I_i = 0 \tag{2.3-10}$$

$$\sum_{i=1}^{16} v_i = 0 \tag{2.3-11}$$

With the formulated boundary conditions, and constant admittivity, the forward problem in EITS is concerned with solving either Poisson's or Laplace's equation for surface potentials on an object of known internal admittance distributions, excited with known current patterns along the same surface.

The solution to this Partial Differential Equation (PDE), Boundary Value Problem (BVP), can be found by re-defining it as an *extremizing* Variational problem [51]. While some simple scenarios of this problem are mathematically tractable for analytical solution, majority of problems are significantly complex, and require a numerical solution. Among others, Finite Difference (FD) Methods, Finite Element Methods (FEM) and Boundary Element Methods have been used in this regard. Major sources of error in the FD method are the truncation errors of the first order finite divided difference approximations of differentials, inaccuracies in the formulation of irregular boundaries and numerical computer precision [52]. Apart from these the FD method solves the *strong form* (PDE) of the EIT problem, whose results are accurate. Further improvement in the solution accuracy can be attained by increasing the *refinement*, which means decreasing the size of the FD divisions or the control volume. However, this comes at the cost of heavy computation due to the increased number of equations to be solved. The Finite Element Method is used in solving the *weak form* or Integral Equation (IE) of Boundary Value Problems (BVP), arising in Science, Engineering and other fields of Applied Mathematics including EITS [53]. These problems are represented by Ordinary or Partial differential equations derived from conservation laws of Physics, examples of these are the Poisson equation and wave equation. These equations with their boundary conditions (Neumann, Dirichlet or Mixed) can be solved by transforming the problem into equivalent *weak forms* directly or through a variational *minimization* approach. In FEM a linearization of nonlinearities is performed. This places a constraint on the dynamic variables of the problem or system under investigation to small changes. Several software packages are available for solution of FEM problems, one of them is DEAL II [54]. This method is much more complex to implement compared to the FD approach. However, FEM relaxes the stringent smoothness requirements on the trial solution of the PDE and results in better accuracy due to better modeling for irregular boundaries, using isoparametric and high order elements.

2.3.2 The Inverse Problem

The Forward problem of EIT is concerned with solving a Poisson or Laplace equation to get surface potentials u_i on electrodes $i = 1, 2, 3, \ldots$, and is important for understanding the properties of, and the conditioning of the reconstruction process. It uses geometrical information of the imaged object, injected currents $\mathbf{i}$, admittivity distribution $\gamma(\mathbf{r})$, which is initialized through an informed guess process, and updated iteratively to compute the surface potentials: $\mathbf{v}_c(\mathbf{r}) = \mathbf{f}(\gamma(\mathbf{r}), \mathbf{i})$. The Inverse problem is concerned with determining the admittivity distribution $\gamma(\mathbf{r})$ within the imaged object from the knowledge of the injected current patterns on injecting electrodes and the measured voltages on the sensing surface electrodes. Numerous methods have been proposed for solving the Inverse problem including iterative methods [48; 18] and Neural Networks [2; 55; 56]. A single shot method using the sensitivity coefficients matrix was also presented by Kotre in [57]. The most illustrative and popular of the methods is the back-projection approach introduced in the next section, followed by the *Sensitivity* $\mathbb{S}$ based methods. Neural Networks have also seen application in the reconstruction problem solving to avoid the time consuming iterative algorithms. These are also introduced later in the text. Several softwares packages are available for solving inverse problems in EIT, the most popular of which is the Electrical Impedance and Diffuse Optics Reconstruction Software (EIDORS) by Lionheart and colleagues [28; 58]. Some of the developments and challenges in reconstruction methods were reviewed by William Lionheart in [14].

Backprojection

Perhaps the most intuitive reconstruction algorithm is that of Barber and colleagues [59], which is derived from the methods used in Computed Tomography (CT) [60]. In CT the radiation travels through the imaged object in a straight path. If the object is exposed to radiation at different angles, the attenuation profiles of the measured eminent radiation from the incident radiation angles can be used to localize the attenuating objects in 2- and 3-dimensions as illustrated in Figure 2.9 where only two orthogonal incidence angles are used to image an object located 4 O'clock inside a bigger object.

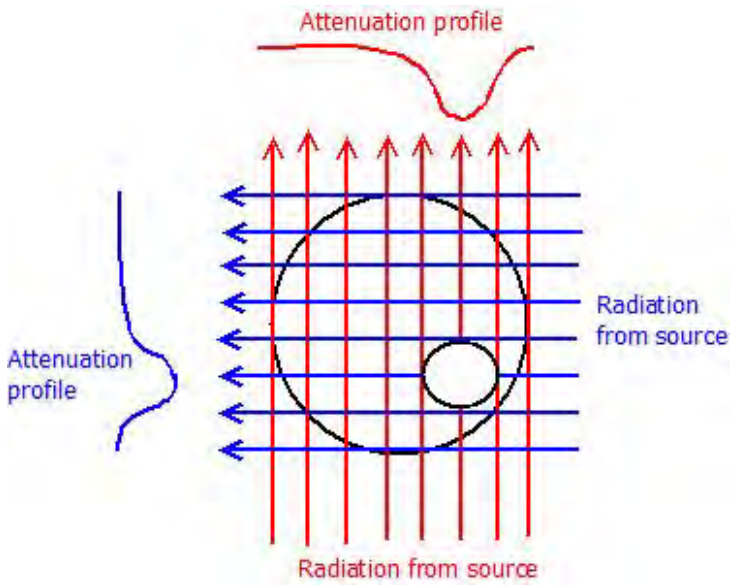

Figure 2.9: CT using vertical and horizontal radiation beams showing clear variation on the measured radiation's attenuation profile around the object's (x, y) location. The image is a free hand sketch for illustration and it is not from practical measurements

Unfortunately, in EITS currents do not travel in straight paths. However, with the assumption of small conductivity variations in the imaged object, and well defined current densities due to injected currents, *equipotential* lines can be defined in the object projecting towards the voltage measurement electrodes as shown with red and blue lines inside the circular object in Figure 2.10. In this idealized view of the problem, it is then evident from the image that only $v_1,\ v_2,\ v_3$ will be affected by the removal or placement of an object at 4 O'clock (see smaller circular object) inside the imaged medium, when current i_2 is injected. Also, only $v_2,\ v_3,\ v_4$ are affected by the same object when current i_1 is injected. The measured voltages due to a current are called a *projection* of such a current. It is then clear that as more currents are injected among electrode pairs, the mesh generated by the overlap of different projections becomes finer and finer, enabling the localization of conductivity changes within the object based on observed voltage variations from all projections.

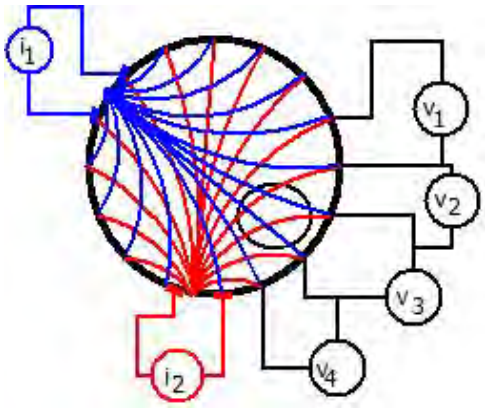

Figure 2.10: The figure illustrates the concept of backprojection as applied to EITS, showing that only v_1, v_2, v_3 are affected by the presence or absence of an object at 4 O'clock, and only v_2, v_3, v_4 are affected due to currents i_2 and i_1 respectively. The intersection of all affected projection bands marks the location and geometry of the conductivity changes

The weaknesses of the algorithm are the assumptions of evenly distributed current density and restriction to small conductivity changes. Looking at the way this algorithm works, it becomes clear how geometrical errors get introduced during reconstruction. Furthermore, it is also clear that the spatial resolution of reconstructed images is limited by the number of electrodes.

Sensitivity Methods

For lower bounded admittance values in a region **O**, the forward problem gives rise to the solution of an Elliptic PDE, with Neumann boundary conditions given by the injected currents at injecting electrodes.

In sensitivity based methods, the argument is that for a region **O** partitioned into small subsections (pixels) $P(x, y)$ in two dimensions, each with a given admittivity value $\gamma(x, y)$ and current injected at electrode (or electrode pair) e_m a voltage can be measured at sensing electrode (or electrode pair) e_n, denoted $v_{m,n,x,y}$. A small variation occurring to the value of $\gamma(x, y)$ such that the new admittance is given by:

$$\tilde{\gamma}(x, y) = \gamma(x, y) + \delta\gamma(x, y) \tag{2.3-12}$$

will produce a variation in the measured voltage [61] such that:

$$\tilde{v}_{m,n,x,y} = v_{m,n,x,y} + \delta v_{m,n,x,y} \tag{2.3-13}$$

where $\delta v_{m,n,x,y} \propto \delta\gamma(x, y)$, and if the proportionality constant is defined, it is given

by $S_{m,n,x,y} = \frac{\delta v_{m,n,x,y}}{\delta\gamma(x,y)}$. This proportionality constant is referred to as the *sensitivity* coefficient and a collection of these coefficients in matrix form corresponding to each pixel within the domain D is called the *sensitivity matrix* or Jacobian. A derivation performed by Breckon and Pidcock in [62], shows that these constants can be computed as the surface integral of the inner product of the gradients of potential fields u_m and u_n over each pixel, due to currents injected on electrode pairs n and m respectively.

$$S_{m,n,x,y} = \frac{\delta v_{m,n,x,y}}{\delta\gamma(x,y)} = \int_{P(x,y)} \nabla u_m \cdot \nabla u_n dA \tag{2.3-14}$$

where dA is a area segment of the pixel. This then means that there is a sensitivity coefficient linking every surface potential to the effects of each pixel. If instead of attaching Cartesian positions on pixels, they are just numbered from $i = 1, 2, 3, \ldots, nP$, where nP is the total number of pixels then $P(x,y) = P(i)$, $S_{m,n,x,y} = S_{m,n,i}$ and the sensitivities can be collected in a matrix equation as:

$$\mathbb{S}\delta\gamma = \delta\mathbf{v} \tag{2.3-14}$$

where

$$\mathbb{S} = \begin{bmatrix} S_{1,1,1} & S_{1,1,2} & \ldots & S_{1,1,nP} \\ S_{1,2,1} & S_{1,2,2} & \ldots & S_{1,2,nP} \\ \cdot & \cdot & \ldots & \cdot \\ \cdot & \cdot & \ldots & \cdot \\ \cdot & \cdot & \ldots & \cdot \end{bmatrix}$$

Because the number of pixels is not the same as the observed surface measurements, the sensitivity matrix is not square. This means that the solution of the equation has to use the Moore-Penrose (Generalized) inverse to obtain a least squares solution $\delta\gamma$.

$$\delta\gamma = (\mathbb{S}^T\mathbb{S})^{-1}\mathbb{S}^T\delta\mathbf{v} \tag{2.3-15}$$

This computed vector at iteration number k is used to update the initial estimate (or computed) admittances for the next iteration $k+1$.

$$\gamma_{k+1} = \gamma_k + \delta\gamma \tag{2.3-16}$$

The iterative process is therefore outlined below and is repeated until the admittance perturbations are less than an acceptable margin $\|\delta\gamma\| < \zeta$, or the set number of iterations is reached.

Step 0: Compute or estimate the initial admittivity values γ for the homogeneous medium.
Step 1: Solve the forward problem for surface voltages using current transmittance values.

Step 2: Compute the sensitivity matrix according to equation (2.3-14), and compute the transmittance change $\delta\gamma$

$$\delta\gamma = (\mathbb{S}^T\mathbb{S})^{-1}\mathbb{S}^T\delta\mathbf{v} \tag{2.3-17}$$

Step 3: Update the admittivity values

$$\gamma_{k+1} = \gamma_k + \delta\gamma \tag{2.3-18}$$

Step 4: If $\|\delta\gamma\| < \zeta$, or the set number of iterations is reached terminate, else go back to Step 1.

2.3.3 The Modified Newton-Raphson Algorithm

The Newton-Raphson algorithm has been used in most published works [4; 63], with a reported execution time less than 1 ms per image frame. In this algorithm, the geometry of the imaged object, placement of electrodes and an internal model (PDE), of the object are captured in a function $\mathbf{v}_c = \mathbf{f}(\gamma(\mathbf{r}))$, defined by a FEM or FD model. This function is in general, nonlinear and models the relationship between the image partitions or pixels, at location $\mathbf{r} = (x, y, z)$ within a 3-dimensional object, whose values are local admittivities $\gamma(\mathbf{r})$, and the computed surface voltages on the measuring electrodes. The algorithm minimizes a sum of squared errors between the computed surface voltages and the actual measured set of voltages $\mathbf{v}_m$ on the imaged object.

$$min_{\gamma(\mathbf{r})}\{J = [\mathbf{v}_c - \mathbf{v}_m]^T[\mathbf{v}_c - \mathbf{v}_m] = [\mathbf{f} - \mathbf{v}_m]^T[\mathbf{f} - \mathbf{v}_m]\} \tag{2.3-19}$$

This minimization yields the computation of local admittivity increments:

$$\Delta\gamma(\mathbf{r}) = ([\mathbf{f}']^T\mathbf{f}')^{-1}\mathbf{f}'(\mathbf{v}_m - \mathbf{f}) \tag{2.3-20}$$

where $\mathbf{f}'$ is the Jacobian matrix of $\mathbf{f}$ with respect to all the spatial admittivities $\gamma(\mathbf{r})$.

$$\gamma(\mathbf{r}) = \gamma(\mathbf{r}) + \Delta\gamma(\mathbf{r}) \tag{2.3-21}$$

The increments are used to update the current admittivity values and the computation is then repeated until the cost is less than a determined value $J \leq \zeta$ or the set number of iterations is reached. This algorithm, when used with regularization has been reported to be better than other methods, but suffers from sensitivity to measurement noise [63].

2.3.4 Computational Intelligence for Image Reconstruction

Artificial Neural Networks (ANN) are a mathematical and statistical tools used for data manipulation [64; 65]. In cases where the complex impedances of the contents of imaged objects are known to a relatively good confidence level, Neural Networks can be trained to perform the reconstruction task, of unknown distributions of such impedances within an object [55; 66; 67]. In the text that follows, an introduction will be given to the structural and functional aspects of Neural Networks.

The structure of a ANN is explained using Fig. 2.11. In it, there are Neuron nodes denoted by circular shapes, input nodes represented by squares and *connections* shown with arrow-lines, inputs and outputs are shown with solid arrow-heads. In the figure, each neuron has multiple inputs and a single output. There are two layers of neurons shown in the diagram (there can be more), of which the first is called the Hidden Neurons layer and the last is called the Output Neurons layer. Each neuron performs a mathematical function on its inputs, the simplest of which is the weighted linear summation. In order to limit the magnitude of the output of each neuron a nonlinear *activation* function is applied on the result of the mathematical function, in order to give an output. The most common activation functions are sigmoid functions given by $tanh$ and tan^{-1} functions, and these are used in Neural networks called Multi-Layer Perceptrons (MLP). This implies that for neuron No_1 the mathematical representation is:

$$y_1 = \tanh[d_1 + \sum_{i=1}^{m} w_{1i}u_i] \tag{2.3-22}$$

$$= \tanh(\sum_{i=1}^{m}[w_{1i}\tanh(\sum_{j=1}^{n} a_{ji}x_j + b_i)] + d_1)$$

where d_1 and b_i are bias scalar constants, a_{ji} are weights on all inputs x_j entering hidden node Nh_i, u_i are the hidden layer outputs and w_{1i} are scalar weights on each input to No_1. A variant of ANN use Radial Basis Functions and Wavelets as activation functions as opposed to sigmoid functions.

Figure 2.11 shows an example of a **Feed-Forward** ANN, in which there are no connections feeding back from front layers to preceding layers (principle of feedback). ANNs with feedback are called **Recurrent** ANN. Furthermore, it is possible for the network to have direct connections from the inputs (nodes) to the output neurons, and for the inclusion of a measure of time delay on the connections between nodes and neurons. It is also possible to use a linear activation function for a given layer. As an example the overall output equation of the depicted neural network, if the activation functions of the output

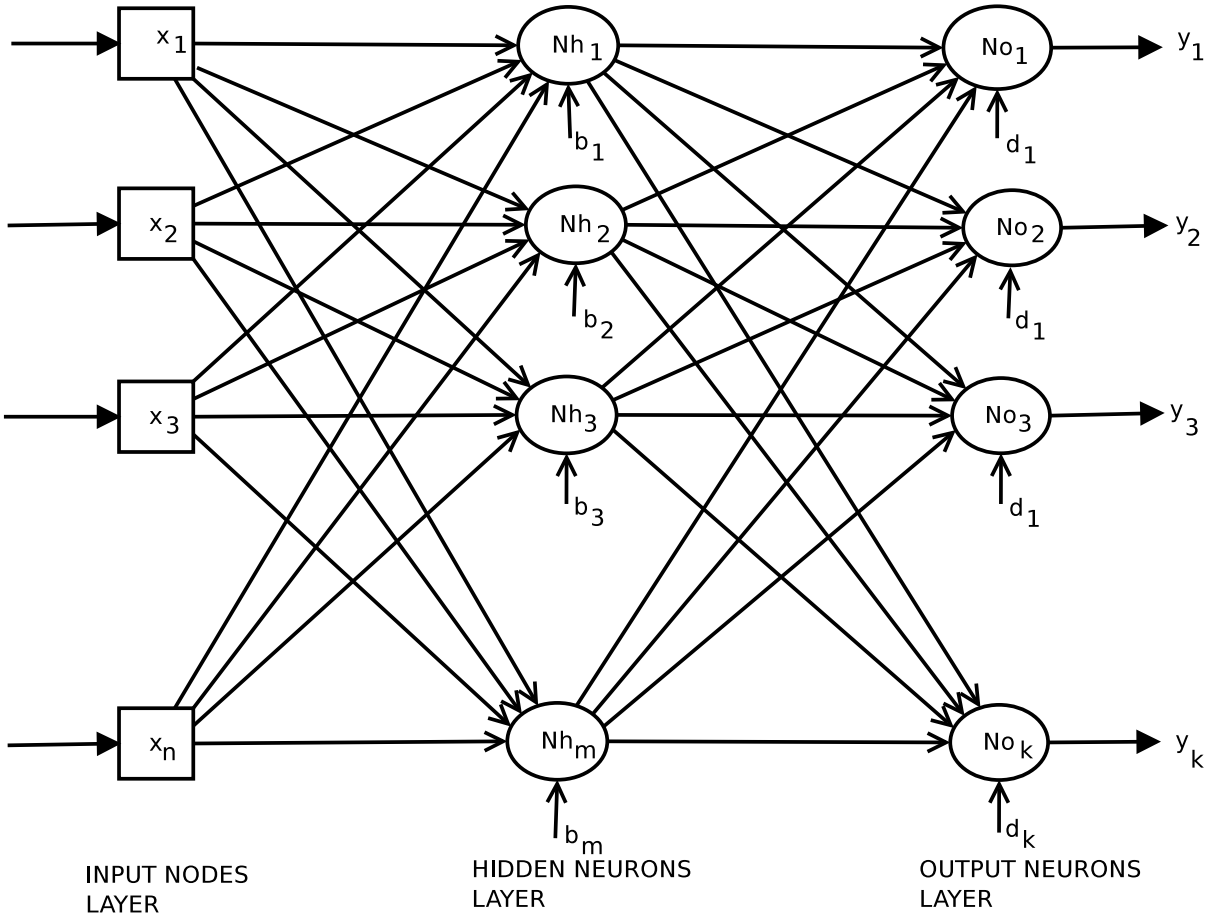

Figure 2.11: The structure of a Neural Network with n-inputs, m-Hidden neurons and k-output neurons

layer are linear would be:

$$y_1 = \sum_{i=1}^{m} [w_{1i} \tanh(\sum_{j=1}^{n} a_{ji} x_j + b_i) + d_1] \tag{2.3-23}$$

Regression is a process of estimating an unknown value of a function $y = f(\mathbf{x})$ given a vector of inputs $\mathbf{x}^T =< 1\ x_1\ x_2\ x_3\ \ldots x_n >$ and a set of known function values $\mathbf{y}$ and their corresponding input vectors $\mathbf{x}$ values. In the case of single layer feedforward network, with linear activation functions the problem is of the form:

$$\mathbf{Xw} = \mathbf{y} \tag{2.3-24}$$

and in the nonlinear activation case the problem becomes:

$$\tanh(\mathbf{Xw}) = \mathbf{y} \tag{2.3-25}$$

where the rows of $\mathbf{X}$ contain the samples $\mathbf{x}^T$ for which the function outputs are known

and stored in the column vector $\mathbf{y}$ and $\mathbf{w} =< w_0\ w_1\ w_2\ w_3\ \ldots w_n >^T$ is the transpose of a row vector containing the weighting (scaling factors) for mapping the inputs to the output and w_0 is the bias constant.

The requirement is generally that the number of known function input-output samples be sufficiently many compared to the number of inputs n to allow the regression of unknown values. But, the samples should not be too many to avoid the regression machine from simply reproducing them, a problem called *over-fitting*. This is related to the choice of the number of hidden neurons in the network.

Training is a process of using the known input-output samples to determine the values of the weights $\mathbf{w}$ in equation (2.3-24) or (2.3-25) that produce the sample input-output mapping or are close in a least-squares sense. This means that the determined weights should minimize a least-squares cost function (2.3-26). Popular training algorithms are: resilient backpropagation, scaled conjugate gradient and the Levenberg-Marquardt [64; 68]

$$J(\mathbf{w}, \mathbf{x}^T) = \frac{1}{2}\sum_{i=0}^{N}[y_i - \mathbf{x}_i^T\mathbf{w}]^2 \tag{2.3-26}$$

For the linear case, the training process is achieved by the generalized (Moore-Penrose) inversion $\mathbf{X}^{\#}$ of $\mathbf{X}$:

$$\mathbf{w} = \mathbf{X}^{\#}\mathbf{y} = (\mathbf{X}^T\mathbf{X})^{-1}\mathbf{X}^T\mathbf{y} \tag{2.3-27}$$

or in regularized form as:

$$\mathbf{w} = \mathbf{X}^{\#}\mathbf{y} = (\mathbf{X}^T\mathbf{X} + \lambda_j\mathbf{I})^{-1}\mathbf{X}^T\mathbf{y} \tag{2.3-28}$$

where λ_j are regularization constants, to alleviate matrix ill-conditioning, $j = 1, 2, 3, \ldots$ and $\mathbf{I}$ is an identity matrix of appropriate size.

For the nonlinear cases, some form of an iterative optimization algorithm has to be used to determine the weights. Some of the algorithms used can be found in [64], where back propagation is used as a way of determining the gradient of the cost function. Measures of how well a regression machine can generalize/predict the values of a function within the boundaries of its training, are: computed by using a set of input data $\mathbf{X_v}$ to validate the determined weights $\mathbf{w}$, with known function outputs $\mathbf{y_v}$ corresponding to the validation data used. One performance measure can be the Root Mean Validation Square Error (RMVSE):

$$RMVSE = \sqrt{\frac{1}{N}\sum_{j=1}^{N}[y_{v,j} - \mathbf{x}_{v,j}^T\mathbf{w}]^2} \tag{2.3-29}$$

where N is the size of the validation set or number of data samples $\mathbf{x}_{v,j}^T$ int it, $j = 1, 2, 3, \ldots, N$.

Classification is a process of assigning a *specimen* represented by a vector of values $\mathbf{x}^T =< 1\ x_1\ x_2\ x_3\ \ldots x_n >$ to one of the Classes $C_i \in \mathbf{C}$. The popular Bayes' Classifier is often used to as a theoretical benchmark for evaluating other classifiers. Alternatively a classifier is trained using a set of specimen with known class designations and tested using a different set of specimen, also with known class assignments and the number of false classifications counted to evaluate the quality of the classifier. Different to regression, the elements of the output vector $\mathbf{y}$ only take discrete values representing different classes C_i. A similar process of determining the weights $\mathbf{w}$ is followed in the training of neural networks for classification. Important analysis can be performed on the input data set $\mathbf{X}$ to show how separable it is using an index such as the Thornton's separability index [69; 70]. The dimensionality of the data set can also be reduced using techniques such as Principal Component Analysis (PCA) to lower the computation cost without compromising distinguishing features of the data set [71]. In an attempt to reduce training time incurred by gradient-based training algorithms popularly used in ANNs, Huang *et al* [72] proposed the Extreme Learning Machine (ELM) - a single layer feed-forward ANN learning method that randomly assigns input weights and biases, and uses differentiable activation functions - which has reduced tuned parameters, and results in a linear problem whose tuning is achieved by the Moore-Penrose generalized inversion.

Neural Networks can also be used for image processing functions such as filtering [73; 74]. Here interest is in their use for reconstructing an image of the cross-sectional impedance distribution of an imaged object [58; 75; 76]. In this application the inputs to the network are the Neumann-to-Dirichlet voltage data measured on the boundary of the imaged object for given current injection patterns. In this case the imaged space is partitioned into N_p pixel areas in a plane $P(x, y)$ whose values are constant at a given time and functions of their location and the measured voltages $\mathbf{v}$.

The ANN is then designed so that each of its N_p outputs correspond to each pixel in the image space. Training then becomes a process of occupying selected pixels in a training image, with known impedances (objects) and measuring the resulting surface voltages. It is essential that the impedances of the objects used in the training process be representative of the intended application impedances range. Furthermore, the number of electrodes of the tomograph and the concept of sensitivity, become of importance when deciding on the number (and sizes) of pixels to be used. In cases where the contents of the objects to be imaged are known and available or their electrical equivalents, such objects can be used for training the ANN for a classification problem. On the other hand,

if only the upper and lower impedance bounds of the contents of the imaged object are known, it would be a good idea to formulate the problem as a regression problem where the training is done using several objects of different impedances and locations, contact impedances and boundary variations, within the bounds of impedances of the imaged object contents. The number and length of experiments required for training such ANNs can be very laborious. However, this may be a better option against Finite Elements, Variational Calculus and Optimization. Mathematically this problem can be formulated, for a single pixel as shown in the equation and block diagram that follows in Figure 2.12, where $\mathbf{w}_i$ is a vector of weights linking the pixel value (admittivity value) to the vector of inputs $\mathbf{y}$ to the output node No_i from the hidden layer.

$$P(x, y) = o_i = \tanh(\mathbf{w}_i^T \mathbf{y} + d_i) \tag{2.3-30}$$

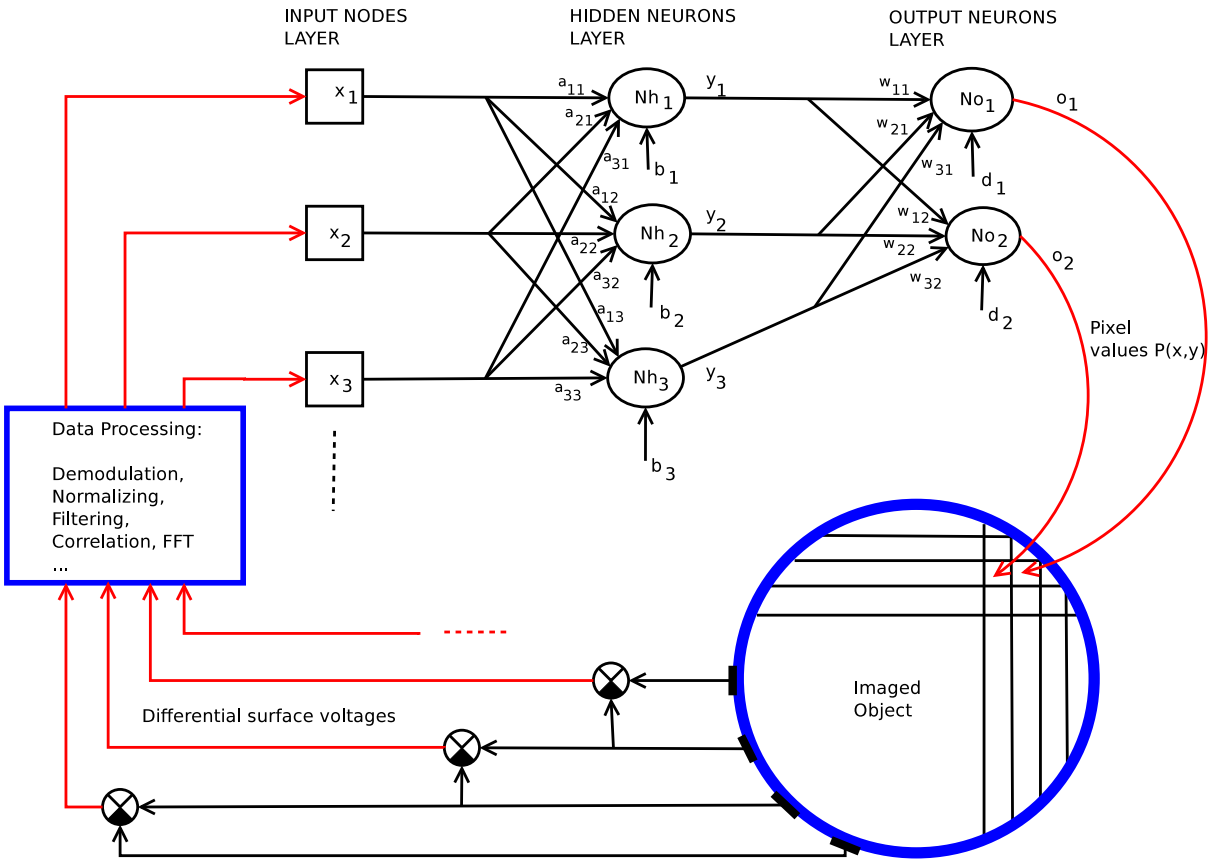

Figure 2.12: The structure of a Neural Network with n-inputs, m-Hidden neurons and k-output neurons. The inputs are processed surface voltages, and network outputs are pixel values.

The first application of Computational Intelligence in EIT reconstruction was by Miller

and colleagues, in 1992. They used a back-projection neural network to reconstruct EIT images of a 52 pixel lung model [77]. In their work, they achieved 14% error on pixel values and up to 40% classification error on unseen imaging scenarios. They recommended addition of measurement noise to bring training data close to real measurements. In 1993, Srinivasan *et al* used a Hopfield network for reconstruction of images obtained from a head model [78]. A Adaptive Linear Network was used by Adler *et al* in 1994 [79]. Their results while acceptable, showed dilations of up to a factor of 10 on reconstructed images. Applications of the Artificial Neural Network (ANN) and Bayesian networks in 1998, 1999 and 2000 showed results that are in keeping with reconstruction literature, that reconstruction quality deteriorates when smaller pixels are used due to sensitivity issues [80; 81; 82]. During the period 2001 to 2010, a multilayer perceptron was investigated by Teague [55] who reported volume fraction errors of 6.1% in a seawater-air-gravel mixture being imaged using EIT. A Radial Basis Function (RBF) network was also implemented in this period by Wang *et al* [83]. The most recent works are those of Wang and colleagues in 2015 who trained an Least-Squares Support Vector Machine (LS-SVM) using a Particle Swarm Optimizer (PSO) [84]. In their results they obtained errors of up to 41% and showed significant improvement over the Gauss-Newton algorithm. Further work by Martin *et al* also used PSO to train a ANN for reconstruction [85]. Their results showed position errors of less than 1% using the same object model and 2.91% using a distorted model. Most or the reported works have been applied on ECT, most of them did not take into account measurement noise and large pixels have been used to reduce the labor intensive data set generation and avoid poor results due to low sensitivity.

2.4 Conclusions

Electrical Tomography is a non-invasive method of imaging objects by establishing their conductivity (ERT), reactance (ECT) or admittivity (EIT) distribution along a cross-section. This is achieved by injecting currents and measuring voltages on the surface of the object in question. ERT is the simplest of the electrical tomography modes and has a potential for the highest frame rates if similar hardware specifications are used for all. However, this method does not allow frequency difference imaging and spectroscopy. ECT allows frequency difference imaging and spectroscopy. It is less intrusive compared to ERT, but may not yield optimal results where resistance is a dominant property of the imaged media. EIT combines the advantages of ERT and ECT but comes at a cost of complex electronics, processing and increased electrode count.

In order to identify which injected current pattern is responsible for causing measured

voltage changes in EIT, multiplexing is used. The most commonly used and simplest form is TDM, it allocates different time slots for each current pattern to be injected. However, due to the sequential operation approach, it results in the slowest injection and measurement times if long current patterns are used. FDM allows injection of current patterns simultaneously by modulating them onto orthogonal frequency bands. FDM does not easily allow frequency-difference imaging and spectroscopy due to its use of different frequency bands for each current. A further challenge facing TDM is that of temporal data inconsistency when applied to fast changing systems. The data consistency problem extends to FDM, in cases where frequency bands are allocated over largely varying regions of the imaged object's frequency spectrum.

Depending on the mode of electrical tomography used; ERT, ECT and EIT, and the type of multiplexing chosen for the system, different system modules are required. Furthermore, based on whether the system injects currents and measures voltages or the reverse, components needed will range from multiplexers, current sources, voltmeters, voltage sources, ammeters and electrodes. Accuracies of all these modules are of paramount importance to the operation of such tomography systems. In applications that employ frequency difference imaging and spectroscopy, the modules ought to have wide bandwidth and good gain band width (GBW) properties for optimal performance. Furthermore, the electrodes used in the system need to be of optimal geometrical shapes and arranged optimally around the imaged object. The selection of materials making such electrodes needs to consider good electro-mechanical properties: conductivity, corrosion, flexibility, soldering and others. Additionally, electrodes need to be safe for biomedical applications and not inject toxic ions into the imaged subjects. Biomedical applications further require isolation, proper grounding and properly monitored signal levels, frequencies and time durations for patient safety. Augmenting electronics such as impedance converters, buffers and filters may be needed to alleviate parasitic circuit effects and reduce noise, interference and common mode signals. A careful choice of electrical tomography mode, multiplexing, components and their design as well as safety measures are critical in the success of the envisaged tomography system.

If the errors in hardware instrumentation with its associated controlling software are minimized and the instrumentation platform meets performance specifications, the next critical stage of electrical tomography is the reconstruction of images. The problem of image reconstruction is a complex, computationally expensive and *ill-posed* in nature. Several approaches have been proposed to solve the problem and the most common of them are: the Sheffield back-projection method. This method yields relatively good results and is conceptually simple to understand, as it originates from well understood area of Computed Tomography. However, it makes assumptions that are not true for large

admittivity changes and may compromise attainable performance. The second approach is the uses sensitivity coefficients that specify the effect of a small sub-region of the imaged on each measured voltage as a result of a specific injected current. The methods based on this approach yield good performance but are also based on the assumption of small admittivity changes. The third approach is based on Neural networks and is an appealing one. However, neural networks only work within boundaries of present knowledge, based on which they are trained. It is the training aspect of these networks limit their performance both in time taken to learn and accuracy of classification or regression. Other important factors affecting reconstruction is the protocol used for injection and measuring currents and voltages respectively, and the solver used for solving the forward problem of reconstruction (FD, FEM, ...). A number of software packages are available for image reconstruction, however the most common one is EIDORS.

Chapter 3

The Proposed Approach: CDM EITS

The hypothesis of this Thesis is that, *if orthogonal (or nearly so) pseudo-random binary codes (PN) are simultaneously applied as excitation current to the electrodes of a tomograph, and resulting surface voltages are measured, the cross-correlations of the injected PN code currents and measured voltages will give impulse responses, whose fast Fourier transforms (fft) can be used to reconstruct images of complex impedance distributions of the imaged objects.* This hypothesis was formulated as an alternative multiplexing approach (CDM), that can be used in EITS to overcome the temporal and frequency data inconsistencies of TDM and FDM. Furthermore, this approach presents an opportunity for injecting high excitation signal energy, which is evenly distributed over the bandwidth of a broadband EITS system. The application of CDM in EITS, can solve problems of TDM and FDM and promises improved frame rates.

Formulations for the CDM approach investigated in this study are presented in this chapter. These are followed by formulations of the Poisson's equation and boundary conditions governing the EITS problem. The boundary conditions are formulated to conform with the EITS system configuration proposed for this work. Numerical methods for solving both the forward and inverse problem in this study are also given in this chapter, in order to provide a complete problem and solution set that can be implemented using computing software.

In order to evaluate the performance of EITS systems, a standard set of performance measures need to be defined. These performance indices include, but are not limited to the signal-to-noise (SNR) of measurement instrumentation, accuracy, repeatability,

amplitude response, detectability, distinguishablity, ringing, frame rates, position error, size error, shape deformation. These performance measures are presented at the end of this chapter, with the intention of using some of them in evaluating and quantifying the extend to which the hypothesis of this work is validated, in comparison to alternative methods and systems reported in literature.

3.1 Proposed Approach: Code Division Multiplexing (CDM)

FDM offers an improvement over TDM by avoiding temporal data inconsistencies through simultaneous current injection. However, due to the frequency sensitivity of biological tissue impedance, FDM can introduce data inconsistencies of its own. This occurs if the frequency bands assigned to current injection electrodes are selected over a frequency range that contains large changes in the impedance of imaged object contents. In addition, trade-offs have to be made between the number of electrodes and interference among simultaneously injected currents.

In Code Division Multiplexing, frequency reuse is possible since every current source (transmitter) is assigned a special pseudo random code (PN) which is used as a stimulus current pattern. All electrodes have the same bandwidth, which avoids the inconsistencies of FDM. These codes are shared between respective source and all measured voltage processors (receivers).

Taking an example of an eight electrode EIT system where four of the electrodes are used for differential voltage measurement, three used for injection 3 pseudo-random binary codes and one as a common ground electrode as shown in Figure 3.1. Each current source is given a unique PN code, which is orthogonal (or nearly so) to those of the other sources to inject into the object. The voltage processors are furnished with information on which PN belongs to which transmitter. At the receiver, the PN codes are used to separately extract the channel impulse response $h_{ij}(jw)$ between source number i and receiver number j.

The benefit of pseudo-random binary codes is that as approximations of white noise, they have a near even distribution of energy over their bandwidth. This then allows them to excite all frequencies with the same amount of energy when used in EITS. Not many other signals share this useful property. CDM extracts channel impulse responses

over the same frequency range for each source. An alternative to extracting channel impulse responses over the same frequency range is to inject a *chirp* stimulus, in a time division multiplexed manner through all injection electrodes. This however, decreases the attainable frame rates in TDM and is compounded by the length of the *chirp* in time. A further disadvantage is that of temporal data inconsistency when this approach is applied to fast changing systems. The *chirp* input approach is used in [26]. Gevers and *et al* [11], also reported recently the application of CDM in EIT using Walsh-Hadamard codes to modulate a sinusoidal carrier. Their implementation was for a narrow band EIT system, with the aim of reducing the interference between different current injecting electrodes. Their formulation does not allow frequency difference imaging and spectroscopy. Furthermore, Walsh-Hadamard codes are reviewed in this document and found inappropriate for the formulations presented in the text that follows due to the fact that their auto-correlations do not result in a single impulse function.

The advantage of using CDM is that, the cross-correlation performed with the PN codes at each output explicitly extracts the impulse responses of the channel connecting the respective output with the Transmitter that owns the PN code [27; 39; 86]. This is shown mathematically through a discrete time derivation below.

Each input signal U_i is a PN code PN_i , and the input follows different paths/channels h_{ij} to output point O_j . At each output point O_j, $j = 1, 2, 3, \ldots$ the combined output O_j is correlated with the different PN_i codes (of length T) to extract the respective impulse response h_{ij} [87]. The correlation then becomes $C_{U_i,O_j}(m)$.

$$C_{U_i,O_j}(m) = \frac{1}{T}\sum_{n=0}^{T-1} U_i[n]O_j[n-m] \tag{3.1-1}$$

Where T is the period (*epoch* length) of the PN code. At any time instance k, the combined output $O_j[k]$ at receiver j, is the sum of convolutions between the impulse responses of the different paths/channels and respective inputs.

$$O_j[k] = \sum_{p=0,r=1}^{k,r_m} U_r[k-p]h_{rj}[p] \tag{3.1-2}$$

Here, r_m is the maximum number of inputs. Substituting (3.1-2) into (3.1-1) gives:

$$C_{U_i,O_j}(m) = \frac{1}{T}\sum_{n=0}^{T-1} U_i[n]\{\sum_{p=0,r=1}^{n-m,r_m} U_r[n-m-p]h_{rj}[p]\} \tag{3.1-3}$$

Under the assumption of linearity (distributive law), this equation can be rearranged to:

$$C_{U_i,O_j}(m) = \frac{1}{T}\sum_{n=0}^{T-1}\sum_{p=0,r=1}^{n-m,r_m} U_i[n]U_r[n-m-p]h_{rj}[p] \tag{3.1-4}$$

The expression can also be re-written as:

$$\begin{aligned} C_{U_i,O_j}(m) &= \sum_{p=0,r=1}^{n-m,r_m}\{\frac{1}{T}\sum_{n=0}^{T-1} U_i[n]U_r[n-m-p]\}h_{rj}[p] \\ &= \sum_{p=0,r=1}^{n-m,r_m}\{C_{U_iU_r}(m-p)\}h_{rj}[p] \end{aligned} \tag{3.1-5}$$

The fast Fourier transform of $h_{rj}[p]$ gives the impulse response $h_{rj}[jw]$ between input i and output j. This now shows that the correlation of O_j and U_i is similar to taking the sum of the correlations of U_i with all other inputs multiplied by their respective connection channel $h_{rj}[p]$. Ideally, the PN codes' cross-correlations should be zeros and hence leaving the only term where $i = r$ which gives a unity correlation value multiplying the impulse response of the connecting channel.

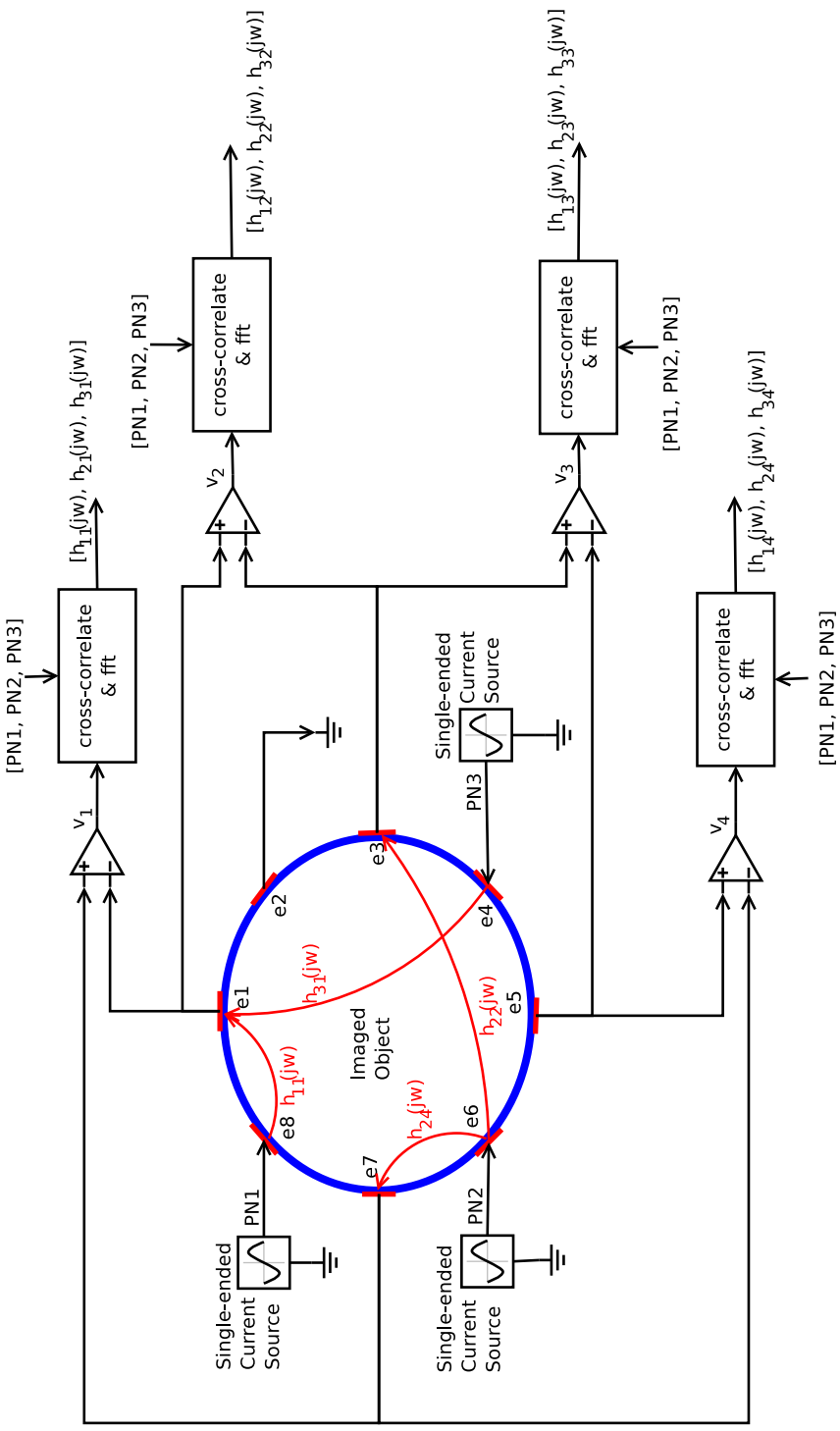

Figure 3.1: This figure illustrates a CDM tomograph. In this diagram, three single-ended current sources are assigned pseudo-random binary codes, PN1, PN2 and PN3 to stimulate the object with. The superposition of injected codes and white Gaussian noise (N) from the imaged object, modulated by the respective channel impulse responses is received at each of the four receivers as differential voltages v_1, v_2, v_3 and v_4. The PN codes are then used to extract the impulse responses through a cross-correlation process. The impulse responses after a Fourier transform, are then used for image reconstruction.

$$C_{U_i,O_j}(m) = \sum_{p=0}^{n-m} C_{U_iU_i}(m-p)h_{ij}[p] = h_{ij}[p] \tag{3.1-6}$$

This derivation can similarly be performed in the continuous time domain [88]. The output y_j at receiver j a convolution of the different inputs scaled by their respective channel weighting functions.

$$y_j(t) = \sum_{r=1}^{r_m}[\int_{-\infty}^{\infty} w_{rj}(\lambda)u_r(t-\lambda)d\lambda] \tag{3.1-7}$$

Where w_{rj} is the impulse response of the channel between input r and output j. Taking the cross-correlation of this output with an input $u_i(t)$ then gives,

$$C_{y_j,u_i}(\tau) = \lim_{T\to\infty}\frac{1}{2T}\int_{-T}^{T} u_i(t)y(t+\tau)dt \tag{3.1-8}$$

Substituting (3.1-7) into (3.1-8) gives:

$$\begin{aligned} C_{y_j,u_i}(\tau) &= \lim_{T\to\infty}\frac{1}{2T}\int_{-T}^{T} u_i(t)\{\sum_{r=1}^{r_m}[\int_{-\infty}^{\infty} w_{rj}(\lambda)u_r(t+\tau-\lambda)d\lambda]\}dt \\ &= \sum_{r=1}^{r_m}[\int_{-\infty}^{\infty} w_{rj}(\lambda)\{\lim_{T\to\infty}\frac{1}{2T}\int_{-T}^{T} u_i(t)u_r(t+\tau-\lambda)dt\}d\lambda] \\ &= \sum_{r=1}^{r_m}[\int_{-\infty}^{\infty} w_{rj}(\lambda)C_{u_i,u_r}(\tau-\lambda)d\lambda] \end{aligned} \tag{3.1-9}$$

The correlation inside the summation only assumes a finite value when $i = r$ and is zero elsewhere if the inputs are orthogonal random signals (pseudo random noise). This therefore implies that the input output correlation gives the weighting function of the respective channel.

$$C_{y_j,u_i}(\tau) = w_{ij}(\lambda) \tag{3.1-10}$$

Whose Fourier transform would now be $w_{ij}(jw)$. The zero cross-correlation and unit

impulse auto-correlations among PN codes is an idealization. In practice the auto-correlations will have nonzero floor values, and the cross-correlations will not be entirely zero.

3.2 The Forward Problem

The forward problem of EITS is concerned with solving for resulting boundary potentials $\mathbf{v}_c(\mathbf{r})$ at points $\mathbf{r} = (x, y, z)$ on the surface of the imaged object with known cross-sectional conductivity distribution, when designed current patterns are injected through it. The current patterns can be simple in TDM systems, while in FDM systems the currents injected at different electrodes (pairs) need to be at orthogonal frequencies. In CDM based tomographs, the currents injected at different electrodes are modulated with orthogonal (or nearly so) binary random codes (popularly Gold codes).

3.2.1 The Strong Form

A Poisson's PDE governing the electromagnetic phenomena within the imaged object **O** was derived in section 2.3.1 and is given here along with the associated boundary conditions:

$$\nabla \cdot (\gamma(\mathbf{r})\nabla u(\mathbf{r})) = 0 \tag{3.2-1}$$

The instantaneous total *normal* current at each injecting electrode can be computed as the surface integral of the current density over the respective electrode:

$$I_i = \int_e \mathbf{J}(\mathbf{r}, t) \cdot \mathbf{n} ds = \int_e \gamma(\mathbf{r})\nabla u(\mathbf{r}) \cdot \mathbf{n} ds \tag{3.2-2}$$

The ground electrode is responsible for sinking the sum of all the currents injected on the other N_i current carrying electrodes, hence the current on it ensures charge conservation:

$$I_g = -\sum_{i=1}^{N_i} [\int_{e_i} \gamma(\mathbf{r})\nabla u(\mathbf{r}) \cdot \mathbf{n} ds] \tag{3.2-3}$$

Equations (2.3-4) and (2.3-5), are not standard *Neumann* conditions. When separate injection and measurement electrodes are used, the voltage measuring electrodes ideally do not carry any current, hence:

$$I_v = \int_e \gamma(\mathbf{r}) \nabla u(\mathbf{r}) \cdot \mathbf{n} ds = 0 \tag{3.2-4}$$

The normal current density on the free sections of the object boundary is zero and therefore:

$$\gamma(\mathbf{r}) \nabla u(\mathbf{r}) \cdot \mathbf{n} = 0 \tag{3.2-5}$$

and lastly, the curl of the current density is zero at all electrodes, under the assumption of high conductivity and constant voltage in short time intervals.

$$\nabla \times \mathbf{J} \approx \mathbf{0} \tag{3.2-6}$$

These equations, together with the shape of the object, electrodes and their geometrical arrangement, and injection/measurement protocol are used in formulating the forward problem of EITS. In this work we use a circular object with interior $\mathbf{O}$ and boundary $\mathbf{\Gamma}$ with 32 evenly spaced electrodes, 15 of which are used for simultaneous current injection and 16 used for differential voltage measurements, while the last electrode is used as a ground path. This configuration is shown in Figure 3.2. All the parameters used are functions of position $\mathbf{r} = (x, y, z)$ and time t, however the time is not explicitly shown as the solutions are obtained at steady state.

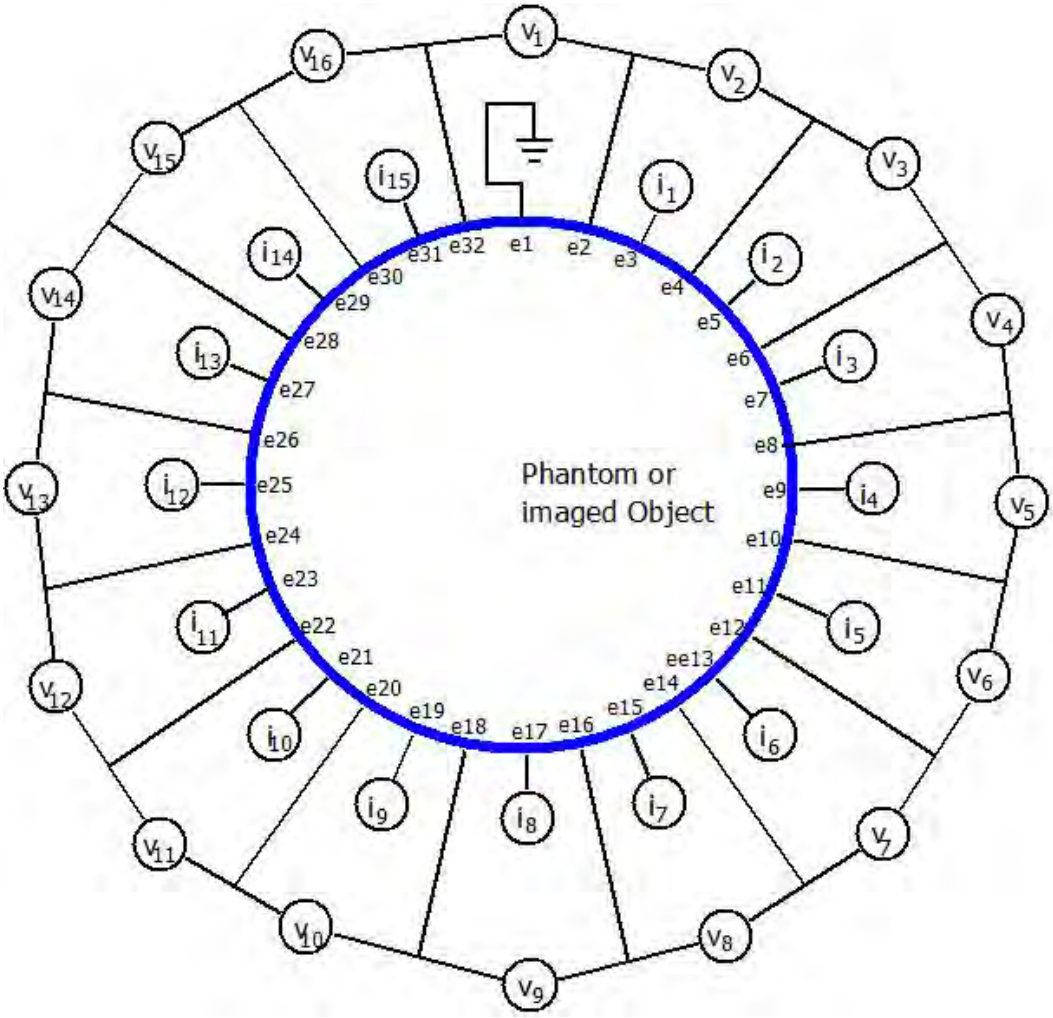

Figure 3.2: A configuration for a CDM EITS system with 15 simultaneous Gold code currents, 16 simultaneous differential voltage measurements and 1 Ground electrode.

3.2.2 The Weak Form

In order to obtain the weak form for the problem, the governing Poisson's PDE is and Neumann boundary conditions are multiplied by a weighting function $w(\mathbf{r})$ and integrated over the object domain and boundary. The weighting function is chosen to assume a value zero on all boundaries at which Dirichlet boundary conditions are specified. The selected weighting functions are required to have a C^0 continuity and be integrable [53]. At the very least, the weight functions have to be linear Lagrange interpolants in order to be complete and useful in FEM.

$$\int_{\mathbf{O}} w(\mathbf{r}) \nabla \cdot (\gamma(\mathbf{r}) \nabla u(\mathbf{r})) d\mathbf{O} \tag{3.2-7}$$

This is accompanied by a set of conditions:

$\int_{\mathbf{\Gamma}_v} w(\mathbf{r})\gamma(\mathbf{r})\nabla u(\mathbf{r})) \cdot \mathbf{n} d\mathbf{\Gamma}_v = 0$ at voltage injecting electrodes.
$\int_{\mathbf{\Gamma}_f} w(\mathbf{r})\gamma(\mathbf{r})\nabla u(\mathbf{r})) \cdot \mathbf{n} d\mathbf{\Gamma}_f = 0$ at boundaries with no electrodes.
$\int_{\mathbf{\Gamma}_i} w(\mathbf{r})\gamma(\mathbf{r})\nabla u(\mathbf{r})) \cdot \mathbf{n} d\mathbf{\Gamma}_i = \int_{\mathbf{\Gamma}_i} w(\mathbf{r}) \frac{I}{A_e} d\mathbf{\Gamma}_i$ at each current injecting electrode.
$\int_{\mathbf{\Gamma}_g} w(\mathbf{r})\gamma(\mathbf{r})\nabla u(\mathbf{r})) \cdot \mathbf{n} d\mathbf{\Gamma}_g = \int_{\mathbf{\Gamma}_g} w(\mathbf{r}) \sum^{15} \frac{I}{A_e} d\mathbf{\Gamma}_g$ at the ground electrode.

Through the use of the divergence and Green's theorems, (3.2-7) can be combined with the boundary equations:

$$\int_{\mathbf{O}} w(\mathbf{r}) \nabla \cdot (\gamma(\mathbf{r})\nabla u(\mathbf{r})) d\mathbf{O} = \int_{\mathbf{\Gamma}} w(\mathbf{r})\gamma(\mathbf{r})\nabla u(\mathbf{r}) \cdot \mathbf{n} d\mathbf{\Gamma} - \int_{\mathbf{O}} \nabla w(\mathbf{r}) \cdot \gamma(\mathbf{r})\nabla u(\mathbf{r}) d\mathbf{O} = 0 \tag{3.2-8}$$

The first integral on the right hand side of the (3.2-8) captures the boundary conditions of the problem. For this problem the boundary conditions are all Neumann type, as specified in the derivation of the strong form. These Neumann conditions are zero at all sections of the boundary that are not covered with current carrying electrodes (including voltage measuring electrodes). On the current carrying electrodes the values of the Neumann conditions are specified in terms of the injected/sunk currents. Therefore the weak form can be stated as:

$$\int_{\mathbf{O}} (\nabla w(\mathbf{r}))^T \cdot \gamma(\mathbf{r})\nabla u(\mathbf{r}) d\mathbf{O} = \int_{\mathbf{\Gamma}_i} w(\mathbf{r}) \frac{I}{A_e} d\mathbf{\Gamma}_i + \int_{\mathbf{\Gamma}_g} w(\mathbf{r}) \sum^{15} \frac{I}{A_e} d\mathbf{\Gamma}_g \tag{3.2-9}$$

3.2.3 Domain Discretization and Approximation Functions

In FEM, imaged object (domain) is segmented into smaller divisions (*elements*) of chosen shapes. The simplest shape in 2-dimensional FEM is a triangle with linear edges as depicted in Figure 3.3. For each triangle, the vertices are marked as nodes of the element. Extra nodes may be located on the edges of the element. Evident in this representation, is the fact that due to the straight edges, the triangular shapes introduce some errors in representing curved boundaries. This problem is alleviated by reducing the size of the triangles (*refinement*) at the domain edges. A better alternative is the use of elements with curved edges, called *isoparametric* elements. For this work linear triangular elements

are used and their refinement increased around curved boundaries. Other shapes can also be used as elements such as linear/isoparametric rectangles, quadrilaterals, and other higher order polytopes.

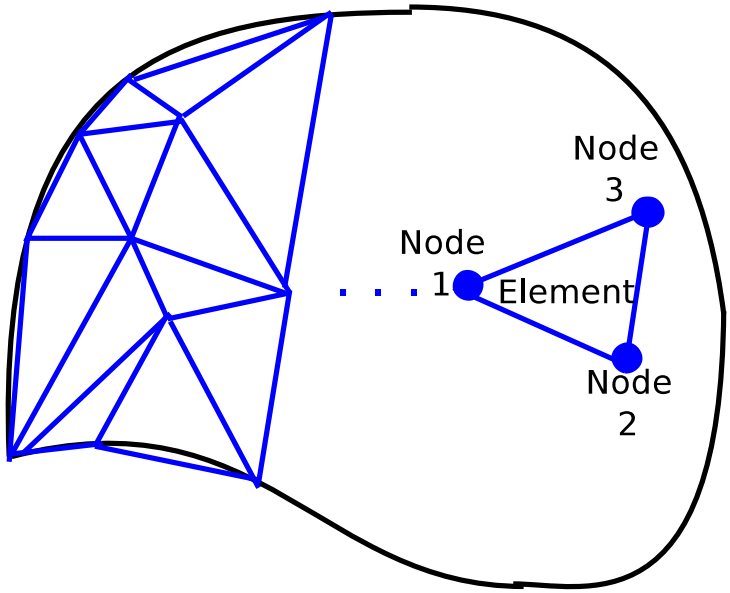

Figure 3.3: An irregular object partially segmented into linear triangular elements. Shape approximations errors are evident at the curved edges due to the linear choice of triangle edges.

In each element the function of interest, in this case the electric potential, is approximated by a trial solution function $u(\mathbf{r})$. The derivation of the weak form discussed in the preceding section made use of weighting functions $w(\mathbf{r})$. Due to the similarity in their formulations, in this section both the weighting functions and the trial solutions will be referred to simply as *approximation* functions $\theta(\mathbf{r})$. The requirements on these functions is that their minimum smoothness be C^0, because the weak form of the BVP contains first order differential/gradient operators. Furthermore, the weight functions are chosen to have a values $w(\mathbf{r}) = 0$ at all prescribed Dirichlet boundary conditions. A further requirement on the trial solutions is that they should be *compatible* at the nodes and edges of adjoining elements in order to satisfy physical requirement that the potentials be *continuous*. The requirement of compatibility comes from the fact that in electrodynamics, two points connected/collocated can not have different potentials or in mechanics, two rigidly connected points can not have different displacement values.

Approximation functions in general are required to be a complete set, which means they should be able to approximate any given smooth function with good relative accuracy. The bare minimum of complete set is that of linear functions represented by:

$$\theta^e(\mathbf{r}) = \alpha_0^e + \alpha_1^e x + \alpha_2^e y = \begin{bmatrix} 1 & x^e & y^e \end{bmatrix} \begin{bmatrix} \alpha_0^e \\ \alpha_1^e \\ \alpha_2^e \end{bmatrix} = \mathbf{p}^{eT} \alpha^e \tag{3.2-10}$$

In (3.2-10) the superscript $e = 1, 2, 3, \ldots$ gives the element number and the subscript gives the local node number within the element. The T is a simply a transpose operator. At each of the three nodes of each triangular element, the values of approximation functions are given by:

$$\begin{aligned} \mathbf{d}^e = \begin{bmatrix} \theta_1^e(\mathbf{r}) \\ \theta_2^e(\mathbf{r}) \\ \theta_3^e(\mathbf{r}) \end{bmatrix} &= \begin{bmatrix} 1 & x_1^e & y_1^e \\ 1 & x_2^e & y_2^e \\ 1 & x_3^e & y_3^e \end{bmatrix} \begin{bmatrix} \alpha_0^e \\ \alpha_1^e \\ \alpha_2^e \end{bmatrix} \\ &= \mathbf{M}^e \alpha^e \end{aligned} \tag{3.2-11}$$

Therefore,

$$\theta^e(\mathbf{r}) = \mathbf{p}^{eT} [\mathbf{M}^e]^{-1} \mathbf{d}^e = \mathbf{N}^e \mathbf{d}^e \tag{3.2-12}$$

The matrix $\mathbf{N}^e = \mathbf{p}^{eT}[\mathbf{M}]^{e-1}$ contains a set of polynomial functions (one for each global node) called shape functions. These functions assume a value of 1 at their respective node and 0 at all other nodes. This is called the Kronecker delta property of shape functions, and is essential in ensuring compatibility.

Triangular elements can have more than 3 nodes, and the extra nodes are placed on the edges. However, the formulations presented here are restricted to three node triangular elements. Figure 3.4 shows a quadrilateral object partitioned into two linear triangular elements. The nodes on the original object are called global nodes and the ones attached to each element separately are local nodes. Node numbers are assigned in a anticlockwise direction in keeping with the common convention used in available FEM softwares.

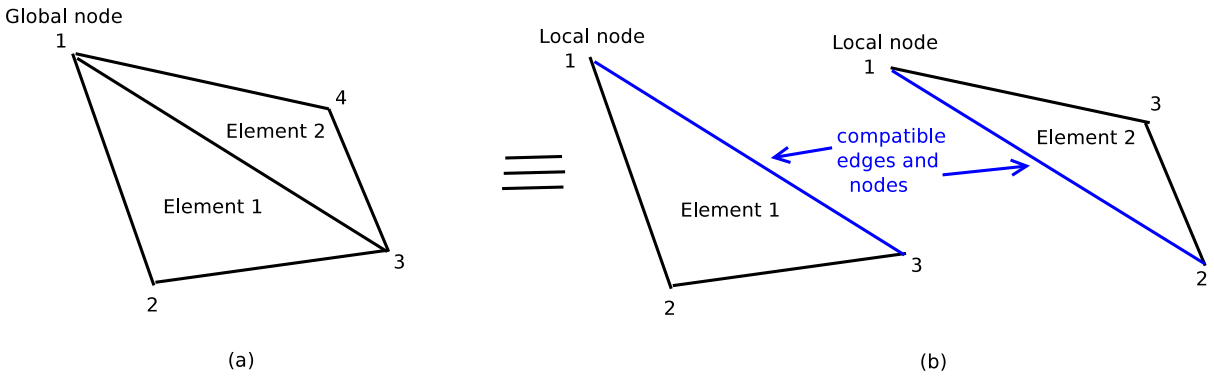

Figure 3.4: (a) A quadrilateral object segmented into two linear triangular elements, with four global nodes. (b) Separated elements showing local node numbering and the common edges on which the approximation functions must be compatible.

By examining Figure 3.4 the values of the approximation functions at the global nodes (note the absence of element numbers on global quantities) can be related to the superposition of those at the local nodes of each element as follows:

$$\mathbf{d} = \begin{bmatrix} \theta_1 \\ \theta_2 \\ \theta_3 \\ \theta_4 \end{bmatrix} = \begin{bmatrix} 1 & 0 & 0 \\ 0 & 1 & 0 \\ 0 & 0 & 1 \\ 0 & 0 & 0 \end{bmatrix} \begin{bmatrix} \theta_1^1 \\ \theta_2^1 \\ \theta_3^1 \end{bmatrix} + \begin{bmatrix} 1 & 0 & 0 \\ 0 & 0 & 0 \\ 0 & 1 & 0 \\ 0 & 0 & 1 \end{bmatrix} \begin{bmatrix} \theta_1^2 \\ \theta_2^2 \\ \theta_3^2 \end{bmatrix}$$

$$\mathbf{d} = \mathbf{L}^{1T}\mathbf{d}^1 + \mathbf{L}^{2T}\mathbf{d}^2 = \sum_{i=1}^{nel} \mathbf{L}^{eT}\mathbf{d}^e \tag{3.2-13}$$

Equation (3.2-13) represents the operation of *gathering* local element node values into global node values, the reverse operation is called *scattering*. $\mathbf{L}^{eT}$ is the transpose of a matrix $\mathbf{L}^e$ that determines the influence of nodal values of element e on global nodal values (scatter matrix), and *nel* is the total number of elements. The size of these scattering matrices depends on the total number of global nodes and their sparsity can be exploited to improve computational efficiency. Individually the contributions of each element to the global node values are:

$$\mathbf{d}^1 = \begin{bmatrix} \theta_1^1 \\ \theta_2^1 \\ \theta_3^1 \end{bmatrix} = \begin{bmatrix} 1 & 0 & 0 & 0 \\ 0 & 1 & 0 & 0 \\ 0 & 0 & 1 & 0 \end{bmatrix} \begin{bmatrix} \theta_1 \\ \theta_2 \\ \theta_3 \\ \theta_4 \end{bmatrix} = \mathbf{L}^1\mathbf{d} \tag{3.2-14a}$$

$$\mathbf{d}^2 = \begin{bmatrix} \theta_1^2 \\ \theta_2^2 \\ \theta_3^2 \end{bmatrix} = \begin{bmatrix} 1 & 0 & 0 & 0 \\ 0 & 0 & 1 & 0 \\ 0 & 0 & 0 & 1 \end{bmatrix} \begin{bmatrix} \theta_1 \\ \theta_2 \\ \theta_3 \\ \theta_4 \end{bmatrix} = \mathbf{L}^2\mathbf{d} \tag{3.2-14b}$$

Because the weak form integral of the problem contains gradients of the approximation functions $\nabla\theta(\mathbf{r})$, it is essential to perform such operations:

$$\nabla\theta^e(\mathbf{r}) = \begin{bmatrix} \frac{\partial}{\partial x}\mathbf{N}^e \\ \frac{\partial}{\partial y}\mathbf{N}^e \end{bmatrix} \mathbf{d}^e = \mathbf{B}^e\mathbf{d}^e = \mathbf{B}^e\mathbf{L}^e\mathbf{d} \tag{3.2-15}$$

Substituting the gradient equations into the weak form integral and taking the sum over all elements:

$$w^T(\mathbf{r})[\sum_{i=1}^{nel} \mathbf{L}^{eT}\{\int_{\mathbf{O}} \mathbf{B}^{eT}\gamma(\mathbf{r})\mathbf{B}^e d\mathbf{O}\mathbf{L}^e u(\mathbf{r}) - \int_{\mathbf{\Gamma}_i} \frac{I}{A_e} d\mathbf{\Gamma}_i - \int_{\mathbf{\Gamma}_g} \sum^{15} \frac{I}{A_e} d\mathbf{\Gamma}_g\}] = 0 \tag{3.2-16}$$

The matrix $\mathbf{K}^e = \int_{\mathbf{O}} \mathbf{B}^{eT}\gamma(\mathbf{r})\mathbf{B}^e d\mathbf{O}$ is called the element stiffness matrix, $\mathbf{f}^e_{\mathbf{\Gamma}_i} = \int_{\mathbf{\Gamma}_i} \frac{I}{A_e} d\mathbf{\Gamma}_i$ and $\mathbf{f}^e_{\mathbf{\Gamma}_g} = \int_{\mathbf{\Gamma}_g} \sum^{15} \frac{I}{A_e} d\mathbf{\Gamma}_g$ contain the prescribed boundary conditions at the current injecting electrodes and the ground electrode. All these integrals can be computed using Gauss Quadrature [52; 53] since the integrands are polynomials.

The global stiffness matrix and specified boundary values are:

$$\mathbf{K} = \sum_{i=1}^{nel} \mathbf{L}^{eT} \int_{\mathbf{O}} \mathbf{B}^{eT}\gamma(\mathbf{r})\mathbf{B}^e d\mathbf{O}\mathbf{L}^e = \sum_{i=1}^{nel} \mathbf{L}^{eT}\mathbf{K}^e\mathbf{L}^e \tag{3.2-17}$$

$$\mathbf{f}_{\mathbf{\Gamma}_i} = \sum_{i=1}^{nel} \mathbf{L}^{eT} \int_{\mathbf{\Gamma}_i} \frac{I}{A_e} d\mathbf{\Gamma}_i = \sum_{i=1}^{nel} \mathbf{L}^{eT}\mathbf{f}^e_{\mathbf{\Gamma}_i} \tag{3.2-18}$$

$$\mathbf{f}_{\mathbf{\Gamma}_g} = \sum_{i=1}^{nel} \mathbf{L}^{eT} \int_{\mathbf{\Gamma}_g} \sum^{15} \frac{I}{A_e} d\mathbf{\Gamma}_g = \sum_{i=1}^{nel} \mathbf{L}^{eT} \mathbf{f}^e_{\mathbf{\Gamma}_g} \tag{3.2-19}$$

Therefore the weak form (3.2-8) becomes just a matrix equation, after the numerical evaluation of the integrals:

$$w^T(\mathbf{r})\mathbf{K}u(\mathbf{r}) - w^T(\mathbf{r})\mathbf{f}_{\mathbf{\Gamma}_i} - w^T(\mathbf{r})\mathbf{f}_{\mathbf{\Gamma}_g} \tag{3.2-20}$$

3.3 The Inverse Problem

Given all the injected currents, boundary conditions and a FEM model of the imaged object. A solution of the FEM gives the scalar potential field $\mathbf{u}(\mathbf{r})$ as its solution using some approximated admittivity distribution $\gamma(\mathbf{r})$. The computed potentials at the voltage measuring electrodes of Figure 3.2 can be denoted as $\mathbf{v}_c(\mathbf{r}, t)$ and compared with the measured voltages $\mathbf{v}_m(\mathbf{r}, t)$. The time parameterization captures the fact that for time-difference imaging, two sets of measurements need to be taken at different times. All the computed and measured data are cross-correlated with the injected PN codes as discussed in section 6.1 and their Fourier transforms computed. In order to perform reconstruction the resulting frequency spectra need to be sampled in the following manner:

- Static Imaging
  In static imaging, the task is to determine the absolute admittivity distribution of the imaged object. As such a single set of measured potentials is acquired. Cross-correlation of these voltages with the injected currents is performed followed by Fourier transforms. The resulting frequency spectra are sampled at a chosen frequency w to give $\mathbf{h}_m(jw)$. FEM is used to compute surface voltages and similar operations performed on them to yield a set $\mathbf{h}_c(jw)$ the error between these two sets is then used in reconstruction to determine the increments $\Delta\gamma(\mathbf{r})$ to the approximate model admittivity distribution that will reduce this error.

- Time-Difference Imaging
  Time-difference imaging is aimed at determining the temporal changes in admittivity responsible for the change in measured potentials between times t_1 and t_2. Voltage measurements are taken at different time instances and FEM computations done to produce sets of computed potentials. Fourier cross-correlations and transforms of the two measured sets are computed, sampled at the same frequency w and the

resulting sampled sets are subtracted to represent measured temporal changes in channel impulse responses $\Delta\mathbf{h}_m(jw) = \mathbf{h}_m(jw, t_1) - \mathbf{h}_m(jw, t_2)$. A similar process performed with the computed FEM data to produce $\Delta\mathbf{h}_c(jw)$. These changes in impulse responses are used in reconstruction to compute $\Delta\gamma(\mathbf{r})$.

- Frequency-Difference Imaging
  In this case a single set of measurements is needed from the real object after injection of currents. The aim is to compute changes in admittivity within an object as a function of frequency. At each reconstruction iteration, a single set of potentials is computed from the FEM model. Cross-correlations are performed on these two sets and their Fourier transforms computed. As opposed to time-difference, here both resulting frequency spectra are sampled at two different frequencies w_1 and w_2. The quantities $\Delta\mathbf{h}_m(jw) = \mathbf{h}(jw_1, t) - \mathbf{h}(jw_2, t)$ and $\Delta\mathbf{h}_c(jw)$ are computed accordingly to be used in the reconstruction.

Figure 3.5 shows a block diagram illustration of the reconstruction task for problem formulated here.

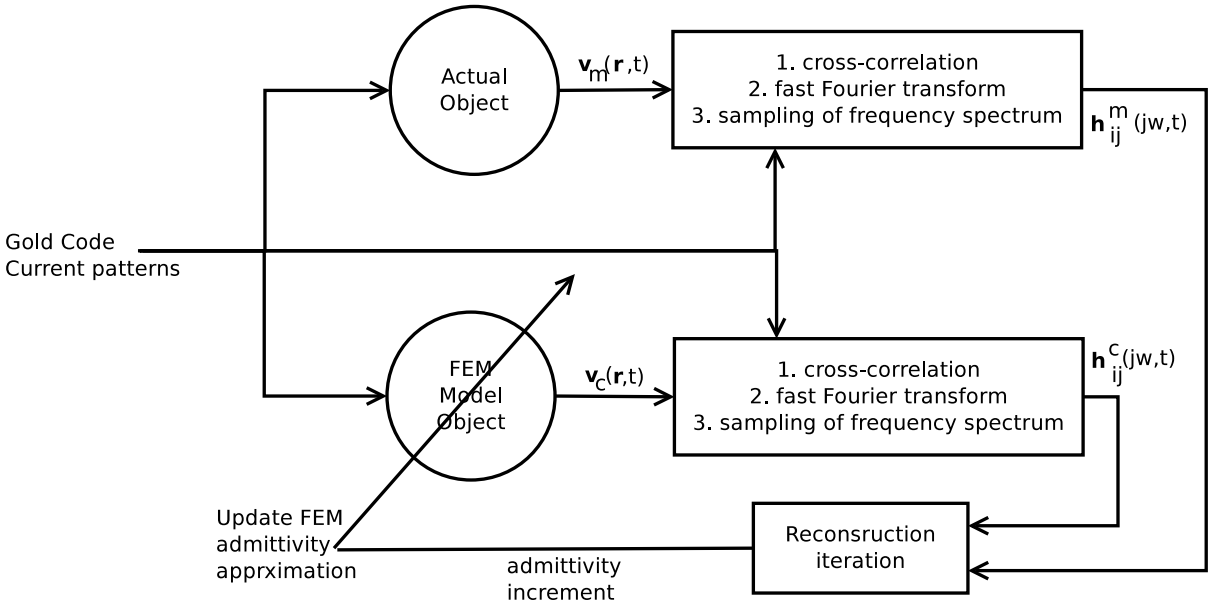

Figure 3.5: A reconstruction block diagram showing the error between the measured and computed voltages being used to update the FEM admittivity until it converges to the actual admittivity distribution.

3.3.1 The Modified Newton-Raphson (m-NR): EIDORS

Due to its reported good performance [63; 89], the modified Newton-Raphson algorithm also referred to as the Gauss-Newton algorithm in EIDORS is used for this problem. The challenge of this algorithm is its sensitivity to measurement SNR leading to ringing in the reconstructed images. Most early reported works only minimize the error between the measured and computed potentials, and introduce regularization to alleviate the ill-conditioning of the reconstruction problem. In this section we present the regularized NR method and include a term for inclusion of prior information,hence the objective function to be minimized is:

$$\Phi(\gamma) = \frac{1}{2}\{\lambda_i[h_{m,i} - f_i(\gamma(\mathbf{r}))]^2 + \eta_j[\Delta\gamma(\mathbf{r})]^2\} \tag{3.3-1}$$

In equation 3.3-1 λ_i is a regularization constant responsible for alleviating ill-conditioning. This constant penalizes the error between measured and computed surface potentials on electrode pair $i = 1, 2, 3, \ldots$. The function $f(\gamma(\mathbf{r}))$ is a representation of the FEM which encapsulates the mapping between the admittivities and computed impulse responses at the measuring electrodes, taking into account the object geometry, electrode positions, boundary conditions and internal sources if any. η_j is a constant that restricts the computed change in admittivity in element j based on prior knowledge of the relative distribution of the admittivities. Equation (6.2-16) can be written as a matrix quadratic form:

$$\Phi(\gamma) = \frac{1}{2}\{\|\mathbf{h}_m - \mathbf{f}(\gamma(\mathbf{r}))\|^2_{\mathbf{Q}} + \|\Delta\gamma(\mathbf{r})\|^2_{\mathbf{R}}\} \tag{3.3-2}$$

Here $\mathbf{Q} = \begin{bmatrix} \lambda_1 & 0 & 0 & \ldots \\ 0 & \lambda_2 & 0 & \ldots \\ 0 & 0 & \lambda_3 & \ldots \\ 0 & 0 & \ldots & \lambda_{16} \end{bmatrix}$ and $\mathbf{R} = \begin{bmatrix} \eta_1 & 0 & 0 & \ldots \\ 0 & \eta_2 & 0 & \ldots \\ 0 & 0 & \eta_3 & \ldots \\ 0 & 0 & \ldots & \eta_{nel} \end{bmatrix}$.

The minimization of this cost function is the solution of the iterative problem in (6.3-18) until the cost value is below a given value.

$$\Delta\gamma(\mathbf{r}) = ([\mathbf{f}'(\gamma(\mathbf{r}))]^T\mathbf{Q}\mathbf{f}'(\gamma(\mathbf{r})) + \mathbf{R})^{-1}[\mathbf{f}'(\gamma(\mathbf{r}))]^T\mathbf{Q}(\mathbf{f}(\gamma(\mathbf{r})) - \mathbf{h}_m) \tag{3.3-3}$$

and,

$$\gamma(\mathbf{r}) = \gamma(\mathbf{r}) + \Delta\gamma(\mathbf{r}) \tag{3.3-4}$$

Here $\mathbf{f}'(\gamma(\mathbf{r}))$ is the Jacobian of functional mapping $\mathbf{f}(\gamma(\mathbf{r}))$.

3.3.2 Alternative Methods

Alternative methods to the m-NR were presented in Chapter 4, however due to their reported inferior performance to the m-NR they are not used in this work. It is worth noting however that the Computational Intelligence methods have not been explored extensively in EITS and significant strides have been made in this field of study. A revisit of some of these methods can potentially yield good performance in reconstruction.

3.4 Results Presentation and Analysis

Results from this research work were predominantly in the form of reconstructed images and their actual photographed counterparts for comparison purposes. Graphs were used to display used signals for validation, and visual inspection. Furthermore, graphs were also used to display static, dynamic and statistical properties of the instrumentation and measurement system. Bode plots were used to show the computed frequency spectra after cross-correlation and Fourier transformation. The designed hardware was tested for accuracy, repeatability, measurement noise and interference immunity. The software results were visually inspected, checking of the properties of the generated codes against literature and the statistical balance of the produced codes.

A number of authors have made an effort to formulate standard methods and indices that can be used to gauge the performance of EITS systems [22; 90; 91]. However, most of these works were published around 2010. As a result, the research contributions reported before that time, primarily rely on three modes of evaluating EIT system performance: signal to noise ratio (SNR), error in determining known conductivities of objects and visual inspection of resulting images. This makes comparison of results obtained using different tomography systems difficult, due to non-standard performance indices used in reporting (if any at all). In the mentioned published works, several measures of system

performance are proposed and used and some are discussed in the subsections that follow:

3.4.1 Hardware Performance

1. Accuracy: Systematic Error Ratio (SER)
   Quantifying the accuracy of a measurement device involves applying the device to measure an object with known/standard properties. McEwan and colleagues [7] benchmarked the performance of their results against directly measured impedance spectrum of a banana over the frequency range: 1 kHz - 1 MHz. Against these direct measurements the results obtained by Woo [10] can be compared, showing an error of about 0.04 S/m at 10 kHz, an error of 80%. Granot [5] and colleagues compared the RMS impedance error in their injection/measurement protocol with the trigonometric protocol showing a maximum variation 20 Ω and a general trend indicating that their protocol performs better than the trigonometric protocol.

2. Reciprocity: Reciprocity Error Ratio (RER)
   For systems employing the same set of electrodes for injecting and measuring currents and voltages respectively, regardless of whether this is done in a simultaneous or sequential manner, the sensitivity of a measured voltage $v_{ij}^{ab}(t)$ between electrodes e_a and e_b due to a current pattern injected between electrodes e_i and e_j and the one in the reverse injection and measurement is constant. This introduces reciprocity between each pair of measurement and injection electrodes if their roles are reversed. However for the configuration used here and by [5] this principle does not apply since electrodes are not shared between injection and measurement. In order to test this property, a reciprocity test can be performed between each pair of measuring and injecting electrodes while the admittivity distribution is kept constant. Disturbance variables such as temperature should be carefully controlled/monitored. Tong *et al* reported reciprocity errors of 0.05% in the KHU Mark 1 system [92].

3. Amplitude Response (AR)
   This index measures variation in measured pixel amplitudes when an inhomogeneity is placed at different locations in the phantom. A test can be performed by moving the object by constant offsets from one side of the phantom to the other, along a straight path. It can shed information on the symmetry of the measurement system about a line perpendicular to the line of motion of the inhomogeneity object. Yasin [91] and colleagues used this index on to compare and contrast three systems using adjacent injection and measurement protocol. This test can also be used to establish the detectability of objects placed at different locations within the phantom. By moving their inhomogeneous object around the phantom in the vicinity of each

electrode and at the center, it was shown in [5] that, while the system can detect the object, the achieved resolution differs with the location of the object. This was mainly due to the uneven current distribution of the injection and measurement protocol. A $z - score$ computation of this index can be performed using the value of a pixel p_v, the mean pixel value at different locations $\bar{p}_v$ and its standard deviation $std[p_v]$ as:

$$AR = \frac{p_v - \bar{p}_v}{std[p_v]} \tag{3.4-1}$$

4. Repeatability
   With every measurement instrument it is desired that measurements of a similar scenario at different time instances give the same outcome. This property can be tested by performing the same measurement at regular time intervals, enough times to enable the computation of the mean value of the measurement and associated standard deviation and variance. Box-Whisker plots or probability distribution plots can be used to represent this measure of performance.

5. SNR or Noise Error Ratio (NER)
   The NER is a ratio of the root-mean-square value of the noise to the value of the measured variable. It is the inverse of the signal-to-noise ratio (SNR). It is usually measured against the smallest expected amplitude of the measured signal or the device's signal resolution, as a SNR or above 50% on the resolution can introduce intolerable measurement errors. Majority of reported systems give a specification of the attained SNR over the system's bandwidth. Yasin and colleagues reported the use of this index in [91]. A review of some tomography systems and their SNR values is given in [93]. Another use of noise measure using its mean ($mean[v]$) and standard deviation ($std[v]$) was reported by Fabrizi [94] and colleagues comparing the KHU Mark 1 and UCL Mark 2.5 systems.

$$SNR = \frac{mean[v]}{std[v]} \tag{3.4-2}$$

6. Low frequency drift
   This is a measure of how a measurement of a constant input or constant periodic signal shifts in its zero frequency (DC) value over the duration of the measurement. It is usually determined by factors such as temperature, ionization of chemical mixtures and electronic device properties.

7. Injection and Measurement Protocol
   Injection protocols have a direct effect on the system complexity in terms of electrode count, processing hardware and speed of acquisition of measurements. More importantly,

measurement protocols have a direct influence on the distribution of injected currents in the imaged object and the imaging sensitivity. A review of some tomography systems and their injection/measurement protocol (parallel or serial) is given in [93].

8. Measurement Frame Rate
   The frame rate is the number of complete measurements needed for reconstruction which can be collected in a period of time (frames/s) using the complete assembled hardware and data acquisition software. It does not include the delays introduced by reconstruction. It is limited by the hardware and software capabilities, the injected current patterns and protocols used to inject currents and measure voltages. A review of some tomography systems and their frame rate values is given in [93].

3.4.2 Reconstruction Performance

1. Detectability (D) and Sensitivity
   This is a measure of the smallest change in admittivity and size of inhomogeneity object that can be detected by a given tomography system. Theoretical guidelines dictate that a 16 electrode system can detect a minimum of an inhomogeneity occupying 5% of the imaged object, and this number is 10% for an 8 electrode system. The test for AR outlined in the previous subsection can be used to establish this property in addition to theoretical analysis that may be performed. This attribute is seldom quoted as a numerical value. However, in some reported works it can be deduced from presented results, for instance from the results presented by [7] it can be deduced that at 128 kHz the system cannot detect a conductance change of 0.025 S/m of an inhomogeneity object occupying 10% of the phantom, which gives a sensitivity of 25% of the full range of the measured conductivity (0.05 S/m - 0.15 S/m). Woo [10] reported a system that could detect 0.01 S/m conductivity changes at 10 kHz for an object occupying 33% of the phantom size. In [22] the detectability is measured using the $z - statistic$ computed on the reconstructed image and actual one.

   In the author's opinion, detectability should be a measure of how well an object at a given location is detected and reconstructed. As such, this performance index (D) should be a weighted aggregate of all N other indices $p_i \quad \forall\, i = 1, 2, 3, \ldots, N$, in a similar manner to the Global error of Fabrizi and colleagues [94]. If all the contributing indices are computed as percentages such that 0% means "perfect" and excluding all indices computed as $z - scores$, then detectability for a single object should be computed as:

$$D = \frac{\sum_1^N p_i}{N} \tag{3.4-3}$$

2. Position error (PE)
   Besides the proposal of and the use of PE reported in [22; 91] no other use of this measure was found by the author. This is a measure of reconstruction accuracy that captures the the difference in the radial distances of the actual and reconstructed inhomogeneity objects" centers d_a and d_r respectively. Such radial distances can be computed relative to the phantom's center, edge or based on their (x, y) position.

$$PE = d_r - d_a \tag{3.4-4}$$

   This value is more useful when computed as a fraction of the phantom diameter d for comparative purposes. This is because the significance of absolute errors depends on the size of the phantom.

$$PE[\%] = \frac{d_r - d_a}{d} \times 100\% \tag{3.4-5}$$

3. Size Error (SE)
   In a similar manner to the PE, the size error is seldom quantified in reported reconstructions. This can be used to measure the difference in the size of the reconstructed image and the actual object. In most cases the reconstructed object appears larger than the original object. Through visual inspection of results reported by Granot in [5], an object occupying 31% of the phantom placed at its center was reconstructed obtaining a dilated reconstruction of 41% occupancy using FDM. This reconstructed occupancy worsened to 51% for the same object located in the vicinity of the current sinking ground electrode, giving a size error of 20%. The deterioration could be attributed to the high current density close to the single ground electrode compared to elsewhere in the phantom. In [7] a banana object occupying 10% of the phantom was used and a reconstructed image showing 20% occupancy was reconstructed at $2kHz$, at an error of 10%. Nahvi [26] reported results that show a size error of approximately 11%. For circular objects, this can be computed using the reconstructed object diameter d_r, the actual imaged object diameter d_a and phantom diameter d:

$$SE[\%] = \frac{d_r - d_a}{d} \times 100\% \tag{3.4-6}$$

4. Shape Deformation (SD)
   Shape deformation measures the difference in shape between the actual object and

the reconstructed image due to artifacts introduced by the reconstruction process and measurement noise. Graphs showing average relative error are reported in [26]. In most reported works, a visual assessment is used to establish the position error, size error and shape deformation without any statement of numerical measures. In [22] the shape deformation is defined with reference to a circular approximation of the reconstructed object. This definition is inadequate since it does not account for arbitrarily shaped objects and the fact that reconstruction algorithms tend to produce circular or oval reconstructions even for non-oval/circular objects. However, it can be defined as a measure of the reconstructed object that lies outside the boundary of the actual imaged object A_+ as an absolute value or percentage of the original object size A_o.

$$SD[\%] = \frac{A_+}{A_o} \times 100\% \tag{3.4-7}$$

5. Distinguishability
   This is a measure of how well a designed tomography system can distinguish among several inhomogeneity objects within the imaged object. The question associated with it is how the radial distances between the objects affect their distinguishability and their relative sizes. A test of distinguishability is done using more than one objects' of differing sizes placed at selected radial distances from each other. The quality of the distinguishing ability of the system can be quantified through position error, resolution and shape deformation after reconstruction. Among a few results reported on multiple inhomogeneity objects, the work of Navi and Hoyle [26] shows that the system can distinguish a banana and cucumber object in a single phantom, however, the reconstructed images incorrectly represent the objects as having equal sizes and shapes which is inaccurate. A report of the UCL Mark 1b distinguishing among three circular objects (banana, cucumber and perspex) using time difference and frequency difference imaging is given in [95]. The indices discussed earlier such as PE, SE, SD and the $z - statistic$ can be used to quantify the distinguishing ability of a system.

6. Ringing
   Ringing is a measure of how much negative admittivity changes are evident in the reconstructed images. This artifact usually appears as areas of pixels containing negative polarity impedance changes in the image. No publications using either TDM, FDM or random codes were found that quote a measure of ringing. Some works use thresholding to remove ringing in order to give clearer images.

Out of all the discussed measures of performance, some of them are not applicable to

the system designed here. Furthermore, some of them are not widely used and do not provide a good platform for comparison with other reported systems. However, a selection of indices was made that provide a measures of how accurate the designed prototype system is. Additionally, they were chosen to provide a means of comparison between the current prototype and the reported systems using FDM, TDM [4; 5] and the works of McEwan and colleagues who applied pseudo-random codes as current patterns using a time difference multiplexing scheme [7].

3.5 Conclusion

A mathematical formulation of the EITS problem using CDM was presented in this chapter. The formulations show that under ideal conditions, it is possible to extract channel impulse responses between current injecting and voltage measuring electrodes. These impulse responses can be extracted from the measured data on each voltage electrode by cross-correlating it with each of the injected Gold codes (PN) followed by a Fourier transform operation to obtain the frequency response of each channel. Through the solution of the forward problem using FEM computations and using the error between the FEM computed surface voltages and measured ones, the Newton-Raphson algorithm can be used to adjust the approximated admittivity distribution of the finite element model until it converges to that of the actual object. Regularization is used to alleviate the ill-posedness of the inverse problem by choosing constants λ_i associated with each electrode. These are chosen taking into account the measurement accuracy on the respective electrode. When available, prior information about the imaged object can also be used to penalize the incremental changes made by the Newton-Raphson algorithm to each element of the finite element model in each iteration.

Performance measures and indices were discussed that were used in quantifying the performance of the designed prototype system and resulting reconstructed images. These indices are used to evaluate systematic errors, noise errors and reconstruction errors of the system. The most applicable of these are: size error, position error, repeatability, noise-error-ratio, detectability, amplitude response, accuracy and shape deformation. While these performance measures have not enjoyed wide deployment in reported EITS works they provide an easy and standard platform for comparison of different systems and methods.

Chapter 4

Simulations and Proof of Concept

In this chapter, simulations of the proposed approach in the previous chapter are presented. These are intended at providing a proof of concept for the proposed approach since the works of Tapson and colleagues [23] used a time division multiplexed system to produce results, and the works of Gevers and colleagues [11] used a sine wave carrier modulated by random codes in a narrow-band system and both do not provide sufficient proof of concept. Simulations demonstrating the properties of PN codes are also presented in this chapter. As a benchmark for comparison with EITS reconstruction results, PN codes are used to identify a single-input single-output (SISO) system, to demonstrate the spectral contamination that comes with the use of PN codes. Results of the simulated CDM EITS system are compared with reported works in literature using the measures presented in Chapter 3. Furthermore, the outcomes of this simulation chapter are used to inform the design process for the EITS prototype system in the chapter that follows. These simulation results are validated by experimental results presented in Chapter 6.

4.1 Random Codes and Statistical Properties

Owing largely to works done in CDMA Communication systems and Acoustic Engineering, many types of pseudo-random binary codes have been reported. These are called "pseudo" because they appear random at first, but repeat after a given period, determined by the size of the Linear Feedback Shift Registers (LFSR) used or how the codes are formed. However, comparative literature on the statistical properties of these codes against each others is not in abundance as far as the author is concerned. This section deals with the generation of some of these codes and finishes with discussions of some of their properties

and suitability for use in multiple-source CDM tomography systems.

There is a large number of methods reported in literature for measuring randomness of the sequences produced by pseudo-random binary sequence generators [96]. These are grouped into statistical and empirical tests, the *Serial correlation* test has been chosen out of both groups for the purpose of this work. In this investigation both the auto- and cross-correlation properties are vital for good performance. The cross-correlations have been studied in [97].

4.1.1 Maximum Length Codes (ML)

ML codes are the easiest to generate, requiring a feedback shift register. These codes have good auto-correlation properties that get better with increasing code length, however their cross-correlation properties are not impressive. Furthermore, there is only a limited number of primitive polynomials for each code order such as 60 for a 10 bit one. Figure 4.1 illustrate the auto-correlation and cross-correlation behavior of a typical ML code using feedback masks $\begin{bmatrix}10 & 3 & 0\end{bmatrix}$ and $\begin{bmatrix}10 & 8 & 3 & 2 & 0\end{bmatrix}$ for 10 *bit* wide codes. This would give codes of length 1024 *chips*. Shorter codes can also be used at 8 *bits* wide, 256 *chips* long with masks $\begin{bmatrix}8 & 7 & 2 & 1 & 0\end{bmatrix}$ and $\begin{bmatrix}8 & 7 & 6 & 5 & 4 & 2 & 0\end{bmatrix}$, or 9 *bits* wide, 512 *chips* using masks $\begin{bmatrix}9 & 4 & 0\end{bmatrix}$ and $\begin{bmatrix}9 & 6 & 5 & 3 & 0\end{bmatrix}$. The minimum code width chosen for this work (16 electrodes) must produce a minimum of sixteen codes and is 8 *bits* wide.

4.1.2 Gold Codes

In order to circumvent the problem of poor cross-correlation properties of ML codes, with a maximum cross-correlation 383 over all codes of length 1023 (10 bits). Gold proposed a formulation of a set of codes that offer better cross-correlation properties [97; 98]. These are generated by a polynomial:

$$x = yz \tag{4.1-1}$$

where y and z are primitive polynomials for the n^{th} Galois Field ($GF(2^n)$), without any common factors, called *preferred polynomials*. The polynomial x generates $2^n + 1$ unique sequences, with a maximum correlation of $\theta_c = (2^{\frac{(n+1)}{2}} + 1)$ or $\theta_c = (2^{\frac{(n+2)}{2}} + 1)$ for odd and even n respectively. These sequences have a period $T = 2^n - 1$. For 10 bit sequences a pair of preferred polynomials is given by the masks:

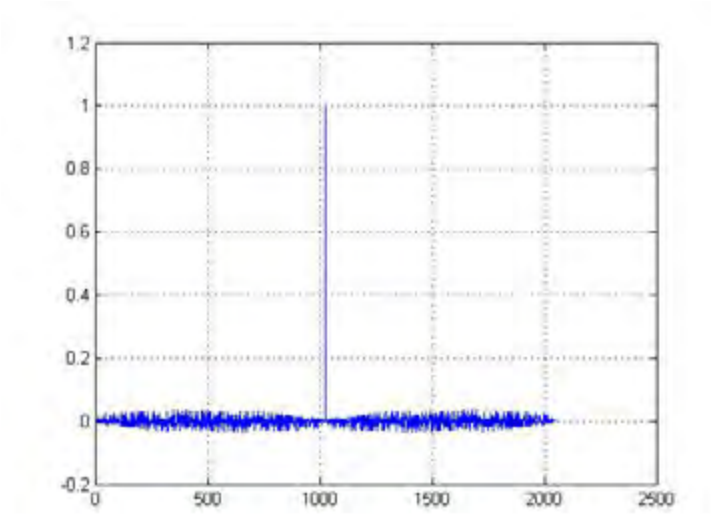

(a) Auto-correlation of ML codes with masks

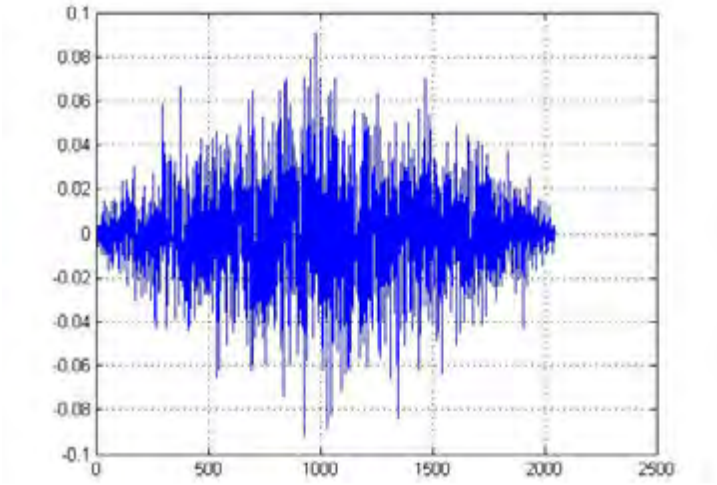

(b) Cross-correlation of typical ML codes.

Figure 4.1: Normalized serial correlation properties of typical 10 bit ML codes.

$y = \begin{bmatrix} 10 & 3 & 0 \end{bmatrix}$ and $z = \begin{bmatrix} 10 & 8 & 3 & 2 & 0 \end{bmatrix}$.

Sequences resulting from this preferred pair are generated and typical auto-correlation and cross-correlations of randomly selected pairs are shown in the Figure 4.2.

The combination process described above is equivalent to taking the Exclusive OR of the ML codes generated by the initial primitive polynomials y and z at all their possible phase shifts, hence the production of $2^n + 1$ distinct codes. For the purpose of this work the codes should be generated from an XOR of out of phase base ML codes. This is because generation from a product polynomial x is in a serial fashion that will lengthen the excitation rate or require storage for simultaneous application. Gold codes have good

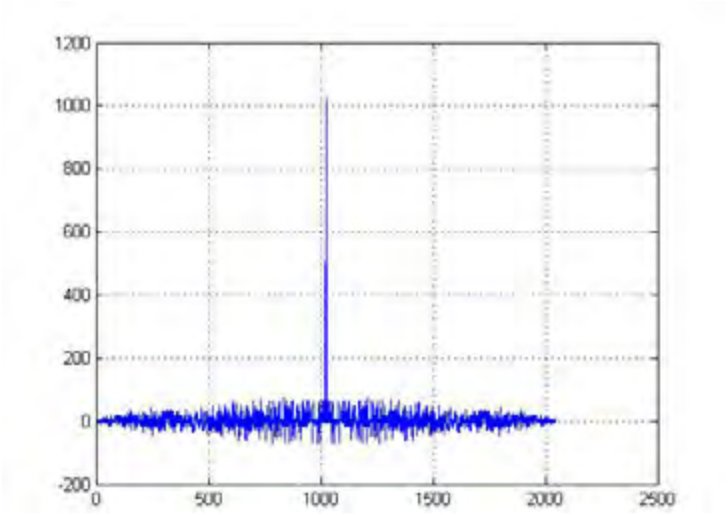

(a) Auto-correlation of typical gold codes

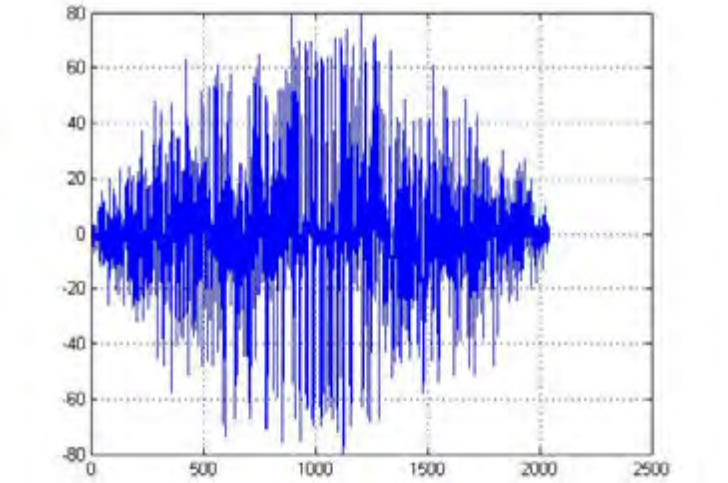

(b) Cross-correlation of typical gold codes.

Figure 4.2: Serial correlation properties of typical 10 bit Gold codes.

correlation properties with impulse auto-correlations. These properties improve with code length.

4.1.3 Kasami Codes

Kasami sequences are a set of pseudo random sequences generated by a polynomial $h = pq$ of degree $\frac{3n}{2}$. Here p is a primitive polynomial that generates a ML sequence S_1 of degree n, where n is even and q is a polynomial of degree $n/2$ that generates a subsequence S_2 of S_1. The roots of q are powers of the roots of p [99; 100]. The small set of Kasami codes have comparable properties to those of Gold codes but are fewer in number at any given

code length. The large set of Kasami codes have poorer correlation properties compared to Gold codes, but have more codes at each code length. The generation of these codes is not as simple as that of Gold codes.

4.1.4 Walsh-Hadamard Codes

Walsh codes are generated in a recursive manner by an equation:

$$\mathbf{W}_n = \begin{bmatrix} \mathbf{W}_{\frac{n}{2}} & \mathbf{W}_{\frac{n}{2}} \\ \mathbf{W}_{\frac{n}{2}} & \bar{\mathbf{W}}_{\frac{n}{2}} \end{bmatrix} \tag{4.1-2}$$

where $\bar{\mathbf{W}}$ is the bitwise logic complement of $\mathbf{W}$. Here $\mathbf{W_1} = 0$. From (4.1-2) an $(n \times n)$ binary matrix can be defined whose rows (save the first all-zero row) form the required sequences of length n.

A variant of the above codes are Orthogonal Variable Spreading Factor codes generated using a binary tree (1,-1) as demonstrated in Figure 4.3. Each branching level of the tree forms a $(i \times i)$ matrix, where every w_{ij} forms the j^{th} row of the matrix, $i = 1, 2, 4, 8, \ldots$ and $j = 1, 2, 3, \ldots$

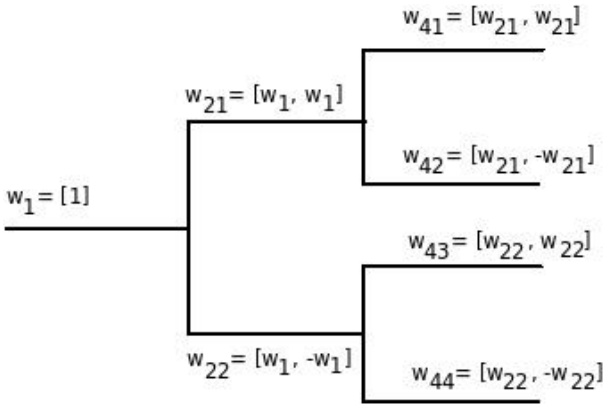

Figure 4.3: Recursive tree for construction Orthogonal Variable Spreading Factor codes.

In a similar manner that the Walsh codes are generated using the matrix formulation, Hadamard codes are generated using the following recursive matrix formulation:

$$\mathbf{H}_n = \begin{bmatrix} \mathbf{H}_{\frac{n}{2}} & \mathbf{H}_{\frac{n}{2}} \\ \mathbf{H}_{\frac{n}{2}} & \bar{\mathbf{H}}_{\frac{n}{2}} \end{bmatrix} \tag{4.1-3}$$

where $\mathbf{H_1} = 1$.

Walsh-Hadamard codes have perfect (zero) cross-correlations when their phase shift is

zero. If the phase shift of codes is non-zero, the cross-correlation properties deteriorate but are still better than those of Gold codes at any code length. These codes are easy to generate however, their main disadvantage is that their auto-correlations contain more than one impulses which makes them difficult to decode, and requiring external synchronization for the task.

4.1.5 Barker Codes

These codes have good correlation properties, but only go to a maximum length of 13 bits. This in return defeats the purpose of injecting high signal energy for the Tomography application. These codes are given in Table 4.1.

Table 4.1: Table of Barker Codes

Length n [bits]	Code
1	[-1]
2	[-1 1]
3	[-1 -1 1]
4	[-1 -1 1 -1]
5	[-1 -1 -1 1 -1]
7	[-1 -1 -1 1 1 -1 1]
11	[-1 -1 -1 1 1 1 -1 1 1 -1 1]
13	[-1 -1 -1 -1 -1 1 1 -1 -1 1 -1 1 -1]

4.2 Identification Using Random Codes

Among the different pseudo-random binary codes discussed in the previous section, Gold codes are the only type that offer good correlation properties, give a large number of distinct codes of the same length, have a single impulse auto-correlation and do not require stringent external synchronization. This makes them a good choice for application in simultaneous injection CDM based EITS. As a result, the remainder of this work will use Gold codes as the the codes of choice.

The initial proposal of the hypothesis of the work contained in this thesis was published and patented by Tapson, van Schaik and Holder in [23]. In their work they performed preliminary experiments using two pseudo random codes stored in a micro-controller and a circuit representation of a subsection of a typical imaged object. The main aim of this chapter is to support their proof of concept by simulation and experimentation, and

increased number of used electrodes. To the best of the author's knowledge there has not been a system employing the proposed CDM technique using more than 2 electrodes reported.

The principle of system identification using random signals is established and presented in a myriad of texts on signal processing. The presentation in this subsection is purely for the purpose of developing and intuitive feel of the concept. The magnitude bode plot in Figure 4.4 is obtained through injecting a Gold code current of 1024 *chips* into a parallel RC (R = 100, C=2.7 μF) low pass circuit and measuring the voltage across it. The output voltage is sampled at 3072 $Samples/s$. The output and input are then cross-correlated and an impulse response computed.

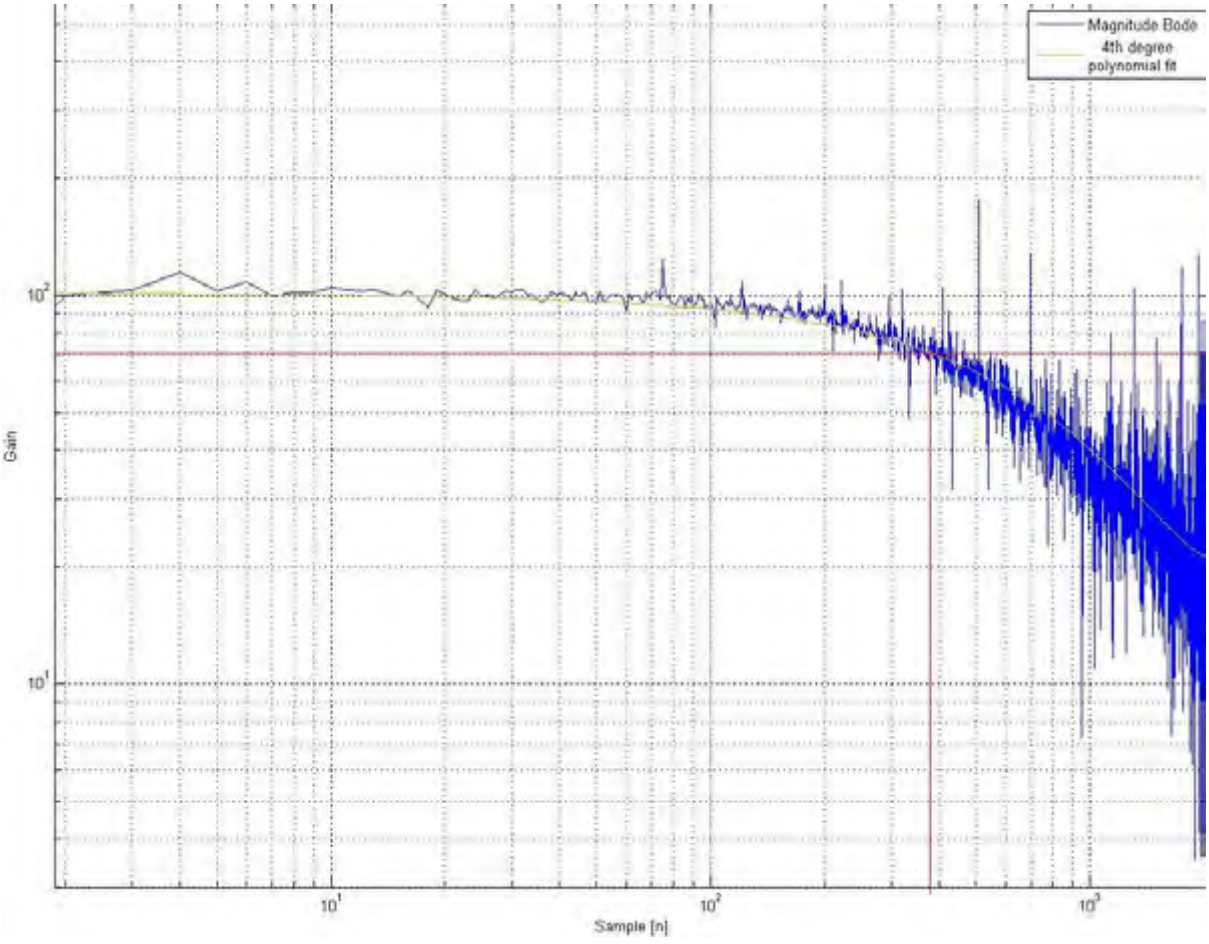

Figure 4.4: Bode plot of a RC low pass filter using a 1024 *chips* Gold code current input.

Through this experiment, it was established that the quality of the identified impulse response was not as good as theory suggested, and needs to be divided by the Fourier transform of the auto-correlation of the Gold code used. The results in Figure 4.4 are from such a process. In addition to that, a 4^{th} order polynomial fit is used to approximate the underlying magnitude Bode plot for accuracy. The reasons for this identification method

performing below expectation are that: (a) ideally the auto-correlation of a pseudo-random binary code produces an impulse function. However, due to the non idealities of these codes that is not the case as the floor values of the auto-correlation are non-zero and (b) the peak is not an impulse but a triangular pulse due to the codes being sampled at more than one sample per chip.

Other than the accuracy issues and spectral contamination seen on the magnitude Bode plot. It is established that the identification of the RC circuit gain and time constant is successful using the Gold code input. This is shown on the plot by the approximated gain value of 100 and bandwidth 370 Hz. The gain identification is almost 100% accurate while the bandwidth has an error of +19 Hz.

4.2.1 EIDORS Simulation

In this simulation experiment, EIDORS is used to create a circular tank with 15 single ended injection electrodes, 16 differential measurement electrodes and one ground electrode. Gold codes are set as stimuli and an impedance FEM mesh with a circular object at 3 O'clock, 6 O'clock, 9 O'clock and 12 O'clock are used. Reconstruction is run to establish the effectiveness of the CDM method and the effects of the non-ideal correlations between injected Gold codes. The reconstruction shows that the objects can be identified however, the spatial resolution is not good. Figures 4.5, 4.6, 4.7, 4.8 show the results. The problem of contaminated frequency spectrum that led to the division by the auto-correlations of the codes in the previous simulation is compounded here, and a similar method is used together with polynomial fitting. Figure 4.9, shows the contaminated bode plot with a polynomial fit on it.

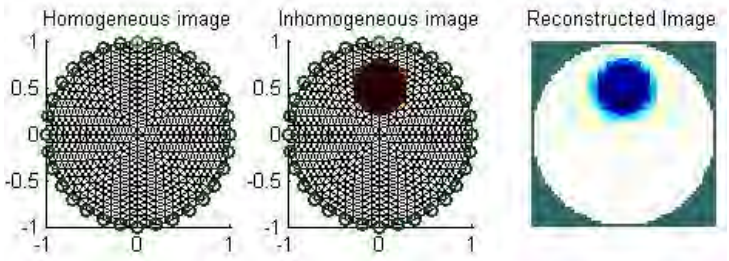

(a) Finite Element Mesh (left), simulated object (center) and reconstructed image from raw input/output data(right)

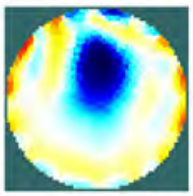

(b) Reconstructed image using impulse responses of CDM EITS

Figure 4.5: Reconstructed images of inhomogeneous object placed at 12 O'clock in the phantom using CDM EIT.

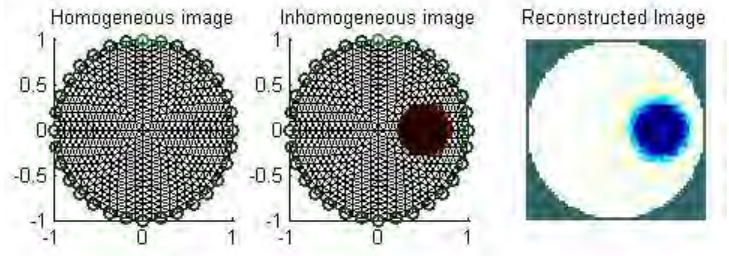

(a) Finite Element Mesh (left), simulated object (center) and reconstructed image from raw input/output data(right)

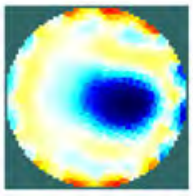

(b) Reconstructed image using impulse responses of CDM EITS

Figure 4.6: Reconstructed images of inhomogeneous object placed at 3 O'clock in the phantom using CDM EIT.

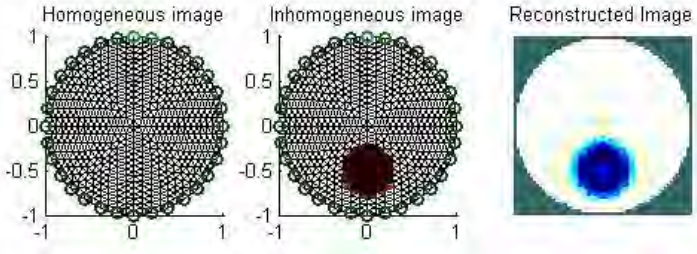

(a) Finite Element Mesh (left), simulated object (center) and reconstructed image from raw input/output data(right)

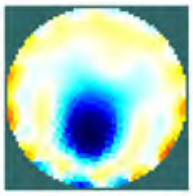

(b) Reconstructed image using impulse responses of CDM EITS

Figure 4.7: Reconstructed images of inhomogeneous object placed at 6 O'clock in the phantom using CDM EIT.

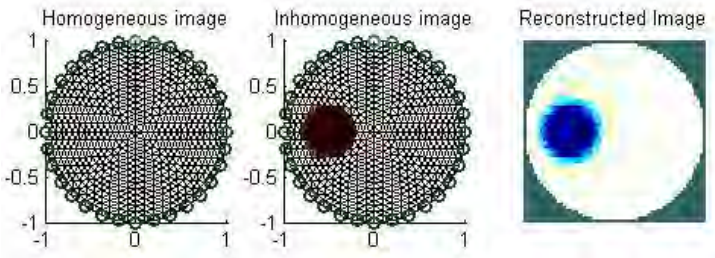

(a) Finite Element Mesh (left), simulated object (center) and reconstructed image from raw input/output data(right)

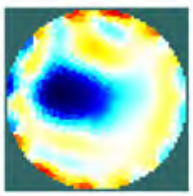

(b) Reconstructed image using impulse responses of CDM EITS

Figure 4.8: Reconstructed images of inhomogeneous object placed at 9 O'clock in the phantom using CDM EIT.

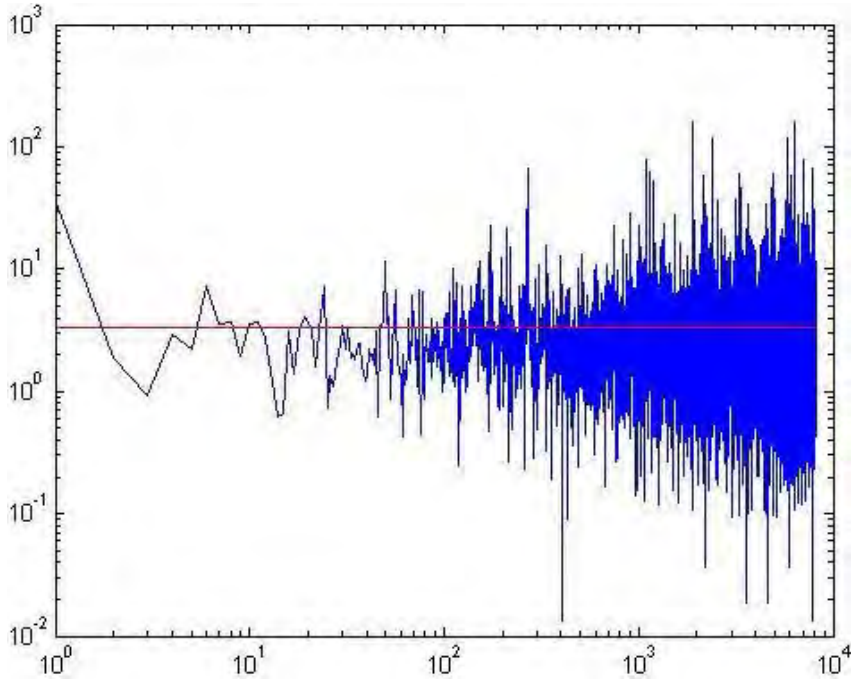

Figure 4.9: A sample magnitude Bode plot from a single input/output channel showing spectral contamination and a polynomial fit used to approximate the actual magnitude plot.

For the above simulation results, the simulation configuration used is as depicted in Figure 3.2.

4.3 Results Discussion

In general, the results obtained in this chapter through EIDORS simulations confirm that pseudo-random binary codes can be used for system identification accurately. Furthermore, the results show that CDM can be used as a multiplexing method for simultaneously injecting Gold current patterns for EIT measurements and reconstructing the conductivity distribution within the imaged object.

4.3.1 Single Code Identification

The application of a single 1024 *chips* Gold code as an input for identifying an RC low pass filter shows accurate results in predicting the gain and bandwidth of the circuit, with a bandwidth error of 19 Hz from a nominal bandwidth of 589 Hz. In addition to

the prediction of the circuit parameters, it was discovered that the non-ideal correlation properties of the Gold code necessitate a division by the auto-correlation (effective input) of it in order to extract the impulse response of the circuit. The extracted magnitude bode plot showed spectral contamination due to the non-idealities of the correlation properties of the Gold code and measurement noise. Tapson and colleagues in [7] reported an increase in spectral error of 0.41% when an extra code is simultaneous injected.

4.3.2 CDM EITS

Simulation of a full 32 electrode CDM tomography system with 16 differential voltage measurements on a separate set of electrodes and 15 injected Gold code current patterns with 1 common ground electrode, show that CDM can be used to image conductivity distributions of objects. This is evident in the detection of object placed at selected locations within the phantom as shown in Figures 4.5, 4.6, 4.7 and 4.8. The reconstructed images also shows that there are some errors in the reconstruction with the reconstructed object size and location, of 11% and 7% respectively, on average.

Through the analysis of the reconstructed images using the MATLAB image processing toolbox several measures of performance can be extracted. In this analysis the location and centroid of the object within the phantom are extracted by gray-scaling the Red, Green and Blue planes of the reconstructed images. It was observed that this process separates the reconstructed and reconstruction artifacts such as ringing and effects of noise in to different planes: Green and Blue respectively. Using the Green plane, and a magnitude pixel plot along the the middle of the plane (along x or y axes), the radius and centroid of the reconstructed object can be determined, and used to compute the position and location errors. The reconstruction artifacts are used by computing the standard deviation of the Blue plane, which is used to divide the maximum pixel value in the Green plane. Both the Green and Blue gray-scaled planes are inverted before processing so that the background color (zero conductivity change) has a pixel value of zero and not 255 in the gray-scale range. Figures 4.10, 4.11, 4.12, 4.13, 4.14 show the images and plots used to compute the indices for simulated inhomogeneous objects at selected locations in the phantom.

Based on the computations performed from these images and plots, the performance measures in Table 4.2 were computed. It is to be noted that while it is more convincing and technical to compute these values from image processing, these values were found to be in close agreement with the values computed through manual measurements on images,

with the exception of the SNR which whose computation involves the knowledge of each pixel value. Furthermore, while the pixel values serve as a good computation variable, the discretization error of the gray-scale $(0 - 255)$ introduces some quantization error. The merits of this approach however as opposed to the approaches proposed in [91; 22] is that only the reconstruction images and actual images are needed for the computations, as opposed to the need for raw data from EIDORS processing which is seldom available to consumers of reported works.

Table 4.2: Performance indices of CDM EIT simulations in EIDORS

Index	**3 0'clock**	**6 O'clock**	**9 O'clock**	**12 O'clock**	**Center**	**Average**
PE	11%	10.9%	12.4%	11%	3.2%	9.7%
SE	20%	12.7%	22.6%	20%	19%	18.7%
NER	25.7%	25.5%	27.1	26.3%	27.3%	26.4%
D	15.6%	16.2%	20.7%	18.8%	16.5%	17.6%

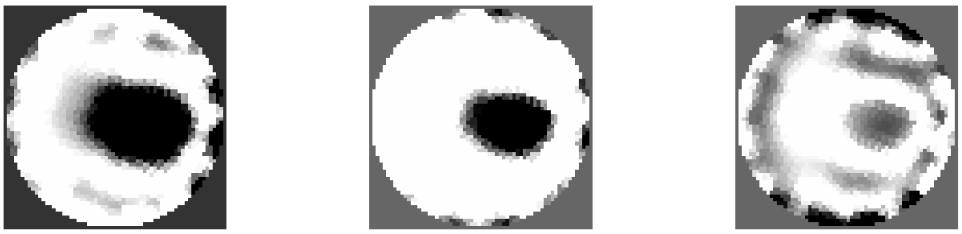

(a) Gray scaled Red, Green and Blue (RGB) planes of the reconstructed image, from left to right. The Green plane shows the reconstructed object, while the Blue Plane shows the ringing and image artifacts.

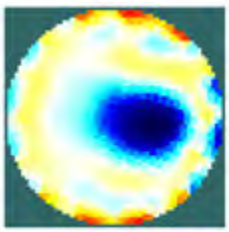

(b) Reconstructed image using impulse responses of CDM EITS, for comparison

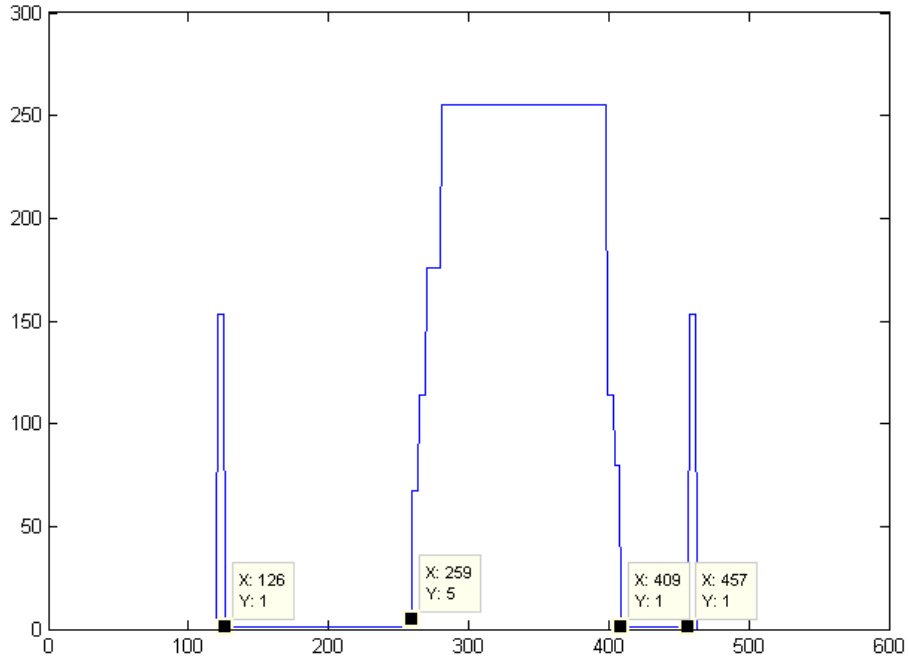

(c) Pixel magnitude plot along the middle horizontal line, plotted against pixel number.

Figure 4.10: Processing of reconstructed image at 3 O'clock to extract size, location, and centroid.

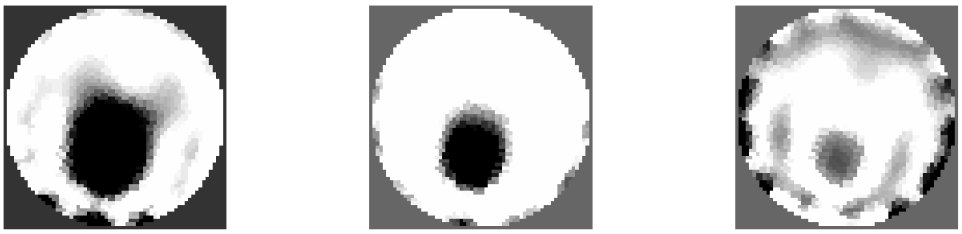

(a) Gray scaled Red, Green and Blue (RGB) planes of the reconstructed image, from left to right. The Green plane shows the reconstructed object, while the Blue Plane shows the ringing and image artifacts.

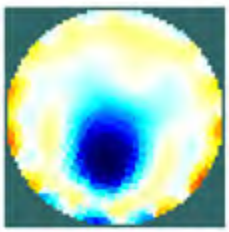

(b) Reconstructed image using impulse responses of CDM EITS, for comparison

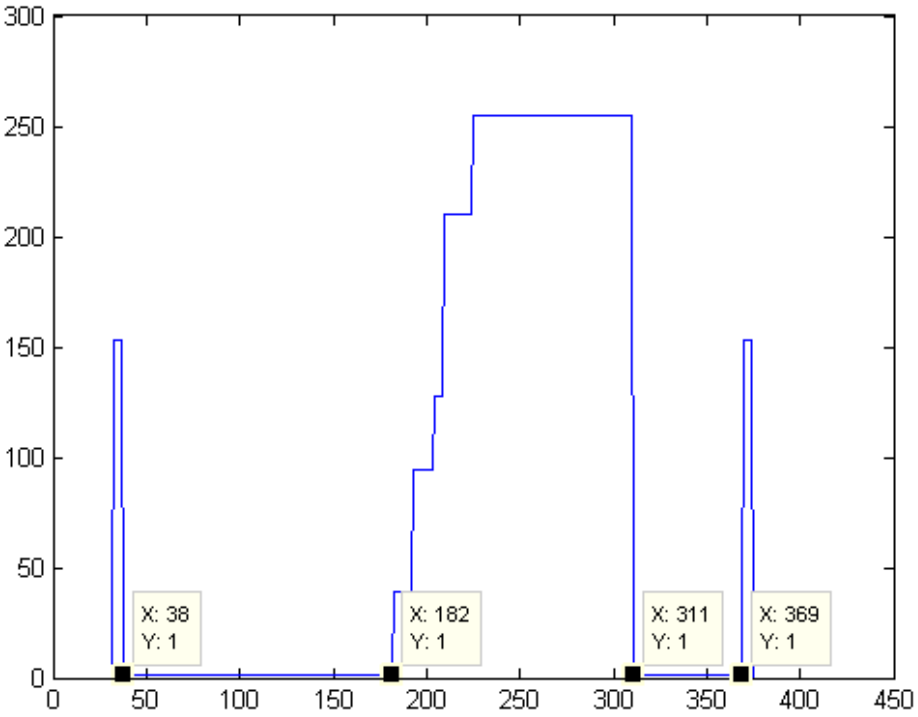

(c) Pixel magnitude plot along the middle horizontal line, plotted against pixel number.

Figure 4.11: Processing of reconstructed image at 6 O'clock to extract size, location, and centroid.

(a) Gray scaled Red, Green and Blue (RGB) planes of the reconstructed image, from left to right. The Green plane shows the reconstructed object, while the Blue Plane shows the ringing and image artifacts.

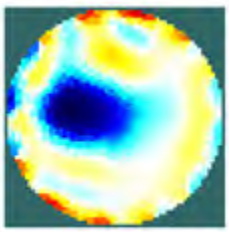

(b) Reconstructed image using impulse responses of CDM EITS, for comparison

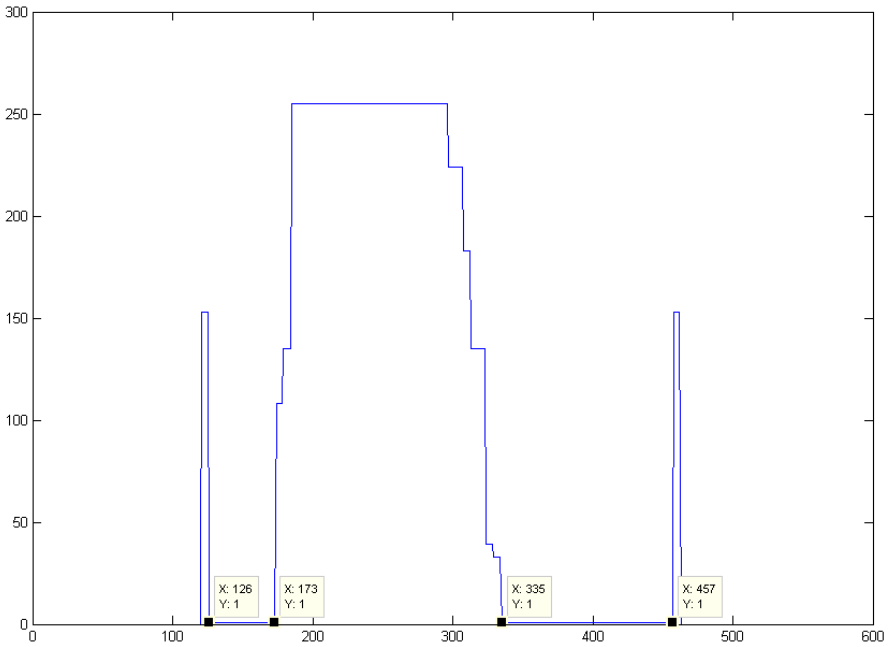

(c) Pixel magnitude plot along the middle horizontal line, plotted against pixel number.

Figure 4.12: Processing of reconstructed image at 9 O'clock to extract size, location, and centroid.

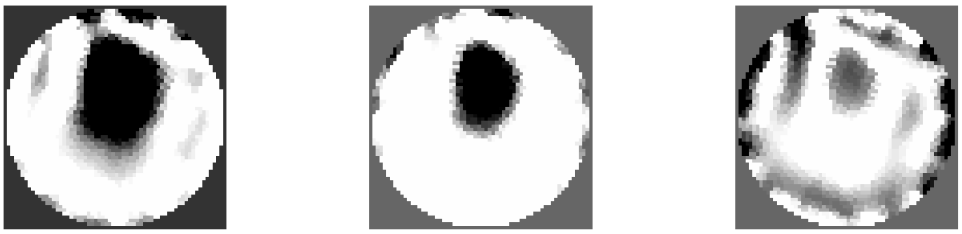

(a) Gray scaled Red, Green and Blue (RGB) planes of the reconstructed image, from left to right. The Green plane shows the reconstructed object, while the Blue Plane shows the ringing and image artifacts.

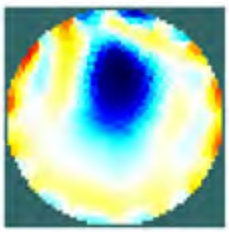

(b) Reconstructed image using impulse responses of CDM EITS, for comparison

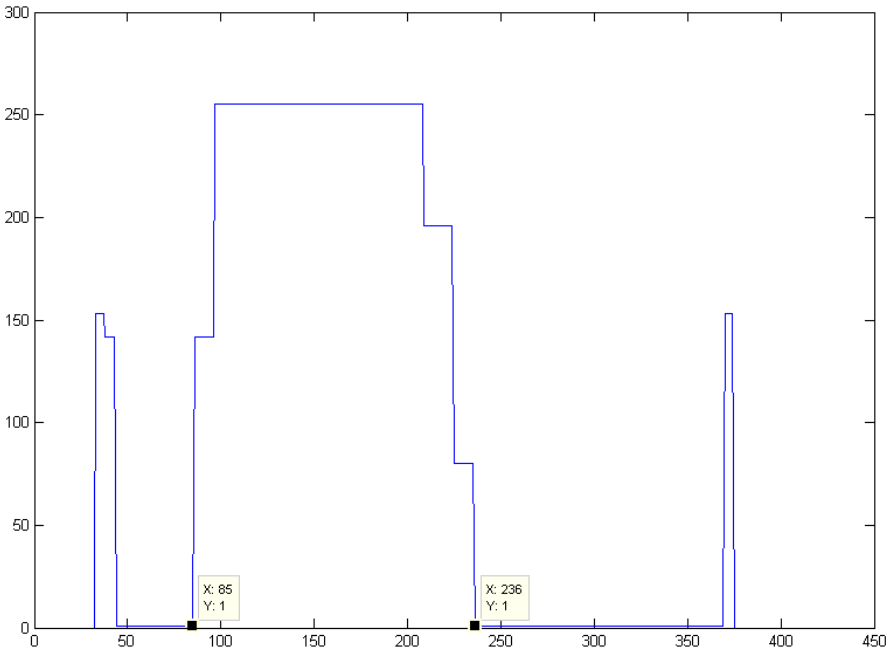

(c) Pixel magnitude plot along the middle horizontal line, plotted against pixel number.

Figure 4.13: Processing of reconstructed image at 12 O'clock to extract size, location, and centroid.

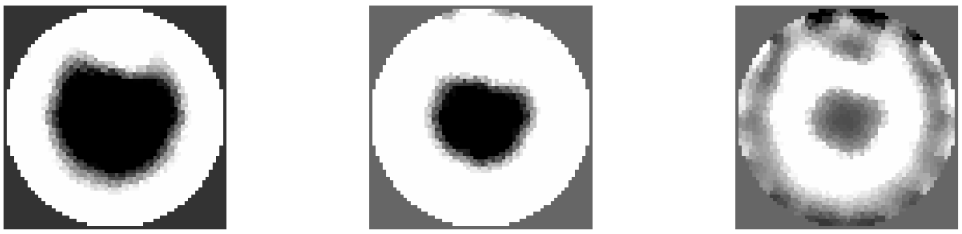

(a) Gray scaled Red, Green and Blue (RGB) planes of the reconstructed image, from left to right. The Green plane shows the reconstructed object, while the Blue Plane shows the ringing and image artifacts.

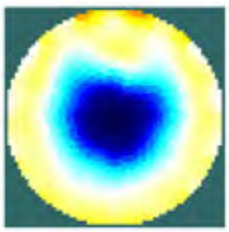

(b) Reconstructed image using impulse responses of CDM EITS, for comparison

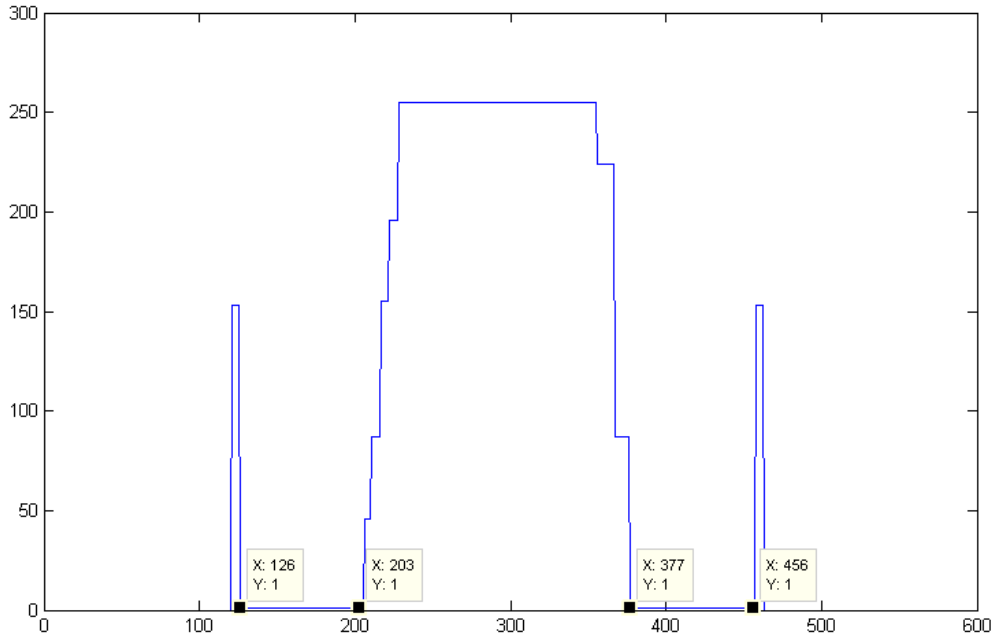

(c) Pixel magnitude plot along the middle horizontal line, plotted against pixel number.

Figure 4.14: Processing of reconstructed image at the center to extract size, location, and centroid.

On the basis of size and position error the results of the simulation study are comparable to those reported by Fabrizi in [94]. Furthermore the results of a Time Multiplexed system using Gold codes as current patterns in [7] showed position and size errors of 11.7% and 10% respectively for a banana object occupying 10% of the phantom at 2 kHz. The system of Granot [5] using Frequency division multiplexing with simultaneous injection and measurements gave size errors to a maximum of 20% when an object occupying 31% of the phantom was placed in the vicinity of the common ground electrode, and 10% at the center of the phantom. From the results presented by Wilkinson and colleagues [4], and circular object 50 mm in diameter placed in a circular phantom of 350 mm diameter was reconstructed showing a size error of approximately 9.2%. It is therefore, concluded from the comparative studies that a simultaneous injection and measurement tomography system using CDM with Gold pseudo-random binary codes is viable for imaging conductivity distributions in EIT. The resulting magnitude bode plots when 15 Gold codes are injected simultaneously at a sample rate of 4 samples/chip bears a significant amount of spectral contamination and necessitates the use of line fitting or a smoothing algorithm in order to extract accurate values out of it, as can be seen in Figure 4.9. Compared to the bode plot in Figure 4.4 the increase in spectral contamination can be seen.

4.4 Conclusions

White noise can theoretically be used to identify frequency responses of systems. However, it is difficult to generate white noise practically. Pseudo-random binary codes are used to approximate white noise with a defined time period. Several pseudo-random binary codes are available with varying correlation properties and lengths. Gold codes are preferable over available alternatives due to their correlation properties, ability to produce many codes of the same length (8, 16, 32, 64) needed for simultaneous injection CDM tomography, and the ease with which they can be generated. The use of pseudo-random binary codes to identify impulse responses suffers from spectral contamination due to their non-ideal correlation properties, but the method produces accurate results. Simulations of simultaneous current injection using Gold codes and simultaneous measurement of voltages show that it is possible to use CDM in EIT and that the results obtained are of comparable quality to reported results using TDM and FDM methods. The results show: 9.7% position error, 18.7% size error 26.4% Noise Error Ratio and 17.6% detectability error.

Chapter 5

System Design

In this chapter, a *Systems Design* approach is taken in designing an experimental platform to be used in this research. This begins with a motivation for the development of a Tomography system based on different principles to existing TDM and FDM platforms. Thereafter, requirements and specifications for the envisaged system are given. These include, *functional*, *non-functional* and *biomedical* requirements. The above are presented along with a synthesis of technical specifications that are used to guide the design choices and selections. A few design concepts are then suggested and evaluated using a scoring table against the requirement specifications. The selected design is then passed forward for detailed simulation, and design, which are presented in the two chapters that follow.

5.1 Needs and Motivation for System

1. Injection Time and Frame Rates
   Current systems, such as the UCL Mk2.5 and KHU Mk1 use TDM injection protocols [94]. While these systems are well designed and functional, their current injection and measurement times, can be improved by using the simultaneous injection and measurement protocol, resulting in better frame rates. They do however, have an advantage inherent in their design of low/no interference among driving and measurement electrodes. An alternative to systems based on TDM is based on FDM. However, due to the use of different frequency bands for different injecting electrodes in FDM, spectroscopy and frequency difference imaging become impractical. Therefore an alternative approach which allows frequency difference imaging and spectroscopy while providing good spatial (image quality) and temporal (frame rates) resolution, is sought.

2. Data Inconsistencies
   The fact that TDM systems inject currents and measure voltages at different times in a sequential manner, means that for fast changing systems these systems become inapplicable as they will result in inconsistent temporal data. FDM systems also result in inconsistent data if the frequency bands assigned to each current injection electrode are chosen over a range of frequencies that contains large changes in impedance. The insufficiency of these two multiplexing schemes motivates for a system that uses CDM to allow collection of temporal data from all electrodes while currents are injected concurrently, and excites the same frequency range through all injected currents, to avoid inconsistencies caused by FDM.

3. Signal Energy
   The ability of a system to easily perform spectroscopy and frequency difference imaging is based on how easily it provides access to frequency response of the imaged object. While for FDM the above concepts are completely unrealistic, for TDM, the frequency responses can be obtained by application of known inputs $U(jw)$ and computation of the resulting transfer functions $G(jw) = \frac{O(jw)}{U(jw)}$ using the resulting outputs $O(jw)$ after a Fourier transformation. The problem with this approach is that the energy of most of commonly used input functions such as a step or pulse, do not contain evenly distributed energy over all frequencies in the selected range. PN codes poses this desirable property.

4. Electrically Active Objects
   When imaging electrically active objects such as active muscle or brain tissue, there maybe signals originating from inside the imaged space. Depending on the frequency at which these internal signals occur, they can cause errors in the measurement systems involving TDM and FDM. In CDM the cross-correlation process at the measuring electrodes renders such interfering signals as very low energy noise which (theoretically) does not cause much problems.

5.2 Specification

Based on the specifics of the imaging task and object type, the requirements of the designed EITS system vary. A particular envisaged application of this system is brain imaging for diagnosing of stroke, effects of which can occur at low frequencies around 100 Hz and as high as 1 MHz. Furthermore, biomedical quality, reliability and safety standards as stipulated in the IEC 601-1, IEC 601-1-2, IEC 601-1-4 and ISO 13485, 13488 and 14969, have to be observed in the design of such equipment. The specifications are

given in three separate subsections starting with functional specifications, then biomedical considerations and finally non-functional specifications of the device.

5.2.1 Functional Specifications

Signal Levels and Compliance

With medical applications in mind, injected current levels are dictated by biomedical findings that, human beings can sense a current of level 1 mA flowing through them, at 1 kHz. This amplitude is larger at lower frequencies and must be lower at higher frequencies. This value takes into account the fact that the heart is most vulnerable to currents at a frequency of 60 Hz, and the value can be raised with increasing frequency [23; 36]. Typical impedance levels of the human skin transfer impedance are in the range 100 - 10 kHz. These impedances combined with the safe current magnitude give a voltage compliance of 10 V for the current sources [101].

Signal Frequencies and Excitation Rates

From the application specific operating frequency range of 100 Hz to 1 MHz it is desired that the equipment have a bandwidth to accommodate that. In addition, the driving signal produced by the signals (PN codes) from the waveform generator need to be at a frequency dictated by the desired imaging frame rate. For the purpose of this research work, any frame rate of above 10 frames/s will be deemed sufficient. Using PN codes of 1024 bits length, this translates to a period of less than 0.2 ms, 0.02 ms for 100 frames/s and 2 μs for 1000 frames/s.

Number of Electrodes and Resolution

It is desired that a setup of 8 or 16 electrodes along each plane of imaging be designed and the measurement be at accuracy levels of 0.1%. With a 3D measurement obtained using 3 planar measurement this can lead to 48 electrodes at most. If all these electrodes act simultaneously, then the worst case accuracy requirement is 0.002% on each electrode, or 0.006% for a 16 electrode single plane system. In addition to the electrodes above, it is necessary that the number of electrodes be kept as few as possible. This therefore

implies that if possible, split current injection and voltage measurement electrodes are to be avoided for complexity and spatial resolution. An accuracy of 0.002% would require a data acquisition resolution of 16 bits or more, in which case an accuracy of LSB would satisfy the requirement.

5.2.2 Biomedical Safety Considerations

In order to ensure the safety of life imaging subjects, the final device has to conform to biomedical safety requirements, and these are itemized below.

- Equipotential grounding between all devices to avoid leakage current flows.
- Patient isolation for protection from active electronics using transformers or opto-couplers.
- Over-current protection to avoid affecting bodily function, through the use of fast acting fuses.
- Patient protection from physical irritation due to electrodes, adhesives and saline solutions.
- Patient isolation from environment to prevent fault currents from flowing to ground through sensitive body parts such as the heart and brain, in the operating rooms.
- Fail safe software and hardware states within the system.

5.2.3 Non-Functional Requirements

These are specifications that do not dictate the operation of the device and have no bearing on the safety of live subjects, on whom the device maybe used. They are mainly ergonomic and economic requirements.

- The cost of the device should be kept as low as possible, compared to to the commercial systems which cost about $400000.00ZAR$.
- The platform should be light weight and portable for possible use in an ambulance, or mobile platform.

- The platform should be capable of deriving power from a 12 V battery or vehicle power outlet.

5.3 Device Concepts

Besides a computer needed for signal processing and reconstruction, the largest cost of cost of the system is for the data acquisition hardware. This comprises the platform for generating the binary random codes, and for measuring surface voltages. Several options are available for PN code generation through digital synthesis. Some of these are discussed below, along with voltage measurement hardware.

5.3.1 Concept One: Personal Computer and Interface Cards

Hardware and Software speciciations:
The use of a Personal Computer (PC) through a data acquisition card is used as a first option due to its simplicity of implementation. However this approach is not favorable due to the cost of multi-IO high frequency cards. Two μDAQ data acquisition cards from Eagle Electronics: USB30D-32 and PCI766-24, are used for ADC and DAC respectively. The output card can provide refresh rates of 100 kS/s per channel over 24 channels, and the input card provides 1 MHz sampling rate shared among 32 channels for boundary voltages and measurement of injected currents to be used in the cross correlation process. Experiments are done using only 16 channels for boundary potentials, to be correlated with measured current patterns because of lack of synchronization that arise if the currents are not measured. This will enable sampling rates of about 31.25 kHz per channel. These are interfaced to a PC running Windows XP, with 2 GHz dual-core duo processors, and 2048 MB RAM. The software used is developed in both C# and MATLAB, for data acquisition and image reconstruction. The output card has a range of ± 10 V while the input card has a range of ± 5 V. This necessitates scaling of input voltages to accommodate the possible voltage compliance of the system. A complete block diagram of the system used here is provided Figure 5.1, for an 8 electrode system.

Limitations Imposed by Hardware:
According to the hardware specifications above, the maximum frequency at which the imaged object can be interrogated is $\frac{f_s}{2}$ where f_s is the sampling frequency. This therefore means that spectral data up to 15 kHz using a 16 electrode system with 16 current sensing

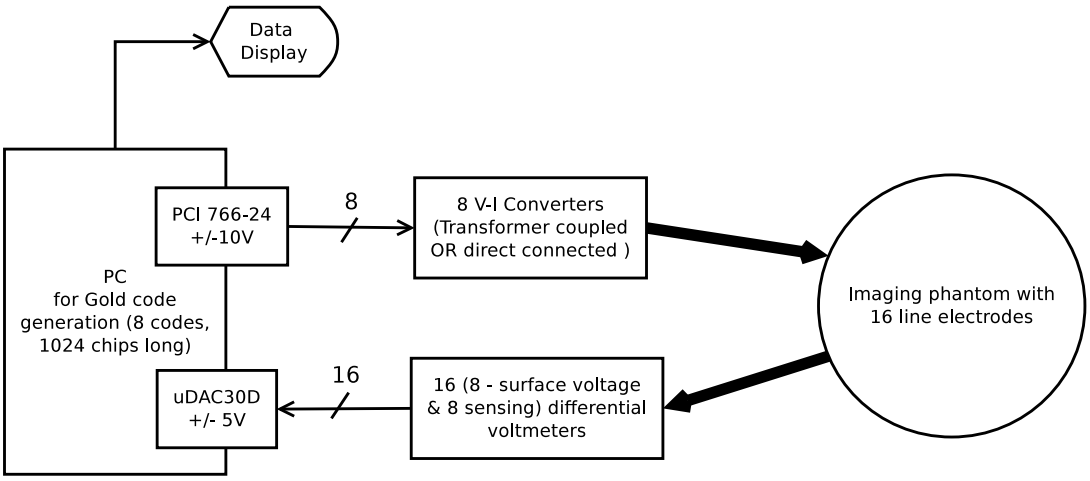

Figure 5.1: An illustration of a 8-electrode tomogram using only the μDAQ30D.

electrodes. Furthermore, even though the output card can generate 100 kHz per channel. The maximum that can be handled by the input card allows only outputs of 15 kHz.

5.3.2 Concept Two: Personal Computer and Micro-controllers

In most applications of microprocessors for generation of signals, the samples of the respective signal are stored in memory and clocked out. This becomes simpler if the signals are periodic. This approach however poses a problem if the signals are aperiodic and contain many samples, due to the limited memory in microprocessor platforms. In testing this approach, instead of storing the pseudo-random codes on the microprocessor memory, the codes are synthesized from the basic principles and then written to the output ports of the micro-controller. C++ code was written for a Arduino Mega 2560 micro-controller to drive 8 digital outputs with the Gold codes. Attained speed was 10 code periods per second, which would be halved if 16 codes were used. The device was used with the μDAQ card discussed earlier. This platform allows higher frequencies but the phase shifts between the codes become a significant problem, which can be corrected at the cost of more complex electronics. Another problem of micro-controllers is that the produced Gold codes are between 0 and 5 V which then needs to be DC shifted to $\pm$2.5 V. The biggest disadvantage of micro-controllers is the fact that they usually possess a single Analog to Digital Converter (ADC) that needs to be multiplexed, reducing the attainable sampling rates to unacceptable levels. This necessitates the use of a different voltage input card with higher sampling rates. A block diagram of this concept is shown in Figure 5.2

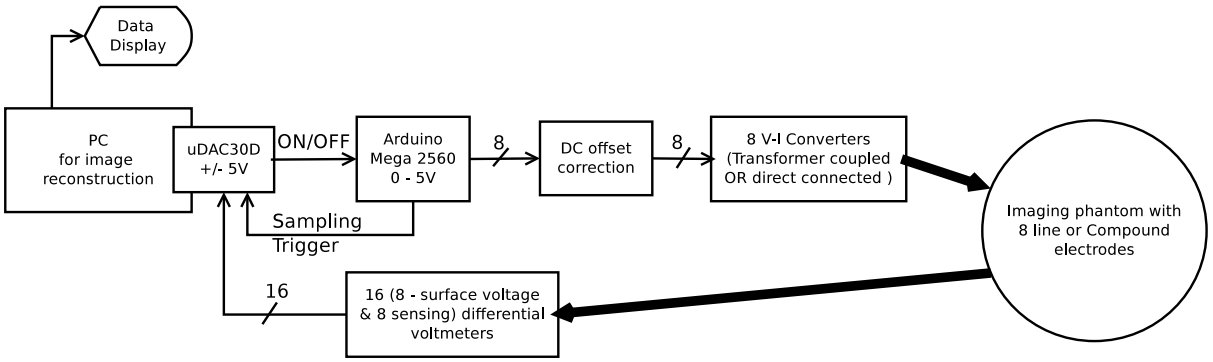

Figure 5.2: An illustrative 8-electrode tomogram using the Mega 2560 and μDAQ30D.

5.3.3 Concept Three: Personal Computer and FPGA

A VHDL implementation of the pseudo random codes was used to synthesize the required codes on a Cyclone EP1C12 FPGA. The development of the VHDL code was done using the Qucs, ModelSim and Web Edition of Altera's Quartus II software. The timing simulation results performed on this platform showed that the device shares some of the disadvantages of the μController problems while being slightly more costly. An alternative stand alone FPGA based platform considered was the National Instruments RIO 9612 platform with 32 voltage inputs at 250 kHz sampling distributed among all channels, while this platform would suffice for concept testing, it can only interrogate frequencies up to 3 kHz on the imaged object when used on a 16 simultaneous injection and measurement system. Faster FPGA based devices are mostly PCI, PXI or PCI-Express connected. This concept is illustrated in Figure 5.3

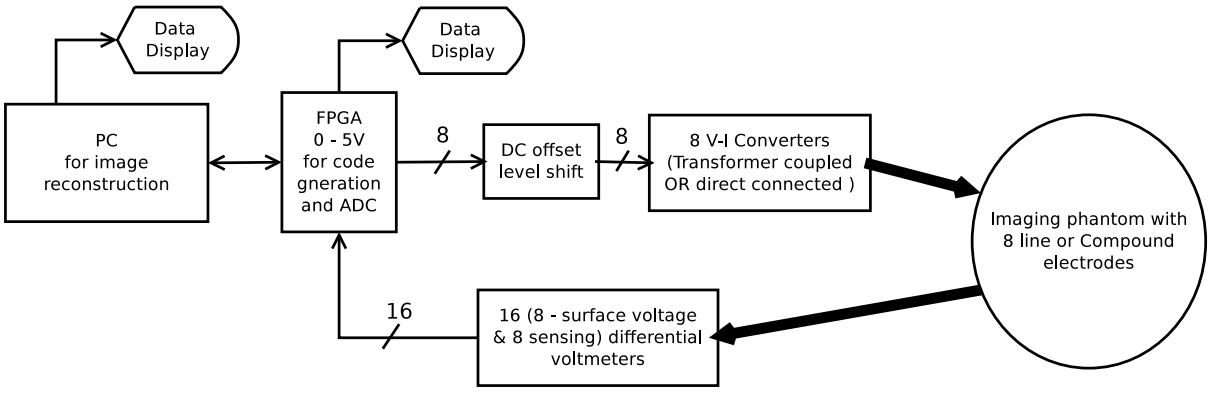

Figure 5.3: 8-electrode tomogram using a FPGA (Cyclone EP1C12).

5.3.4 Concept Four: Industrial Computer and FPGA

This concept uses an industrial PXI computer backplane. Attached to the backplane is a computer board and memory (Random Access Memory) expansion for reconstruction and external communications such as Ethernet. Also attached to the backplane is an FPGA device that is responsible for interfacing to the analog electronics: analog multiplexers, digital-to-analog (DAC) converters, analog-to-digital (ADC) converters and programmable gain amplifiers (PGA). The FPGA connects to three modules of such devices to allow 3 imaging planes for use in 3D imaging. Furthermore, the FPGA is responsible for excitation signal generation (16 signals per plane), processing of measured voltages (16 voltages per plane) using correlation, fast Fourier transform and filtering operations. These tasks are placed on the FPGA to limit the amount of data that goes onto the PXI backplane to the reconstruction computer board. The analog devices used have to be high bandwidth (100 Hz to 1 MHz), and tightly synchronized by the the FPGA. A similar implementation is that of the OXBACT-5 reported by Yue and McLeod in [102]. Their platform achieved 25 frames per second using 16 current injections and 62 voltage measurements per plane. In order to achieve the desired measurement accuracy, DAC devices used must have more than 16 bit resolution. This concept is illustrated in Figure 5.4 The cost of this concept is estimated at $400000.00 ZAR$.

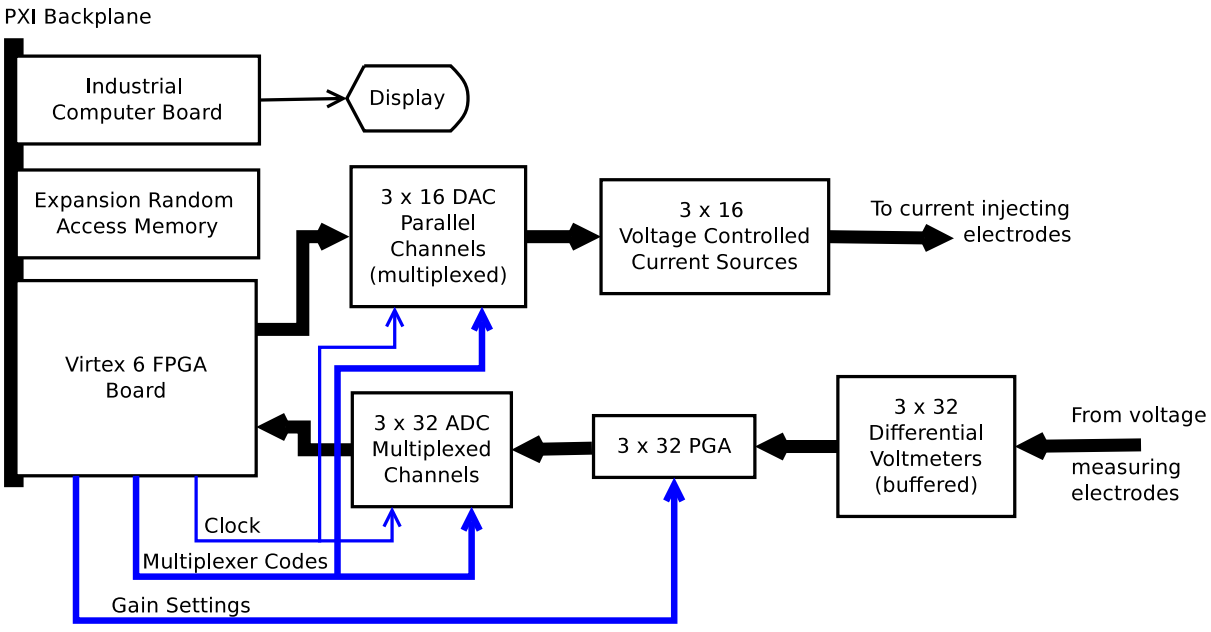

Figure 5.4: A 3D, 3 plane industrial computer and FPGA based EITS system architecture. A downgrade of this configuration to a 2D capable system will only reduce the cost by $30000 ZAR$.

5.3.5 Concept Evaluation

The concepts above are evaluated towards achieving the specifications using a scoring Table 5.1. Within the functional specifications listed earlier, the scoring weights are allocated as follows: *outputrate* = 25%: this scaling factor is selected as such because the output rate influences the attainable frame rates which is an important aspect of the system and quality of the system if it contains too large phase differences between the injected signals, *inputrate* = 30%: this requirement is given the highest weight because it influences the attainable frame rates and the range of frequencies that can be interrogated in the imaging. This is important in spectroscopic imaging and frequency difference imaging which are vital in the proposed mode of imaging (CDM). The cost of development is is an important factor after the frame rate, hence it is given a score of *cost* = 15%. *portability* = 10%: all the proposed concepts have to be portable hence this weight is also chosen low. *needed analog electronics* = 20%: analog electronics in the system can introduce measurement and signal errors hence it is selected to have a moderate weight. The scoring of all concepts is done by considering their strengths and disadvantages discussed earlier.

Table 5.1: Concept Scoring Table

Specification	**Concept One**	**Concept Two**	**Concept Three**	**Concept Four**
output rate [25%]	10	5	8	25
input rate [30%]	10	5	10	30
electronics needed [20%]	20	5	7	0
portability [10%]	10	10	10	7
cost [15%]	15	15	10	0
Total Score [100%]	**75**	**40**	**45**	**62**

From Table 5.1, the first concept was selected as a good compromise between cost and performance and will be the one taken forth for detailed design and implementation. The analog electronics and additional aspects that follow are selected for this concept. Concept four is the ultimate implementation platform as it scores high on functional requirements and enables wider deployment of the developed system, however it is almost ten times the cost of all the other concepts which excludes it as a hypothesis testing prototype.

5.4 Current to Voltage Converters

Following the successful implementation and testing of Gold code generation software, is the design and implementation of current to voltage converters. While the single inverting Op-Amp sources (with and without transformer coupling) is desirable, a Howland source has been selected for implementation due to its lower cost and requirement for fewer electrodes. Simulations of the variants of the devices were performed, however the major considerations used to select the current sources was their resulting complexity. It is decided that to test the hypothesis of this work, a modified Howland source will be used with the OPA655 Op-Amp and ±1% tolerance resistors, due to its moderate requirement for electrode count between that of TDM systems and floating current sources using separate injection and measurement electrodes.

A two electrode measurement system was not used because floating two-point sources proposed by Tapson and colleagues [23] were tested and the results obtained when a ring of three current sources was closed around an RC circuit network, were not satisfactory. Their configuration using two sources and a resistor-capacitor network to simulate the imaged object, did not represent a complete closed ring of sources. Similar results for their scenario were obtained in testing however, upon closing the ring the results deteriorated badly. It is assumed that the results in [23], might have been acceptable because the current source ring used for experimentation was not fully complete, similar to the one they used to explain the practical scenario, or maybe due to lack of information on the authors part on the particulars of their implementation. In [27] a serial UCL Mk2.5 was reprogrammed with two Gold codes of chip length 1024, and used in a time difference multiplexed manner to successfully to produce results comparable to commonly reported results of FDM and TDM systems.

Figure 5.5 shows a schematic of the constructed modified Howland source [40]. The requirements are that $R_1 = R_2 = R_3 = R_4 = R$ and $R_5 = 2R, i_G(t) = -\frac{v_G(t)}{R}$

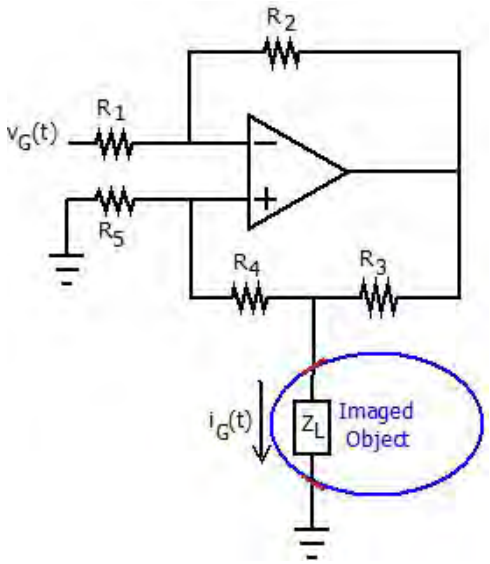

Figure 5.5: Modified Howland current source for Tomograph.

5.5 Voltage Meters

Differential voltage measurements are used to avoid large voltage ranges, common mode rejection and gain bandwidth. After considering two measurement variants, one using a difference amplifier and the other a Instrumentation amplifiers, it was decided to use AD620AN and INA128P Instrumentation amplifiers due to their superiority over difference amplifier configurations.

5.6 Electrodes and Phantom

A round plexy-glass bowl of radius 11 cm and height of 5 cm is used to mount the electrodes. A picture of the phantom and electrodes assembly is shown in Figure 5.6. Unscreened wiring of length less than 0.5 m is used between the current sources and voltage meters.

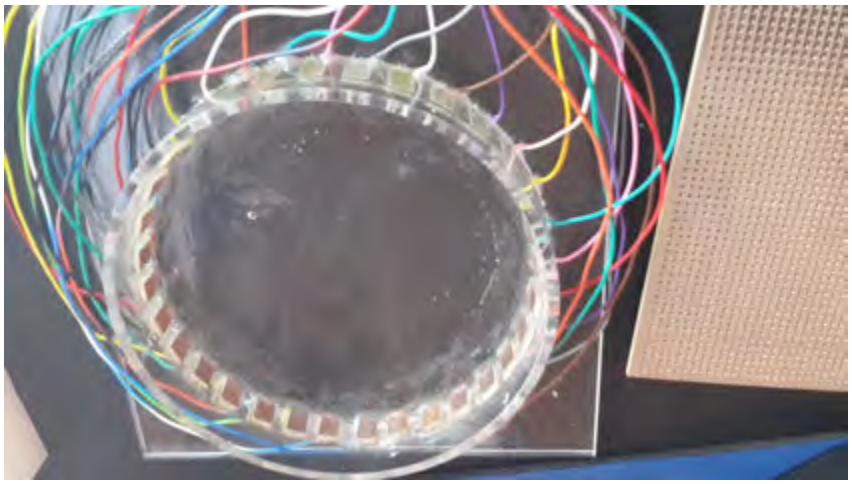

Figure 5.6: A phantom electrode assembly for use in the CDM EITS experimentation with 32 copper line electrodes.

5.7 Computer Interfacing

A 32 analog input USB30D-32 data acquisition card with 16 bit resolution and 1 MHz sampling frequency shared among used channels, ±5 V input range and a PCI766-24 output card with ±10 V output range and 100 kS/s refresh rate on each channel.

A block diagram of the complete single injection and measurement is given in Figure 5.7

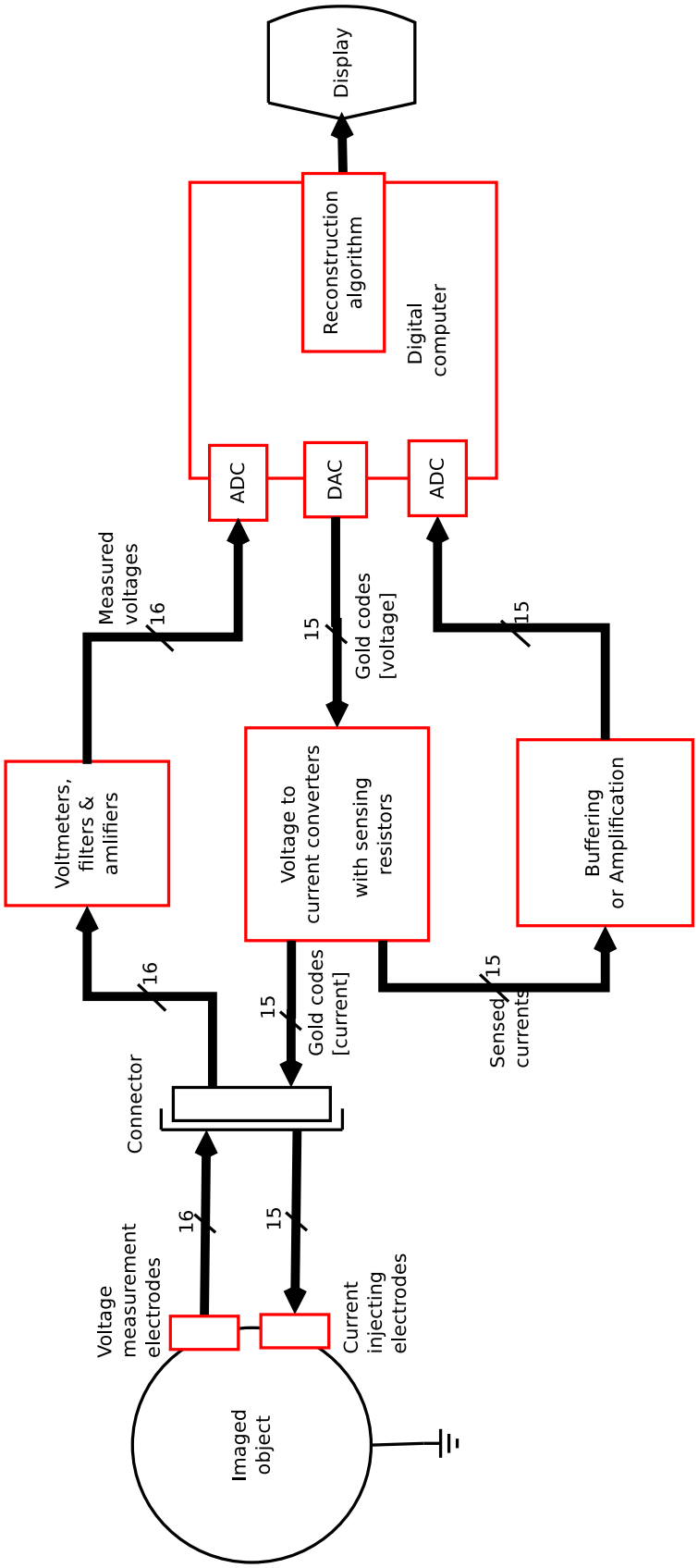

Figure 5.7: A block diagram of the completed CDM experimental system.

5.8 Conclusions

A 32 electrode EITS system with copper electrodes and a circular phantom, using CDM as a multiplexing method was designed. This system was designed to attain 14 frames/s in imaging speed. Out of several approaches, the design using a PCI data acquisition card with 100 kHz refresh rate for each of its 24 voltage outputs with ±10 V output range was chosen. The voltages were converted to currents using 15 modified Howland current sources made of OPA655 operational amplifiers and ±1% tolerance resistors. Voltages were measured in a differential manner using AD620AN or INA128P instrumentation amplifiers and ±1% resistors. These voltages were fed into a USB input device with 32 inputs multiplexed onto a 1 MHz analog-to-digital converter system, with input range of ±5 V. The control of the hardware and graphical user interface were developed in C#. The reconstruction software was implemented in MATLAB and EIDORS and interface to the C# control software using the Windows COM server. Biomedical safety and robustness considerations were given but not implemented as the current prototype is not intended for biomedical testing yet.

Chapter 6

System Testing

In this chapter, results are presented towards asserting the full functionality of the designed Tomography system. Furthermore, results of tests performed to address the hypothesis of the research work are presented and discussed, with reference to the different aspects of the hypothesis statement. Signals in the system are measured to check their integrity SNR and DC drift. Results from phantom imaging tests of several objects are also presented to confirm the success and quality of the designed system. In depth analysis of results and their comparison with results produced by equivalent technologies TDM and FDM, is reserved for the next chapter.

6.1 System Accuracy and Repeatability

In order to assess the performance of the designed data acquisition system, the level of zero input noise measurement needs to be established. Such results are shown in Figure 6.1. It can be seen that the peak-to-peak amplitude is at 0.025 V, and this is deemed reasonable since the system was designed to interrogate resistance values in the range 100 Ω to 10 $k\Omega$, with current amplitudes of up to 1 mA. This implies that minimum measurable data voltages will be 0.1 V which makes the noise level 25%.

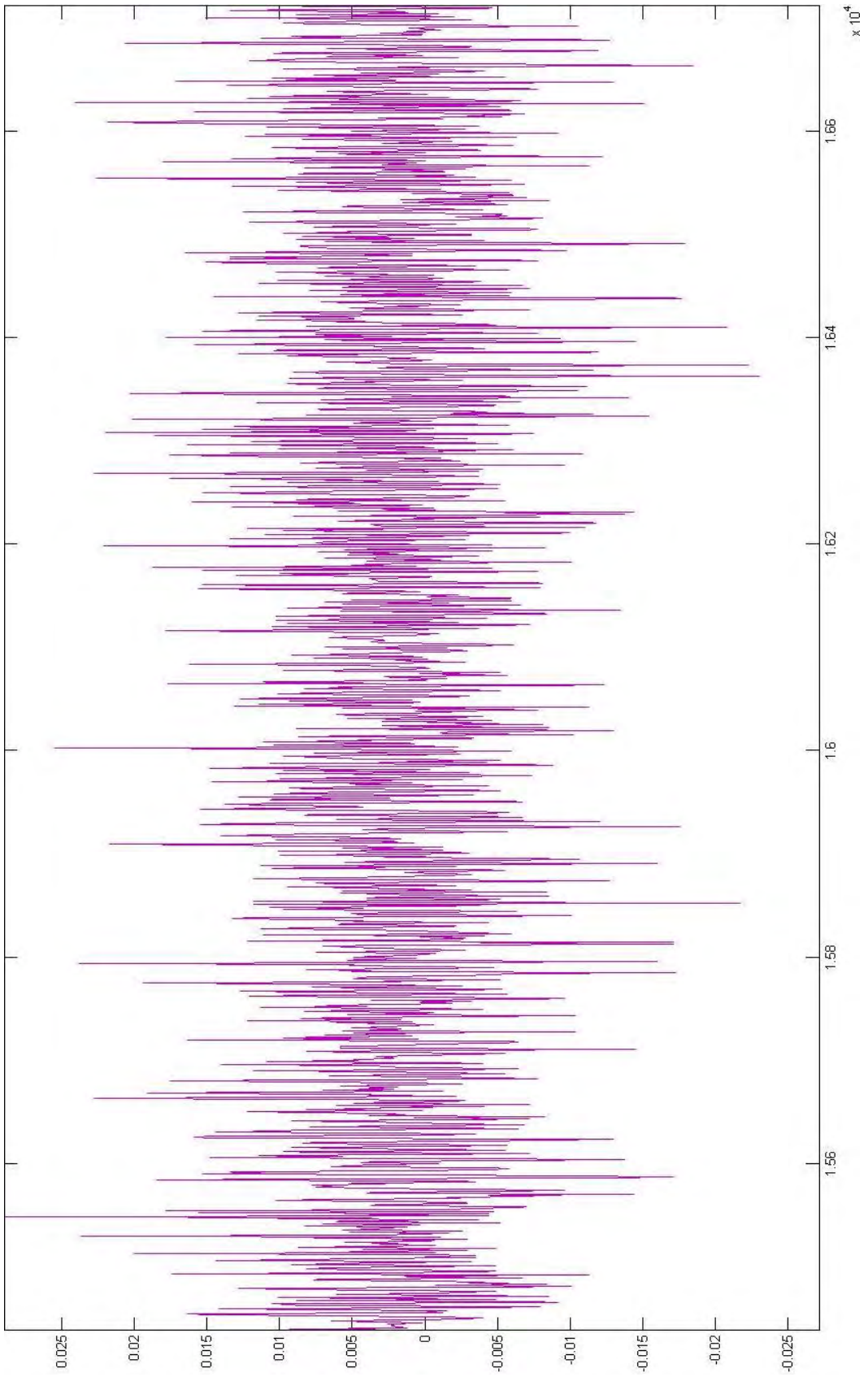

Figure 6.1: A plot showing zero input measurements in Volts plotted against sample number. The measurement shows a maximum amplitude 0.025 V.

For inspection purposes, the injected Gold codes are plotted using the acquisition software and shown in Figure 6.2, and samples of measured surface voltages are shown in Figure 6.3. This test and software feature is provided for visual inspection during experimentation. There is some fluctuation in amplitude of the Gold codes besides the logic changes. This is caused by *ghosting* due to the multiplexed nature of the USB30D input device, this phenomena becomes worse with increased sampling rates, signal amplitudes and is due to high output impedances of circuits connected to the input acquisition device. The remedies are: to lower such output impedances, lower the sampling frequencies, or connecting the inputs with the highest output impedance close to the ground connections of the acquisition device. However, these mechanisms do not completely eliminate this phenomena. The ultimate solution is to use a acquisition device with a separate ADC for each input channel and such have a higher cost than their multiplexed alternatives.

Figure 6.3, shows that for zero inputs (left edge of the plot), some of the measured outputs are not zero. This is due to DC bias within the imaging phantom. This DC bias has to be removed before results processing to avoid reconstruction errors. This can be achieved in software or through the use of high pass filters on the hardware measurement channels. It was opted that such corrective action be implemented in software for this work to reduce the electronics component count.

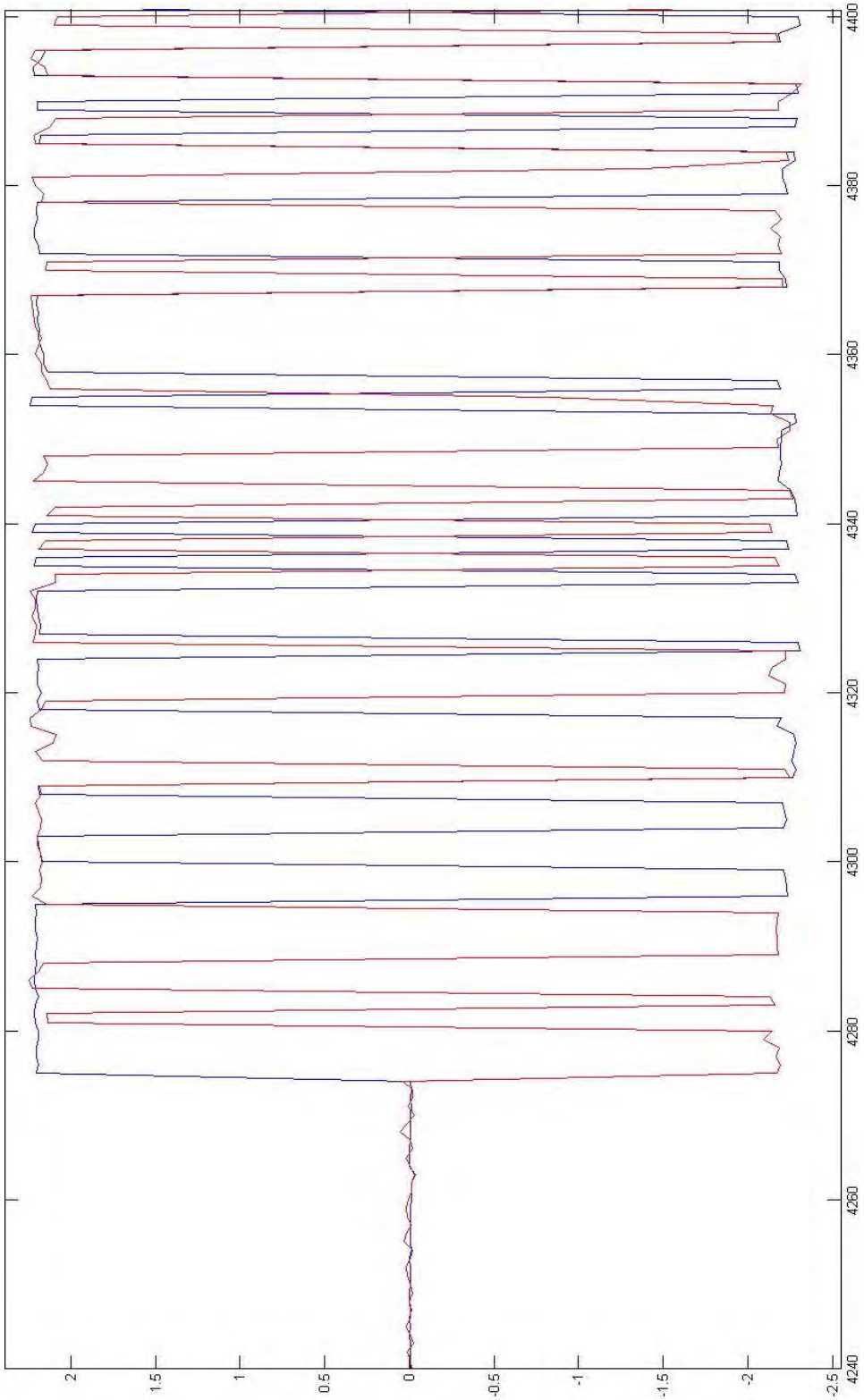

Figure 6.2: A sample of measured Gold codes as injected into the imaged object in Volts against sample numbers. Besides logic level changes effects of ghosting on a multiplexed ADC can be seen. These voltage patterns are used to drive the modified Howland current-to-voltage converters.

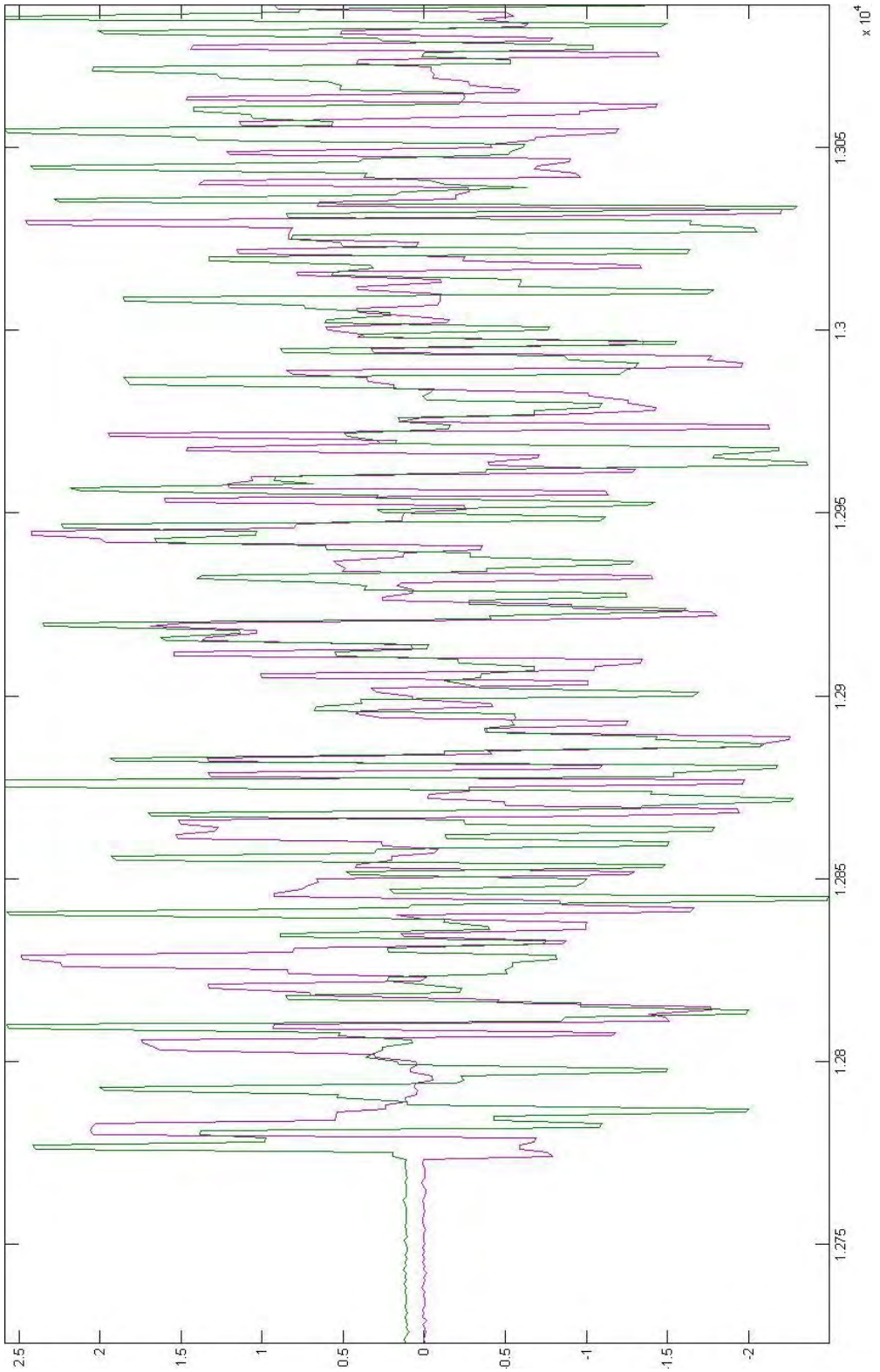

Figure 6.3: A sample of measured surface voltages showing clear distinguishability from each other. The magnitudes are volts plotted against sample numbers. The results further, show some DC bias in the measurement, evident on the left side of the plot during zero inputs.

6.2 CDM EIT Phantom Testing

To perform phantom tests, the phantom was filled with a *normal* NaCl saline solution - (1%) concentration, which is similar to to the NaCl concentration in the human body electrolyte. Gold code currents were injected into the phantom and measurements of a homogeneous impedance distribution taken. An object was then placed into the phantom (banana, cucumber and teflon). These objects are chosen due to their close impedance properties to human tissue (brain, electrolyte and bone). Another data set of measurements was taken after the object is introduced. The two data sets were used for time difference imaging in the following manner: each of the electrode outputs was cross-correlated with all the injected gold codes to extract the respective channel impulse response in accordance with the derivations of section 4.3. These impulse responses (magnitudes) are supplied to the reconstruction function in EIDORS for reconstruction. The impulse responses from both the homogeneous and inhomogeneous measurements are sampled at a chosen frequency w rad/s to give a set of channel impedances (impulse responses) between each of the 15 inputs and 16 measuring electrodes:

$\mathbf{V}_h(jw) = h_{h1}(jw), h_{h2}(jw), \ldots, h_{h240}(jw)$ and
$\mathbf{V}_i(jw) = h_{i1}(jw), h_{i2}(jw), \ldots, h_{i240}(jw)$ respectively.

These data sets were then subtracted to form a time difference data set used to reconstruct the impedance images. Figures 7.3, 6.5, 6.6 show reconstructions of a banana, cucumber and teflon object placed at various locations in the phantom using time difference imaging.

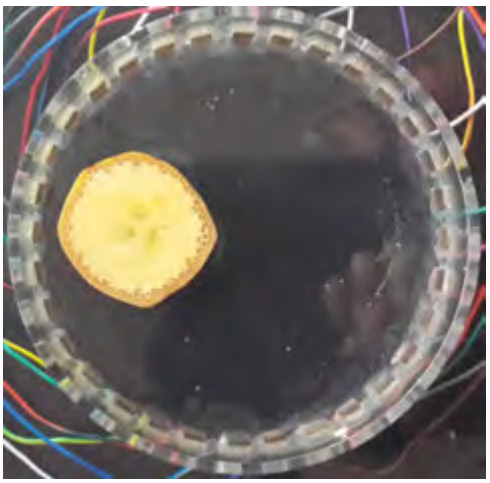

(a) Image of real banana object placed at 9 O'clock in the phantom

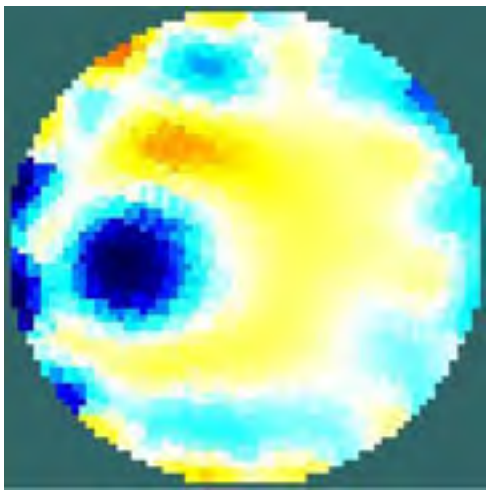

(b) Reconstructed image using impulse responses

Figure 6.4: Images of inhomogeneities (left images) placed at selected locations, and their reconstructed images (right images) using CDM EIT.

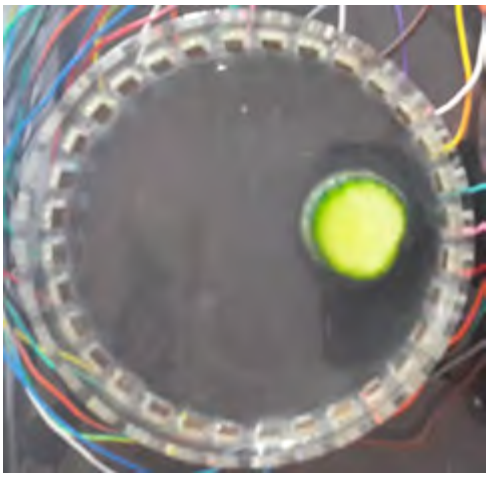

(a) Image of real cucumber object placed at 3 O'clock in the phantom

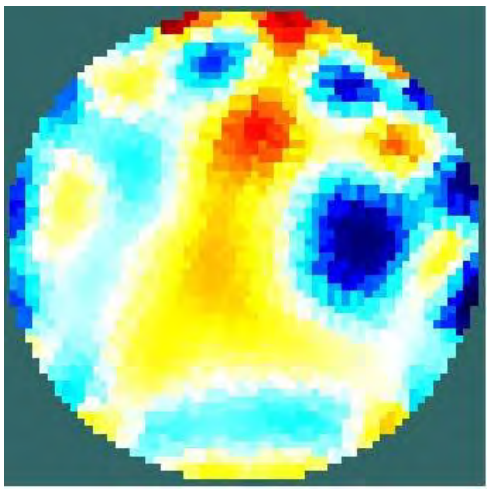

(b) Reconstructed image using impulse responses

Figure 6.5: Images of inhomogeneities (left images) placed at selected locations, and their reconstructed images (right images) using CDM EIT.

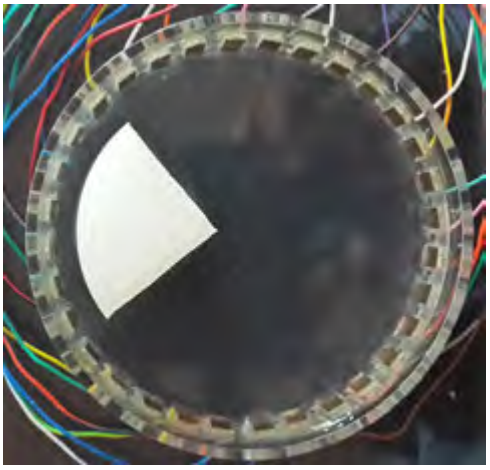

(a) Image of a block of polytetrafluoroethylene (teflon) placed at 9 O'clock

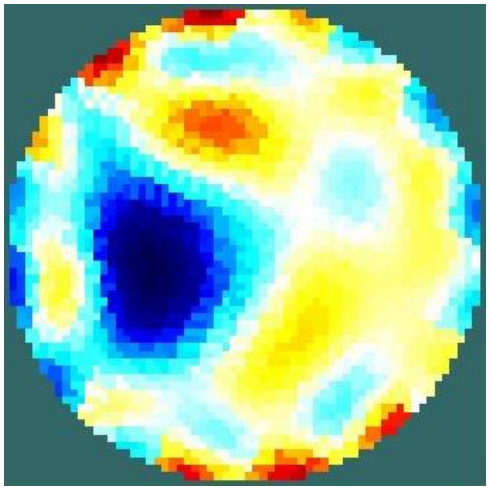

(b) Reconstructed image using impulse responses

Figure 6.6: Images of real objects (left images) placed at selected locations, and their reconstructed images (right images) using CDM EIT.

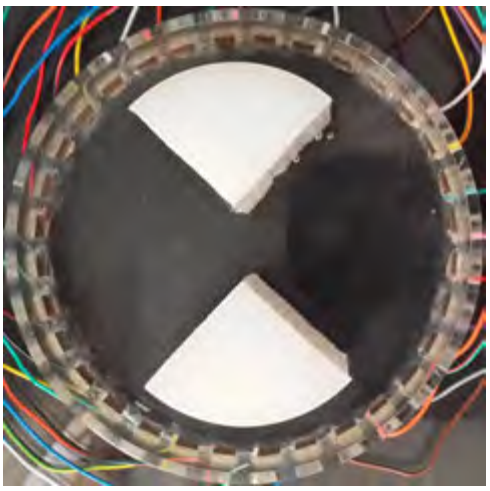

(a) Image of two blocks of polytetrafluoroethylene (teflon) placed at 12 and 6 O'clock

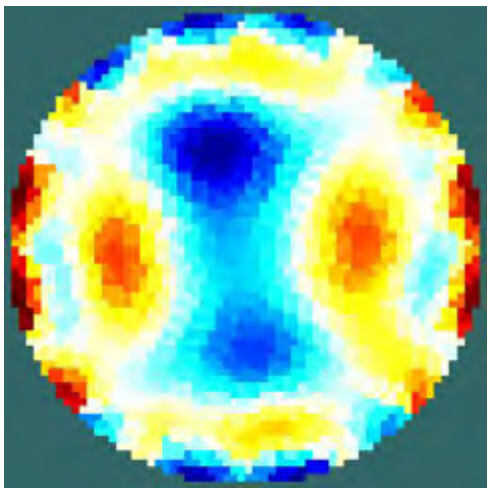

(b) Reconstructed image using impulse responses

Figure 6.7: Images of real objects (left images) placed at selected locations, and their reconstructed images (right images) using CDM EIT.

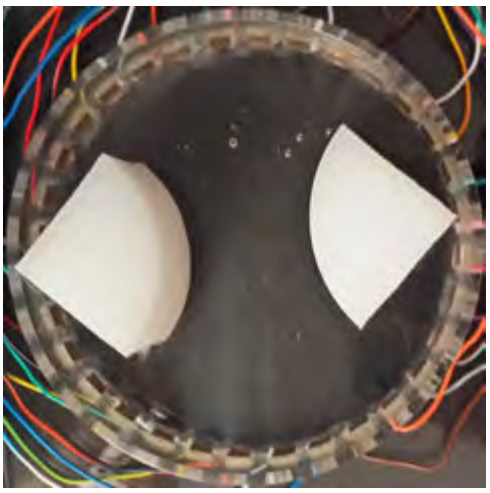

(a) Image of two blocks of polytetrafluoroethylene (teflon) placed at 9 and 3 O'clock

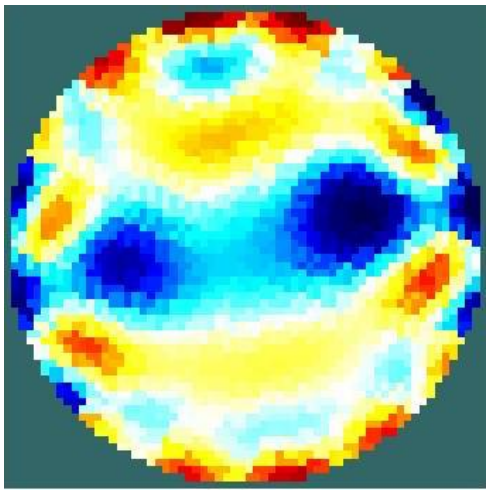

(b) Reconstructed image using impulse responses

Figure 6.8: Images of real objects (left images) placed at selected locations, and their reconstructed images (right images) using CDM EIT.

The reconstructed images show that CDM can produce comparable images to the currently used EIT modalities FDM and TDM. This is seen in the correct localization of the inhomogeneities and their relative sizes. The quality of the reconstructed images depends heavily on the concentration of the saline solution. This is because the concentration is

related to the solution's impedance. The difference in impedance between the the solution and the introduced object also contributes. Furthermore, due to the chosen current injection protocol, the current distribution in the phantom is symmetric about the ground electrode, and the device has more sensitivity close to the ground electrode as a result of the high current density in its vicinity. Figure 6.9, shows the current distribution within the device. Reconstructed images obtained here are compared to similar ones reported in [7; 95]. The linearization done in the FEM and reconstruction algorithms can adversely affect the accuracy of reconstruction in cases where the imaged object has large impedance difference from the surrounding saline solution. While it is to be assumed that a reduction in the spectral contamination due to non-ideal correlation properties of Gold codes injected simultaneously into the phantom will improve the results, the results show comparable quality to those reported in literature in the current state of the system. The results of Figures 6.7 and 6.8 further show that the designed device can distinguish between two objects within the phantom.

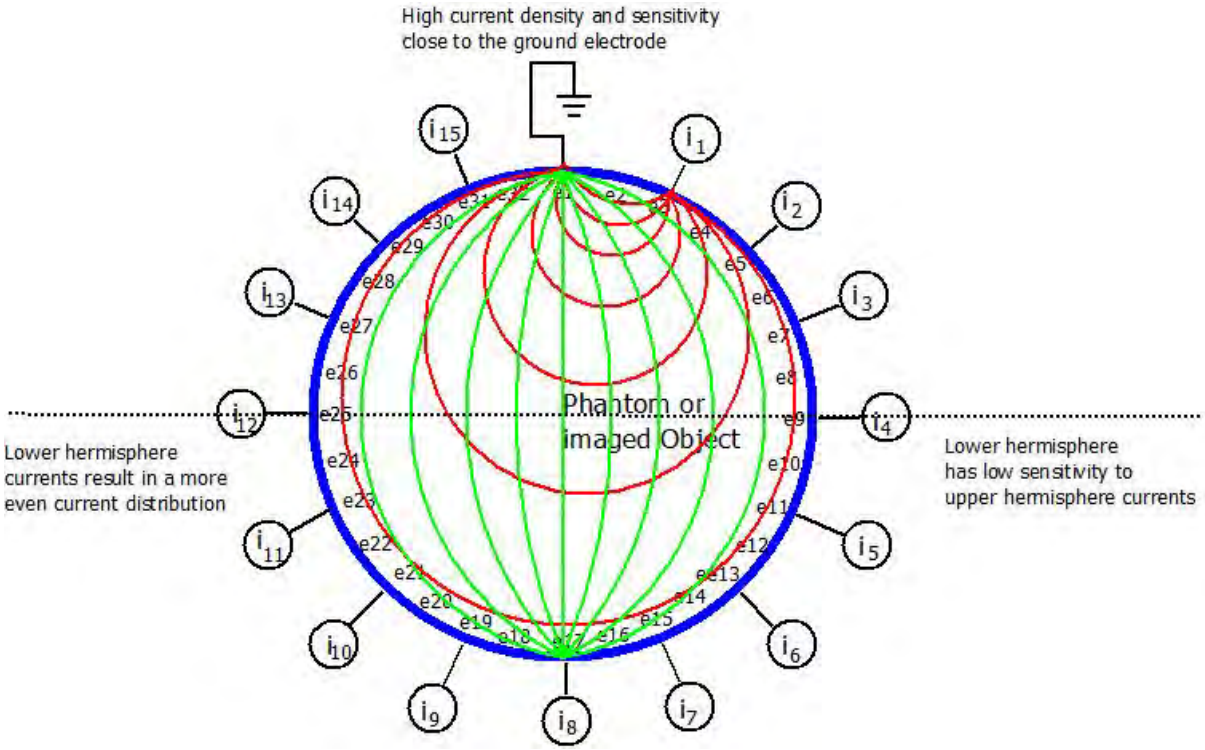

Figure 6.9: Image showing the current distribution within the phantom. It shows that the current density is highest in the vicinity of the ground electrode and falls off evenly away from that electrode.

6.3 Comparison of 256 and 1024 Gold Codes

In this research work, the selection of Gold code lengths used was taken as a compromise between achieving high frame rates (short codes) and two conflicting objectives: injection of high signal energies and getting good correlation properties, both of which get better with longer codes. The bowl was filled with a *normal* NaCl saline solution - (1%) concentration, which is similar to to the NaCl concentration in the human body electrolyte. Data sets of similar inhomogeneity locations are captured using 256 *chip* length codes and 1024*chips* ones. The results presented in Figures 6.10, 6.11, 6.12, show the different imaging quality using different code lengths. It can be seen from the figures that using shorter codes result in lower position and size accuracy in reconstructed images than longer codes. The results of reconstruction using 512 *chip* Gold codes are presented in Figure 6.13. In the results, the quality of reconstruction does not deteriorate heavily for the 512 *chip* codes.

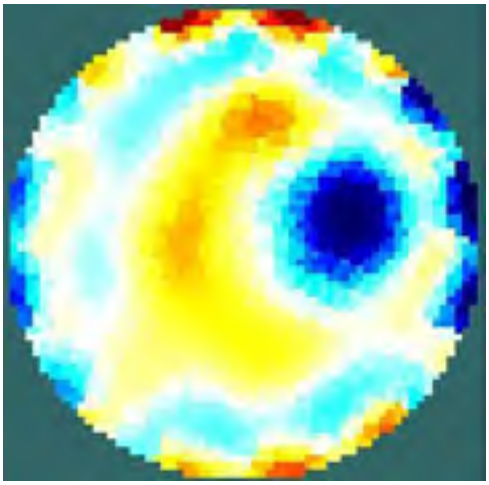

(a) Reconstructed banana object placed at 3'O'clock using 1024 *chips* codes

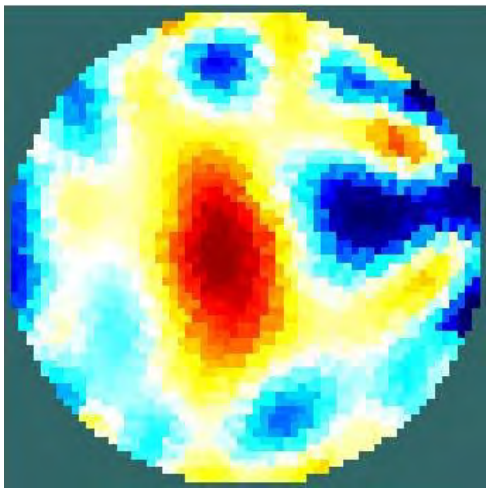

(b) Reconstructed banana placed at 3 O'clock using 256 *chips* codes

Figure 6.10: Reconstructed images of a a banana object placed at selected locations, using different code lengths. The shorter codes show lower reconstruction accuracy in position and size of objects.

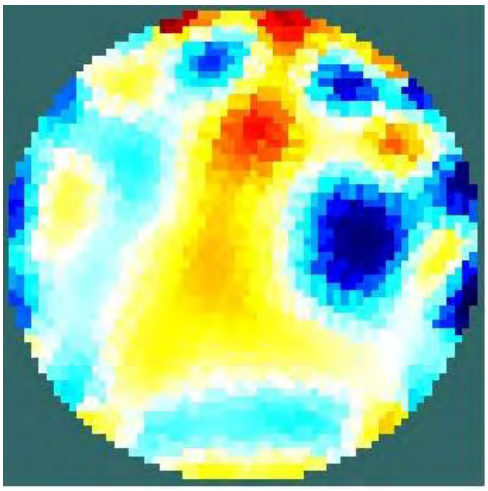

(a) Reconstructed cucumber object placed at 3'O'clock using 1024 *chips* codes

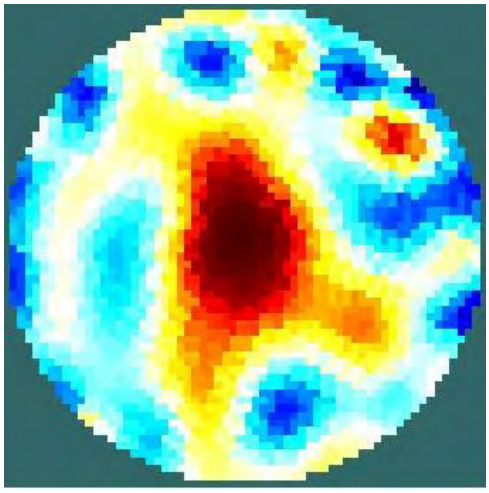

(b) Reconstructed cucumber placed at 3 O'clock using 256 codes

Figure 6.11: Reconstructed images of a a cucumber object placed at selected locations, using different code lengths. The shorter codes show lower reconstruction accuracy in position and size of objects.

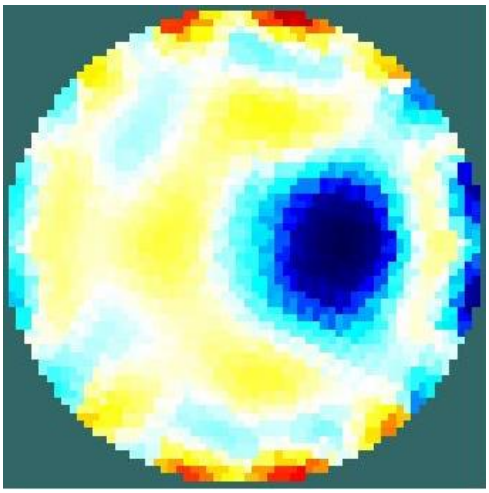

(a) Reconstructed teflon placed at 3 O'clock using 1024 *chips* codes

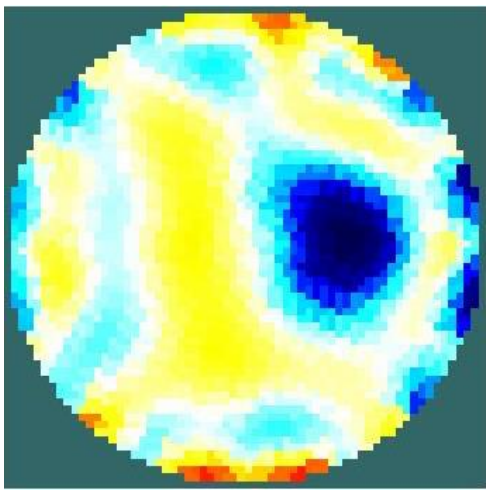

(b) Reconstructed teflon placed at 3 O'clock using 256 *chips* codes

Figure 6.12: Reconstructed images of a a teflon object placed at selected locations, using different code lengths. The shorter codes show lower reconstruction accuracy in position and size of objects.

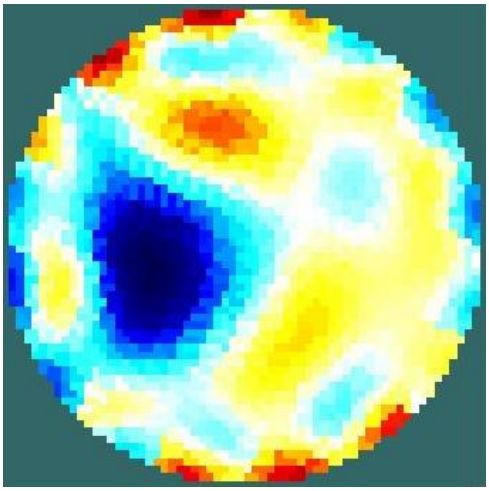

(a) Reconstructed teflon placed at 9 O'clock using 1024 *chips* codes

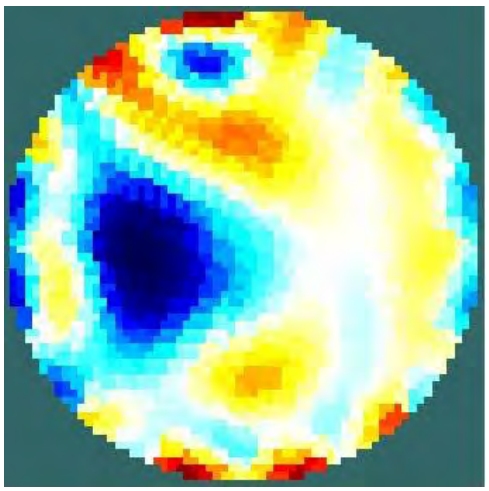

(b) Reconstructed teflon placed at 9 O'clock using 512 *chips* codes

Figure 6.13: Reconstructed images of a a teflon object placed at selected locations, using different code lengths. The shorter codes show lower reconstruction accuracy in position and size of objects.

It was decided based on the evidence of these results that codes of length 1024 *chips* would be used for the rest of the study. However, codes of 512 *chips* were also tested and can be used, at the sacrifice of reconstruction accuracy, and twice the imaging speed (frame rate). Miao and Zane used multiple *epochs* of pseudo-random binary codes, and averaged the results to improve the spectral quality identified impulse response of a power converter in [103], while this approach may work, in the case of multiple code injections, it also has the disadvantage of lowering the attainable frame rates.

6.4 CDM Frequency Difference EIT

In addition to the experiments performed to test the use of CDM in EIT, it is also a stipulation of the hypothesis that a single data set of CDM EIT can be used to reconstruct the impedance distribution using frequency difference imaging. This has the advantage of reducing the temporal resolution of the EIT device to half (twice the speed). However, this mode of difference imaging depends heavily on the variation of the impedance of the imaged object with frequency. McEwan and colleagues have established using a 0.1% saline solution that the impedance of a banana becomes the same as that of the salt solution around 90 kHz making it indistinguishable through time difference imaging at that frequency [7]. Yerworth and colleagues support the findings of McEwan and further

show through Cole-Cole plots of direct measurement that there is enough impedance variation between 2 kHz and 8 kHz, as well as between 8 kHz and 1.6 MHz for a piece of banana or cucumber to enable the use of frequency difference imaging. They however attribute the lack of distinguishability of the imaged banana at 90 kHz to the CMMR of the system. It was therefore decided that while their findings using EITS suggested very little change in these frequency ranges, a banana would be a suitable object to test the frequency difference imaging capabilities of the designed simultaneous injection CDM system in the frequency range 0 - 8 kHz. The results presented in Figure 6.14, show that while the achieved imaging quality and sensitivity is not good we can successfully implement frequency difference imaging. The subtracted data sets were sampled at frequencies 100 Hz and 8 kHz.

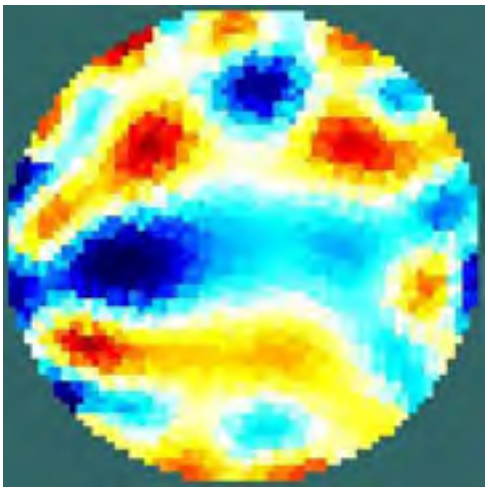

(a) Reconstructed images of banana placed at 9 O'clock using frequency difference imaging.

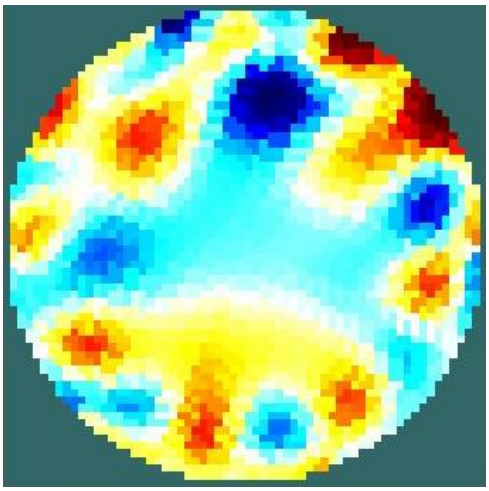

(b) Reconstructed images of banana placed at 12 O'clock using frequency difference imaging.

Figure 6.14: Images of a banana imaged using frequency difference imaging.

6.5 Conclusions

System test results are presented showing that the integrity of injected current patterns is acceptable and that the measured voltages are distinguishable. Results of reconstruction show that CDM can be used in EIT to image single objects placed at selected locations withing a phantom and to image two objects placed in the phantom. Results of frequency difference imaging are presented showing that the imaging is successful. However, due to the limited bandwidth of the prototype system the image quality is low compared to that of time difference imaging. Analysis of the results is presented in the next chapter.

Chapter 7

Results Analysis and Discussion

Analysis of the results presented in the previous chapter is performed here in order to measure the success of the prototype system developed in affirming the hypothesis of this dissertation. The analysis conducted uses the performance measures discussed in Chapter 3, in order to quantitatively and qualitatively measure the performance of the system. The chapter is divided into three sections as follows: the first section addresses the performance of the prototype system by analyzing the signals through the system, while the second section analyses the entire system through the results of imaging. These sections use both the qualitative and quantitative performance measures to draw comparisons of the designed prototype with prominent reported works that use TDM and FDM. Explanations of the results are given, challenges facing the developed system are identified and possible approaches to address such challenges discussed. Due to the lack of standardized presentation of tomography systems and their performance in literature, the task of comparing systems is not a trivial one and the author infers some performance measures of reported systems from presented results. Such a process is subject to some error as the author has no access to the raw data from such literary sources for accurate processing.

7.1 System Performance

The prototype system designed was intended as a platform for checking that pseudo-random binary codes injected simultaneously into a 16 electrode tomography system will confirm the research hypothesis. The system is therefore limited by budget constraints to being a basic system that meets bare minimum specifications given in the design

chapter. Analysis of performance of the system is however performed and compared to other reported systems, however unfair the comparison might be. In cases where direct comparisons can not be drawn, extrapolation and hypothetical analysis based on the features of compared systems is performed.

7.1.1 Accuracy/Systematic Error

Out of the reviewed literary sources, the work of McEwan [7] is one of those that present direct measurements of conductance of a banana object for comparison with the values obtained EITS over a frequency range of up to 1 MHz. In their report they show that the Sheffield Mark 3.5 system they used can accurately predict the conductivity spectrum of a banana object up to a maximum frequency of 128 kHz. It is also evident in their work that the system is unable to detect a conductance change of 0.025 S/m (using time multiplexed Gold codes) and 0.04 S/m (using time multiplexed sinusoidal inputs) for a banana occupying 10% of the phantom at 128 kHz with reference to the conductance of the background saline solution of conductance 0.16%.

Based on the direct measurements of McEwan, the KHU Mark 1 system reported by Woo [10] can be benchmarked for measuring the conductivity spectrum of a banana object producing a 50% error at a frequency 10 kHz. However, the results presented show that the KHU system is able to detect a conductance change of 0.01 S/m introduced by the banana object at 10 kHz in a saline solution of conductivity: 0.01 S/m, which is more sensitive than the Sheffield system. Direct impedances of a banana and cucumber objects are made in the report by Yerworth [95]. and show a errors of 1288% and 4830% respectively. Based on these results it is seen that the accuracy of EITS systems in directly determining actual values is not very good. This can be rectified by calibration experiments using known impedances. Regardless of the errors in the determination of absolute admittivity values, the reconstructed images still give invaluable information on the constitution of the imaged objects. It was decided that this performance measure not be assessed, as even direct conductivity measurements of McEwan [7] and Woo [10], show errors which make it difficult to use in benchmarking EIT systems.

7.1.2 Noise Error/SNR, DC Offset and Low Frequency Drift

The results presented in this section are derived from the measurement signals. In Figure 7.2, it is uncovered that the measurement system has DC offsets on the 16 measurement

channels with a maximum offset of 0.13 V and a maximum standard deviation on the channels of 0.01 V which is 10% of the minimum expected variation caused by an impedance change of 100 Ω using excitation currents of 1 mA peak amplitude. An estimation of the measurement NER is then 0.1, which drops to 0.001 at 10 $k\Omega$.

Furthermore, the results in Figure 7.1 show that there is no low frequency drift in the system across the acquisition of about seven imaging frames. The removal of the DC bias is done in software to reduce reconstruction errors. A method to reduce the effects of measurement noise and offsets is to average the results over multiple frames, and use averaging on homogeneous measurements used in time difference imaging. This approach however decreases the effective frame rates of the system and is not preferable. Wilkinson and colleagues [4] reported measurement standard deviations of 0.0025 V. They however computed the percentile over the largest measurement which is counter intuitive as measurement variation affects smallest values more. A low pass filter can be implemented to alleviate the measurement noise in the system.

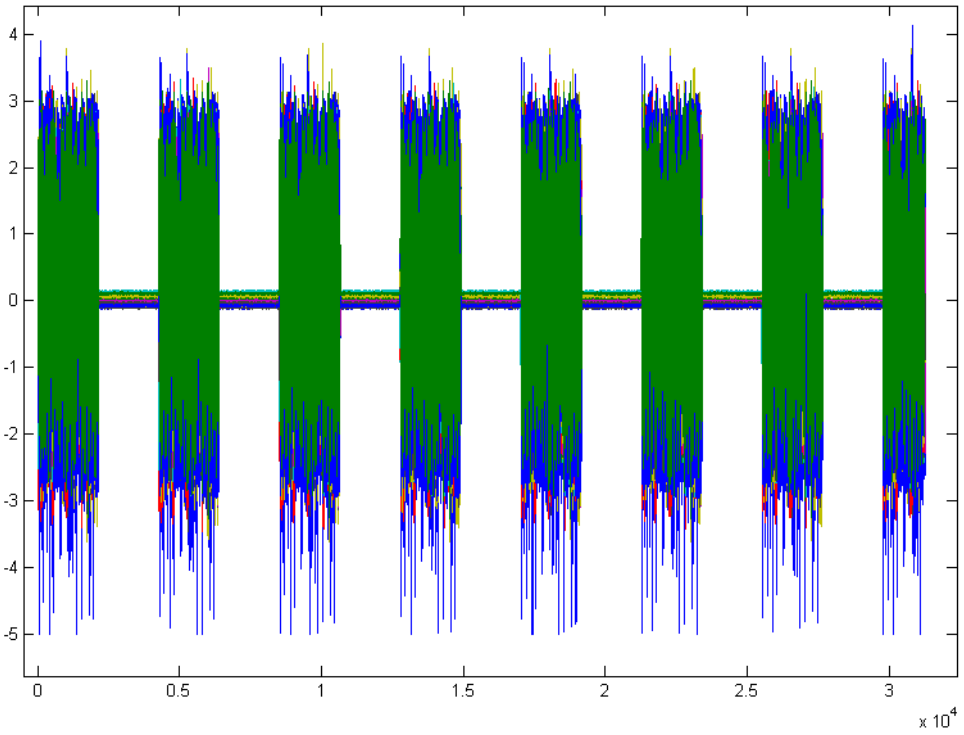

Figure 7.1: Frames of the data (in Volts vs sample number) capture using 1024 *chip* Gold codes, showing that the zero input measurement between frames has no low frequency drift. Furthermore, it is seen that the zero input measurements contain noise and DC offset.

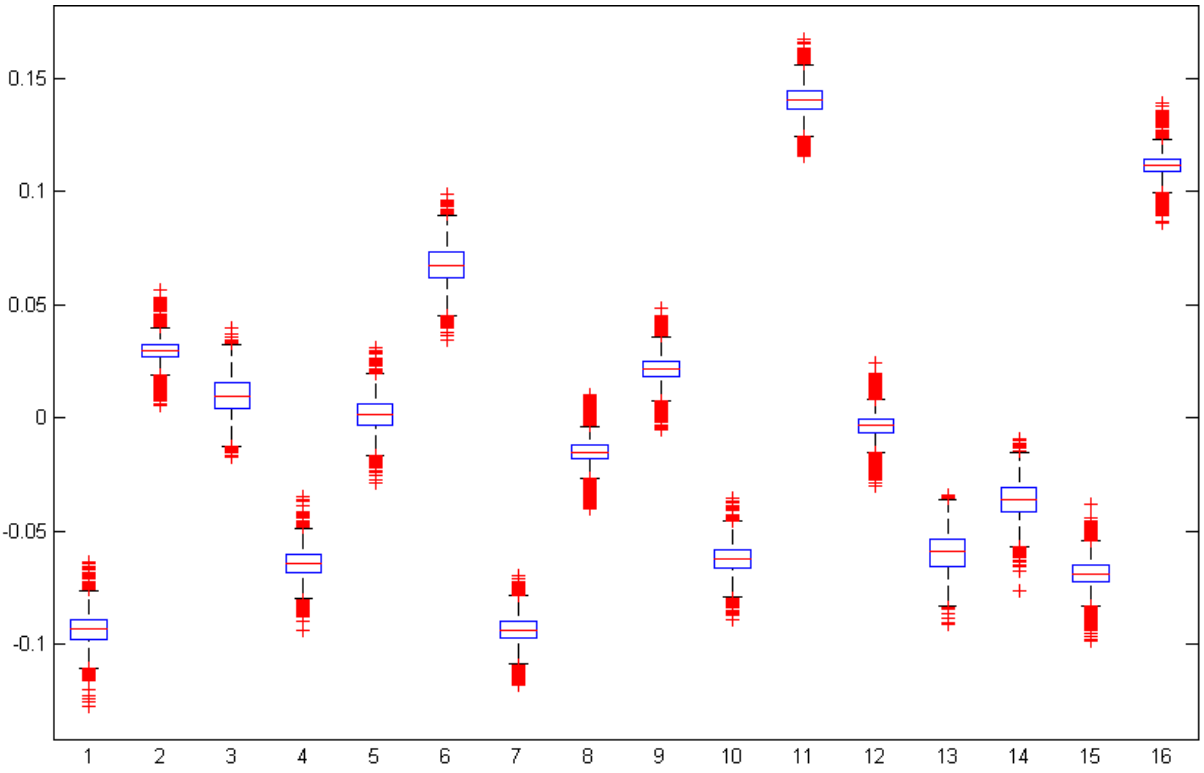

Figure 7.2: Box-Whisker plot of measurement noise across all 16 measurement electrodes (in Volts vs electrode number). Results show DC offset in all the channels and give the mean and variance of the noise. This data is used to set regularizing constants in the reconstruction.

7.2 Reconstruction Performance

The reconstruction done in this work used the Gauss-Newton one step solver. Comparison done between this algorithm, the Sheffield back-projection and GREIT algorithms showed that it has higher performance measured by ringing, amplitude response, and position error. However, the comparisons also showed that the algorithm is less robust than the other two to noise [22].

7.2.1 Analysis

In this subsection analysis of the presented phantom results is performed. The analysis is performed on reconstruction tests using banana objects, however the analysis can be

replicated for other objects types. The analysis proceeds in a similar manner to that done for simulation results and the process will not be presented here in its entirety again. However, additional coverage will be given for the analysis of frequency difference imaging and distinguishability performance of the system.

The results summarized in the Table 7.1, are extracted from Figures 7.4, 7.5, 7.6, 7.7. The magnitude plots shown are used to estimate the diameter of the phantom (two outer data points), the two interior data points are used to estimate the diameter of the reconstructed object, then all points are used to estimate the centroid of the object. All the experiments in this section were performed using a banana placed at selected locations in a saline solution. The diameter of the banana was 36% of the phantom diameter. The banana centroid locations around the phantom were at fixed at 0.4 radius fraction from the phantom center. Illustrative images are given in Figure 7.3.

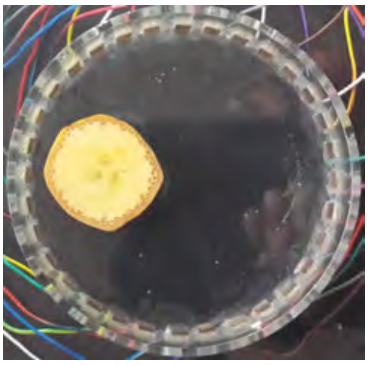

(a) Image of real banana object placed at 9'O'clock in the phantom

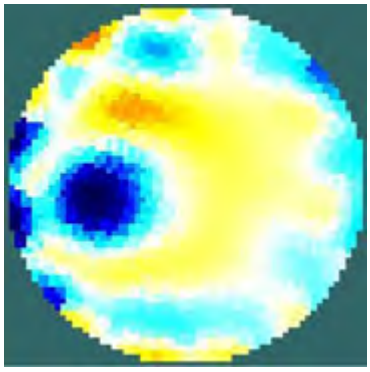

(b) Reconstructed image using impulse responses

Figure 7.3: Reconstructed images of inhomogeneities (left images) placed at selected locations, and their reconstructed images (right images) using CDM EIT.

Table 7.1: Performance indices of CDM EIT banana phantom tests.

Index	**3 0'clock**	**6 O'clock**	**9 O'clock**	**12 O'clock**	**Center**	**Average**
PE	5.2%	3.6%	1%	4.1%	-	3.5%
SE	9.6%	4.3%	2.9%	8%	-	6.2%
NER	27.3%	31.9%	34.1%	32%	-	31.3%
D	14%	13.3%	12.7%	14.7%	-	13.7%

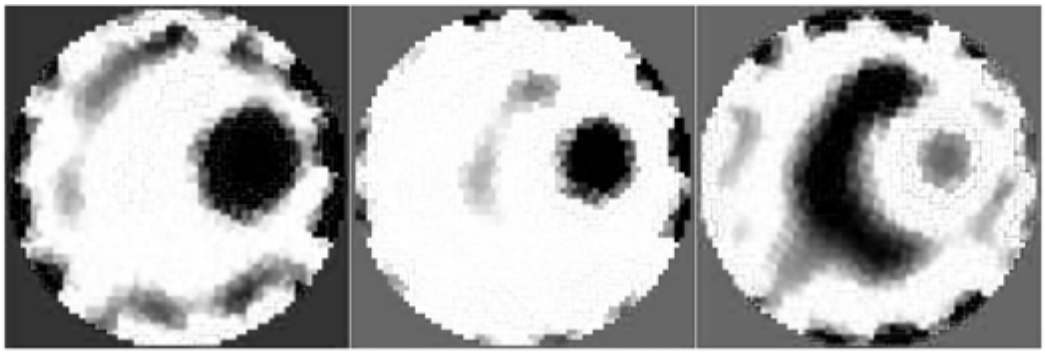

(a) Gray scaled Red, Green and Blue (RGB) planes of the reconstructed image, from left to right. The Green plane shows the reconstructed object, while the Blue Plane shows the ringing and image artifacts.

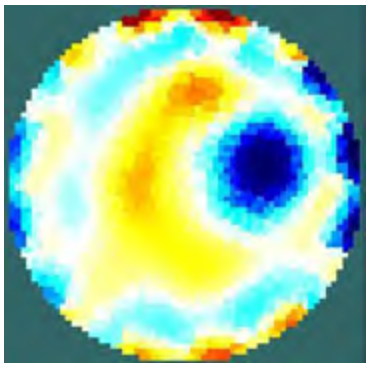

(b) Reconstructed image using impulse responses of CDM EITS, for comparison

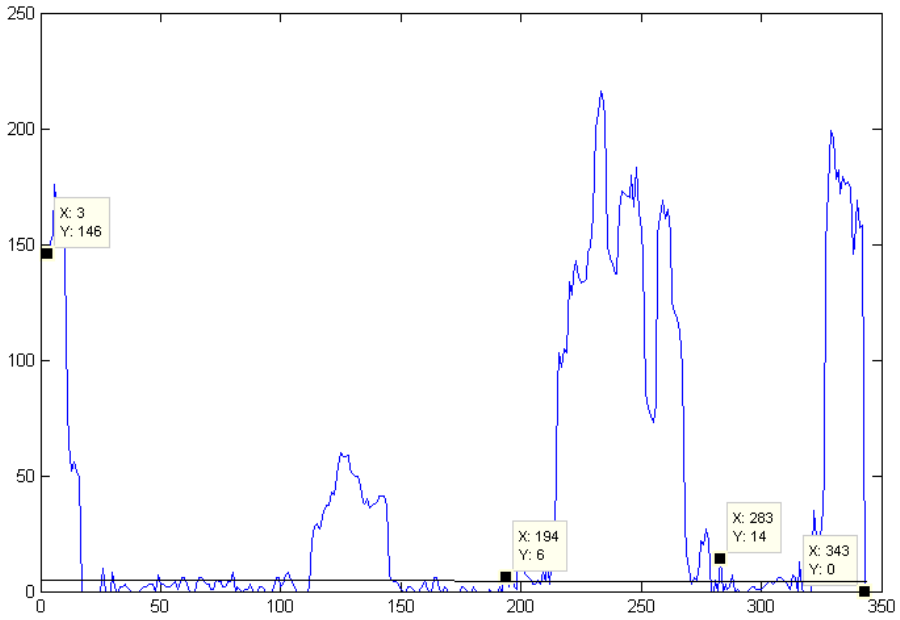

(c) Pixel magnitude plot along the middle horizontal line, plotted against pixel number.

Figure 7.4: Processing of reconstructed image at 3 O'clock to extract size, location, and centroid.

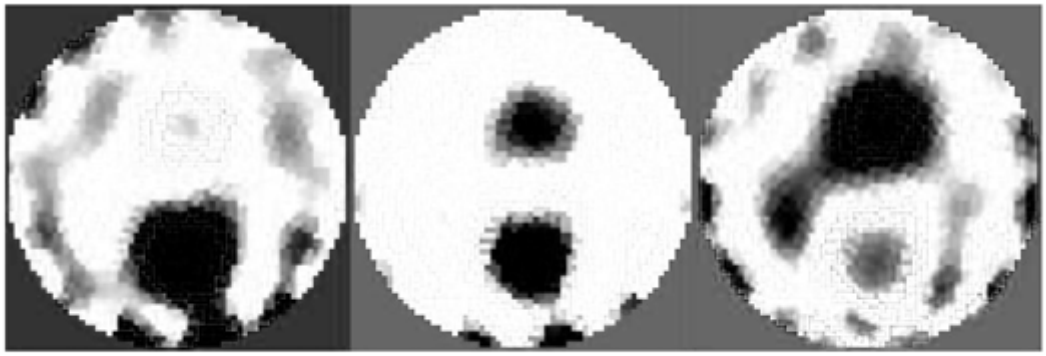

(a) Gray scaled Red, Green and Blue (RGB) planes of the reconstructed image, from left to right. The Green plane shows the reconstructed object, while the Blue Plane shows the ringing and image artifacts.

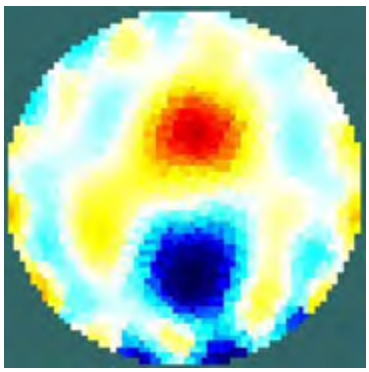

(b) Reconstructed image using impulse responses of CDM EITS, for comparison

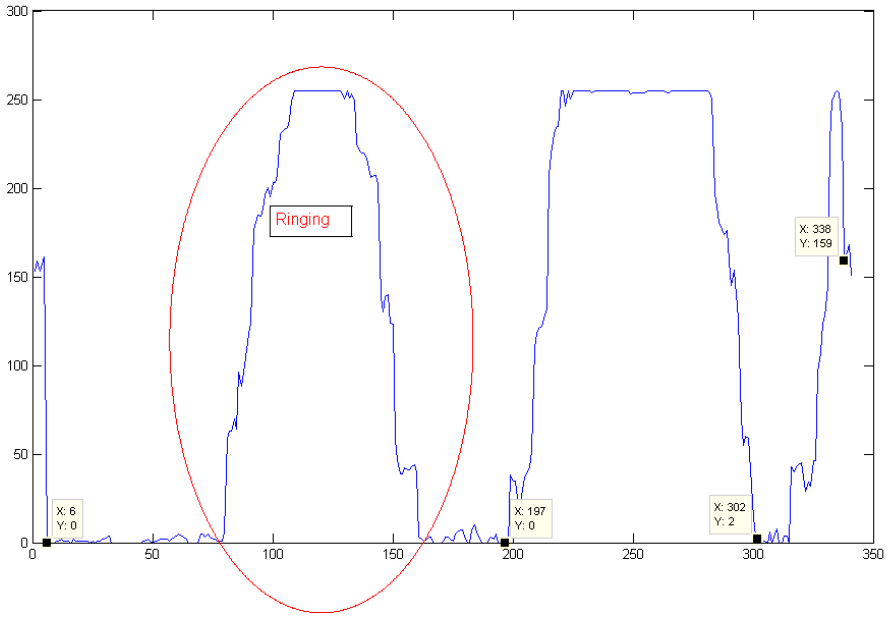

(c) Pixel magnitude plot along the middle vertical line, plotted against pixel number.

Figure 7.5: Processing of reconstructed image at 6 O'clock to extract size, location, and centroid.

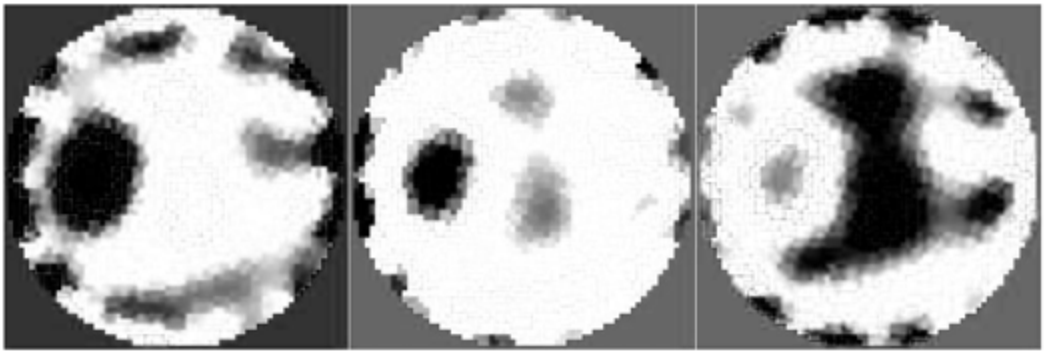

(a) Gray scaled Red, Green and Blue (RGB) planes of the reconstructed image, from left to right. The Green plane shows the reconstructed object, while the Blue Plane shows the ringing and image artifacts.

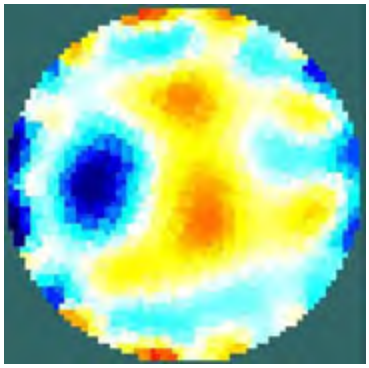

(b) Reconstructed image using impulse responses of CDM EITS, for comparison

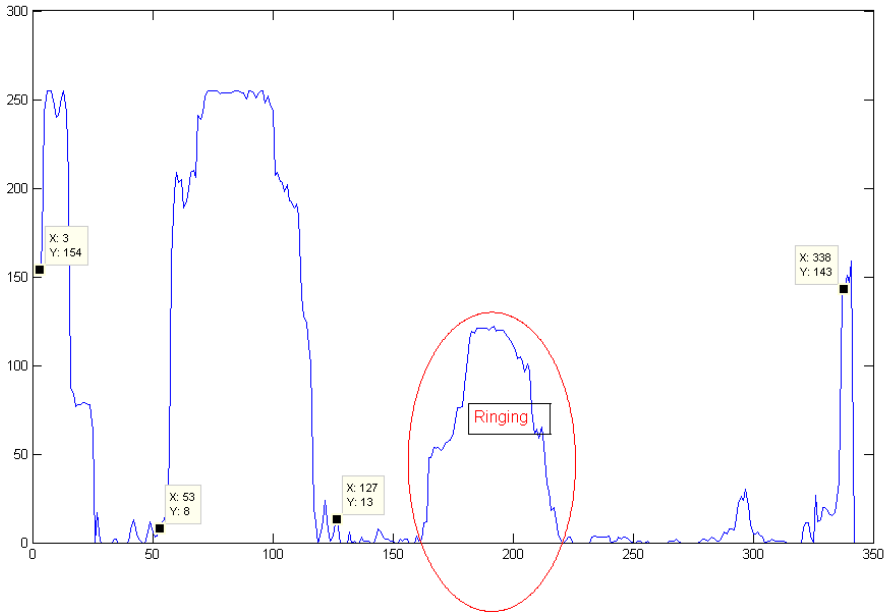

(c) Pixel magnitude plot along the middle horizontal line, plotted against pixel number.

Figure 7.6: Processing of reconstructed image at 9 O'clock to extract size, location, and centroid.

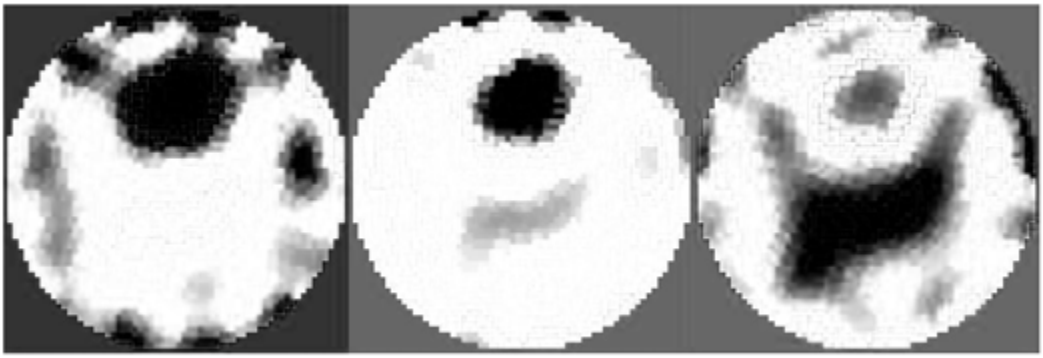

(a) Gray scaled Red, Green and Blue (RGB) planes of the reconstructed image, from left to right. The Green plane shows the reconstructed object, while the Blue Plane shows the ringing and image artifacts.

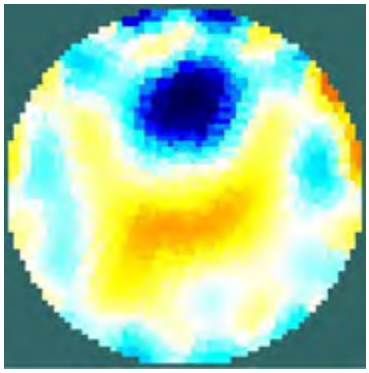

(b) Reconstructed image using impulse responses of CDM EITS, for comparison

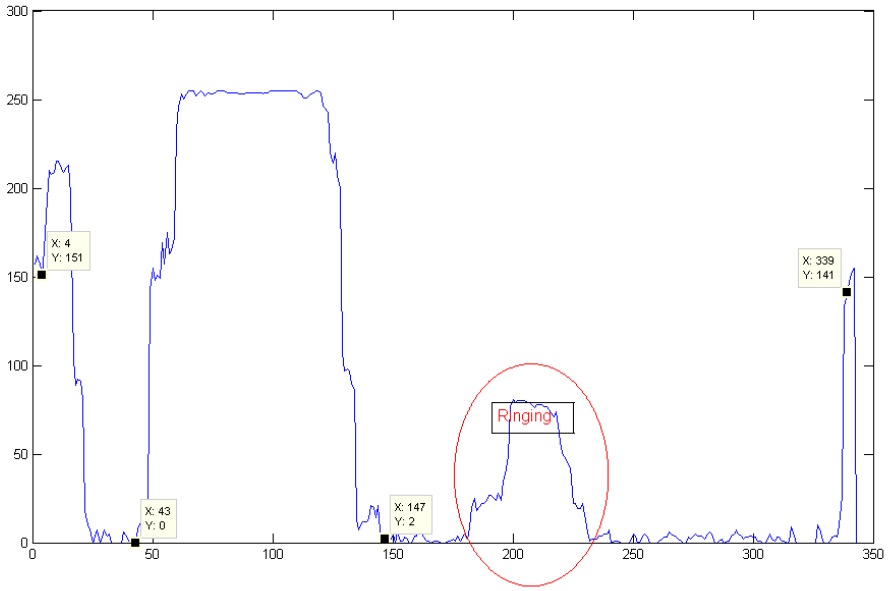

(c) Pixel magnitude plot along the middle vertical line, plotted against pixel number.

Figure 7.7: Processing of reconstructed image at 12 O'clock to extract size, location, and centroid.

7.2.2 Position Error

The reconstructed images using banana objects placed at different locations within the phantom show an average localization error of 3.5%. The position error is measured as the ratio of the difference in radial distances of the actual and reconstructed objects, with the radial distance of the actual object from either the center or edge of the phantom.

These results are comparable to reported results of Nahvi [26], estimated at 43% location error, and 25% position error estimated from the results of Yerworth in [95]. Similar construction estimations on the results McEwan [7] show a position error of 12% using pairs of Gold codes time multiplexed around all the electrodes of the Sheffield Mark 3.5. Other results are presented in [94] comparing the KHU Mark 1 and the UCH Mark 2.5 using different protocols. The results show maximum position errors of 16.9% and 10.7% for the KHU and UCH systems measured from the phantom center. Unfortunately there is not enough information in the report of a TDM ERT system by Wilkinson and colleagues [4] and the FDM system by Granot [5] to draw any meaningful comparisons.

7.2.3 Size Error

The error in the reconstructed size is measured as the ratio of the reconstructed and actual object radii with the radius of the actual object. In most cases the reconstructed images appear dilated compared to the actual objects. In order to do this in an accurate manner, a threshold is selected in the image node (pixel) values at which the object boundary is drawn - a similar process to image segmentation. The results of the designed prototype show a 12% dilation in the reconstructed images. A comparison is done with the results of a TDM ERT system of Wilkinson [4] estimated at 9.2% computed from an actual percentage occupancy of 14.3% and reconstructed occupancy of 23.5% estimated from the presented images. The results of McEwan [7] reconstruct an object of occupancy 10% producing an image of occupancy 30% and a dilation of 200% or 20% size error. The results of Nahvi show 35% dilation in the banana size. However, these results maybe affected by the fact that two objects are in the phantom. An FDM system reported by Granot [5] shows a dilation of 32% for an object placed at the center of the phantom. When the object is moved to the vicinity of the single current sinking ground electrode the dilation becomes 64%. These values are computed from the stated actual occupancy of 31% and the reconstructed images reported. Based on these comparisons, and the attained size error of 6.2% it is clear that the designed prototype performs comparable to the these reported systems.

7.2.4 Detectability and Ringing

The results presented in the previous chapter Figures 7.3, 6.5, 6.6 show that the developed prototype is able to detect object placed around the phantom. However, the the image quality at different locations of the phantom is not the same. This is due to the uneven current density distribution within the phantom as a result of the chosen current injection protocol. A measure of detectability as an aggregate of the position and size errors is computed to be at an average of 13.7%. It is however noticed that compared to the simulation results, the NER ratio from the system is higher with an average of 31.3% and this is attributed to the measurement noise and DC offset discussed earlier, and the fact that the Gauss-Newton one step reconstruction algorithm used has been established to introduce ringing as seen in the results presented in Figures 7.4 to 7.7. Filtering can be used to alleviate the effects of measurement noise, and an alternative reconstruction algorithm such as the Sheffield back-projection or Newton-Raphson can also be used.

7.2.5 Distinguishability

Through the use of two teflon objects placed within the phantom, it is evident from Figures 6.7 and 6.8 that the system can distinguish among multiple objects. However, there is evidence of shape deformation for both objects and some position error. The results obtained are comparable to those obtained by [26], with a size error of 35%. For this performance measure the reviewed TDM and FDM systems of Wilkinson and Granot [4; 5] do not provide any information regarding the imaging of more than one object in the phantom. This is also the case for the report of McEwan and colleagues [7]. Furthermore, the resultant current distribution within the phantom, from the injection protocol also introduces uneven reconstruction quality. This protocol was chosen because it results in a lower number of electrodes compared to floating current injection. It was also chosen because the proposed use of the same electrodes for current injection and voltage measurement in [23], did not yield satisfactory results in this work.

7.2.6 Frame Rates

Comparisons of tomography systems on the basis of their frame rates heavily depends on their hardware capabilities which are directly related to their cost, and does not constitute a fair comparison metric. However, capabilities of different multiplexing schemes can

be compared, assuming equal capabilities of data acquisition hardware. In this regard and assuming that all systems are required to perform frequency difference imaging and spectroscopy, over the same frequency range, the comparison boils down to the length of injected current patterns. It is reported in [26] that *chirp* signals of period 5 ms were used with a bandwidth of 210 kHz. This input requires time difference multiplexing to distinguish among different input electrode effects. On a 16 electrode system this can only achieve 12 frames/s. Working from the sampling requirements of a signal of 210 kHz at 410 kHz and measuring 13 channels plus the injected signal itself, this would require a 5.88 MHz multiplexed input device. The same input device used for a CDM system with 16 effective electrodes using simultaneous injection and measurement, can only provide an imaging bandwidth of 91.9 kHz at 84 frames/s when using 1024 *chip* codes and 168 frames/s if 512 *chip* codes. This is because using CDM requires all codes to be measured as opposed to measuring only one *chirp* signal. It therefore becomes apparent that simultaneous injection CDM EITS is only an advantage when the imaged object changes rapidly as a function of time, but does not require a wide-band frequency difference imaging system. In any other condition, it is preferable to use a time difference multiplexed system employing either a *chirp* or maximum length pseudo-random binary code as an input in a manner that was done in [26; 7], in order to achieve moderate temporal resolution at a wider bandwidth.

7.3 Frequency Difference Imaging

The results of frequency difference imaging performed using the prototype device are also analyzed in Figure 7.8. The limited frequency range of the designed device in the range 0 Hz to 15 kHz has greatly limited the attained results. This is because the impedance change of a banana in this range is quite small as reported in [7] and [10]. The results however, show that frequency difference imaging is possible. The required increase in frequency range was limited by budgets constraints is left for a full system design as a continuation of the research work presented here. From the results a NER of 30.4% is computed, size error of 11.5% and position error of 4.9%. The results further show that there is significant ringing and reconstruction artifacts in the reconstructed image.

(a) Gray scaled Red, Green and Blue (RGB) planes of the reconstructed image, from left to right. The Green plane shows the reconstructed object, while the Blue Plane shows the ringing and image artifacts.

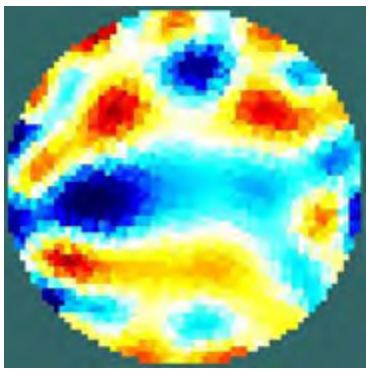

(b) Reconstructed image using frequency difference imaging, for comparison

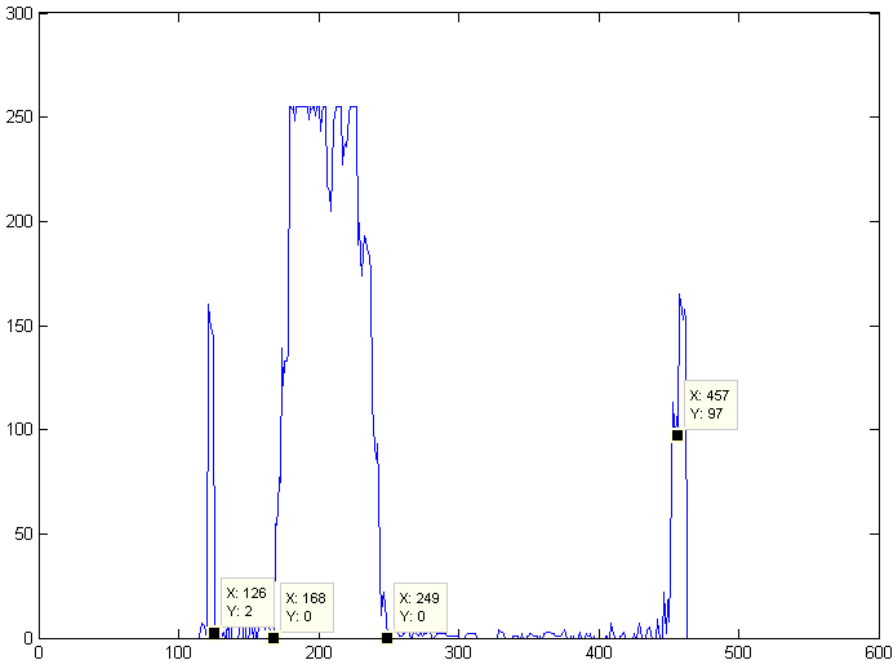

(c) Pixel magnitude plot along the middle horizontal line, plotted against pixel number.

Figure 7.8: Processing of reconstructed image at 3 O'clock to extract size, location, and centroid.

7.4 Conclusions

While the research community in EITS has not fully accepted and used the measures of performance that allow comparison between different reported works, an effort is made in this chapter to quantify the performance of the designed prototype system. The results are as follows: position error 3.5%, size error of 6.2%, detectability error of 13.7% and 31.3% noise error ratio, using time difference imaging. Frequency difference imaging results give: a noise error ratio of 30.4%, position error of 4.9% and size error of 11.5%. These results are comparable if not better that most results results reviewed from literature that use TDM and FDM. Test results on the hardware platform show DC offsets on the measurement channels. These can be removed in software. In addition, the measurement system shows a noise error ratio of 10% maximum over all 16 measurement channels. The results of the reconstruction confirm that pseudo-random binary codes can be successfully injected into a phantom to extract usable impulse response data for both time difference and frequency difference imaging in EITS. Given hardware with a wide enough frequency range and rigorous calibration, EITS systems can provide the capability of spectroscopy. However, this capability was not confirmed due to lack of accurate truth impedance measurements for banana or cucumber objects. Measurements done and reported in literature show very large errors indicating that more work still needs to be done in the instrumentation for measuring truth values of such impedances and calibration methods for EITS systems to achieve such accuracy.

Chapter 8

Conclusions, Recommendations and Future Research

Based on the research work conducted, and both simulation and experimental results presented in the previous chapters, the following conclusions are drawn in line with the different aspects of the research hypothesis. Thereafter, some recommendations for future work are given, that can improve both the quality of imaging in CDM EIS and increase the attainable temporal resolution (frame rates).

8.1 Conclusions

8.1.1 Hypothesis Confirmation

Using the designed platform, the hypothesis was confirmed, which stated that CDM EIT using simultaneous injection and measurement of currents and voltages respectively is practically possible. The obtained results of experimental testing showed an error of 3.5% in the position of the reconstructed objects and 6.2% error in size compared to the actual imaged object. These errors are lower than reported results in literature using other systems based on TDM and FDM. The overall detectability of imaged object was achieved with 13.7% error computed as an aggregate of the PE, SE and NER. It was however noted that, the non-ideal correlation properties of pseudo-random binary code limit the attainable quality of imaging. Furthermore, the implementation results in twice the number of electrodes needed for TDM, however, it has the potential for high frame

rates, using excitation signals that excite all frequencies in the attainable range with equal energy. Polynomial fit estimates were used to extract cleaner impulse response frequency data, and they introduce errors in measurements. Electrical impedance spectroscopy is possible and much easier using CDM EIT, as it only requires the use one data set to be measured compared to N measurements using TDM and a *chirp* excitation inputs where N is the total number of current injection electrodes.

8.1.2 Prototype CDM EITS System

A 32 electrode EITS system was successfully designed and tested. This system uses 16 electrodes for differential voltage measurement, 15 electrodes are used to inject Gold codes currents and 1 electrode used as a ground return path. The system is tested to have adequate accuracy and repeatability. However, this system is connected to and draws power from mains supply which is not recommended for biomedical applications. Secondly, due to cost limitations the system can only image at 14 frames/second using codes of length 1024 chips and 60 frames/second using Gold codes of length 256 chips. The maximum attainable frame rate is 462 frames per second, using 31 chip codes, which is the shortest set that can give 16 distinct codes. The available imaging frequencies are up to 15 kHz. This frequency range is adequate for some imaging applications but low for applications needing up to 1 MHz imaging frequencies. The cost of the designed system is less than $30000.00ZAR$ which is cheaper than commercial platforms that cost more than $400000.00ZAR$. The prototype system showed no low frequency drift in measurements. However, the zero input measurements exhibited DC offsets of $mean + standard\ deviation\ =\ 0.13 \pm 0.01$ V. The standard deviation is about 10% of the smallest expected voltage variation coming out of the measurement system.

8.1.3 Frequency Difference Imaging

Frequency difference imaging was achieved using a single measurement data set. The results obtained showed 11.5% and 4.9% errors in size and position respectively. However, the attained imaging shows imaging accuracy that needs improvement. This is due to several factors being: the limited imaging frequency range offered by the current designed hardware, polynomial fitting errors and the sensitivity, which is a function of the code length, injected currents and their injection protocol for even current density distribution. Due to the feasibility of both CDM EIT and its associated frequency difference imaging, it is possible to apply this system to take both static and dynamic images in situations

where reference images (data sets) are not available such as closed industrial systems and anatomical human imaging. The only requirement is that the contents of the imaged object have distinct frequency dependent impedances, over the frequency range of the imaging device.

8.2 Recommendations

- The use of parallel measurement channels can improve system accuracy as the problem of ghosting at high frequency sampling is a problem requiring unreasonably stringently low output impedances for analog electronics.
- Faster sampling for the voltage measurements will widen the range of frequencies that can be interrogated by the imaging towards the desired 1 MHz ranges for Biomedical applications.
- Patient isolation and protection using opto-coupling, and fast acting fuse circuit breakers will make the device safer for live subjects.
- The current device can be configured to perform a TDM EITS using pseudo-random binary codes, for even distribution of signal energy over all interrogated frequencies and attain a wider spectroscopic range of up to 500 kHz. While this will reduce the frame rates, it offers benefit for systems that are not very rapidly changing. This would be equivalent to applying a *chirp* excitation.
- The device should be tested for EITS on real industrial plants and Biomedical subjects.
- To improve spectral purity for the generated impulse responses in CDM EITS, several approaches can be investigated and these are: injecting multiple periods of the used codes and averaging the results, using longer codes, investigation of better polynomial fitting approaches, and obviously improvement of implemented instrumentation.

8.3 Further Work

Motivated by the success of the research work presented here, further work will be dine to improve both the results quality, system capabilities and explore applications as follows:

- A fully functional system will be designed to support a temporal resolution of more than 200 frames/s. Due to the ease of implementation, this system will be adapted in software to support all three multiplexing modes: CDM, FDM and TDM. The system will have hardware capabilities to support a wider operating bandwidth of up to 500 kHz for improved results on both frequency difference imaging and spectroscopy.

- Biomedical testing of the capabilities of CDM EITS will be explored. This will require the upgraded system to incorporate all biomedical safety and robustness standards discussed in chapter 5. The biomedical testing of the upgraded device will start with imaging, monitoring and spectroscopy of non-critical human organs such as muscle activity but ultimately end with the envisaged head imaging due to differing ethical considerations.

- Custom software that supports the popular reconstruction methods and includes neural networks methods will be developed in order to increase reconstruction speed and provide a more integrated software system.

- Better instrumentation, will be further investigated in two domains: (a) the use of better current sources due to limitations and challenges faced by the modified Howland sources, and (b) methods that enable simultaneous injection of currents and measurement of voltages on the same set of electrodes, in order to reduce the required electrode count.

- The current method will be extended and tested on a 3-dimensional system for more practical applications.

Bibliography

[1] J. Webster, *Electrical Impedance Tomography*, ser. Biomedical Engineering Series. Adam Hilger, 1990.

[2] G. Teague, "Mass Flow Measurements of Multi-Phase Mixtures by Means of % Tomographic Techniques," Ph.D. dissertation, 2001.

[3] R. H. Bayford, "Bioimpedance tomography (electrical impedance tomography)." *Annu Rev Biomed Eng*, vol. 8, pp. 63–91, 2006.

[4] A. Wilkinson, E. Randall, J. Cilliers, D. Durrett, T. Naidoo, and T. Long, "A 1000-measurement frames/second ERT data capture system with real-time visualization," *Sensors Journal, IEEE*, vol. 5, no. 2, pp. 300–307, April 2005.

[5] Y. Granot, A. Ivorra, and B. Rubinsky, "Frequency-Division Multiplexing for Electrical Impedance Tomography in Biomedical Applications." *Int. J. Biomedical Imaging*, vol. 2007, pp. 54 798:1–54 798:9, 2007.

[6] J. R. Smith, C. D. Salthouse, and N. Gershenfeld, "Code-division multiplexing of a sensor channel: a software implementation." *IEEE Journal on Selected Areas in Communications*, vol. 17, no. 4, pp. 725–731, 1999.

[7] A. McEwan, J. Tapson, A. van Schaik, and D. Holder, "Spread spectrum EIT by code division multiplexing," *Journal of Physics: Conference Series*, vol. 224, no. 1, p. 012143, 2010.

[8] F. Seoane, K. Lindecrantz, T. Olsson, I. Kjellmer, A. Flisberg, and R. Bagenholm, "Brain electrical impedance at various frequencies: the effect of hypoxia," in *Engineering in Medicine and Biology Society, 2004. IEMBS '04. 26th Annual International Conference of the IEEE*, vol. 1, Sept 2004, pp. 2322–2325.

[9] T. Kerner, K. Paulsen, A. Hartov, S. Soho, and S. P. Poplack, "Electrical impedance spectroscopy of the breast: clinical imaging results in 26 subjects," *Medical Imaging, IEEE Transactions on*, vol. 21, no. 6, pp. 638–645, June 2002.

[10] E. Woo, P. Hua, J. Webster, and W. Tompkins, "Finite-element method in electrical impedance tomography," *Medical and Biological Engineering and Computing*, vol. 32, no. 5, pp. 530–536.

[11] M. Gevers, P. Gebhardt, S. Westerdick, M. Vogt, and T. Musch, "Fast Electrical Impedance Tomography Based on Code-Division-Multiplexing Using Orthogonal Codes," *Instrumentation and Measurement, IEEE Transactions on*, vol. 64, no. 5, pp. 1188–1195, May 2015.

[12] W. Yang and L. Peng, "Image reconstruction algorithms for electrical capacitance tomography," *Measurement Science and Technology*, vol. 14, no. 2003, pp. R1–R13, 2003.

[13] A. Carpio and M. Rapun, "Hybrid topological derivative and gradient-based methods for electrical impedance tomography."

[14] W. R. B. Lionheart, "EIT reconstruction algorithms: pitfalls, challenges and recent developments," *Physiological Measurement*, vol. 25, no. 1, p. 125, 2004.

[15] E. Somersalo, M. Cheney, and D. Isaacson, "Existence and Uniqueness for Electrode Models for Electric Current Computed Tomography," *SIAM Journal on Applied Mathematics*, vol. 52, no. 4, pp. pp. 1023–1040, 1992.

[16] N. J. Avis and D. C. Barber, "Incorporating a priori information into the Sheffield filtered backprojection algorithm," *Physiological Measurement*, vol. 16, no. 3A, p. A111, 1995.

[17] M. Islam and M. Kiber, "Electrical Impedance Tomography imaging using Gauss-Newton algorithm," in *Informatics, Electronics Vision (ICIEV), 2014 International Conference on*, May 2014, pp. 1–4.

[18] C. Kotre, "STUDIES OF IMAGE RECONSTRUCTION METHODS FOR ELECTRICAL IMPEDANCE TOMOGRAPHY ," Ph.D. dissertation, University of Newcastle-upon-Tyne, 1993.

[19] D. A. Dean, T. Ramanathan, D. Machado, and R. Sundararajan, "Electrical Impedance Spectroscopy Study of Biological Tissues." *J Electrostat*, vol. 66, no. 3-4, pp. 165–177, Mar. 2008.

[20] A. Boyle and A. Adler, "The impact of electrode area, contact impedance and boundary shape on EIT images," *Physiological Measurement*, vol. 32, no. 7, p. 745, 2011.

[21] P. Vauhkonen, M. Vauhkonen, T. Savolainen, and J. Kaipio, "Three-dimensional electrical impedance tomography based on the complete electrode model," *Biomedical Engineering, IEEE Transactions on*, vol. 46, no. 9, pp. 1150–1160, Sept 1999.

[22] A. Adler, J. H. Arnold, R. Bayford, A. Borsic, B. Brown, P. Dixon, T. J. C. Faes, I. Frerichs, H. Gagnon, Y. Gärber, B. Grychtol, G. Hahn, W. R. B. Lionheart, A. Malik, R. P. Patterson, J. Stocks, A. Tizzard, N. Weiler, and G. K. Wolf, "GREIT: a unified approach to 2D linear EIT reconstruction of lung images." *Physiol Meas*, vol. 30, no. 6, pp. S35–55, Jun. 2009.

[23] A. McEwan, J. Tapson, A. van Schaik, and D. Holder, "Electrode Circuits for Frequency- and Code-Division Multiplexed Impedance Tomography," in *Biomedical Circuits and Systems Conference, 2007. BIOCAS 2007. IEEE*, Nov 2007, pp. 130–133.

[24] W. Yan, S. Hong, and R. Chaoshi, "Optimum design of electrode structure and parameters in electrical impedance tomography," *Physiological Measurement*, vol. 27, no. 3, p. 291, 2006.

[25] B. Packham, H. Koo, A. Romsauerova, S. Ahn, A. McEwan, S. C. Jun, and D. S. Holder, "Comparison of frequency difference reconstruction algorithms for the detection of acute stroke using EIT in a realistic head-shaped tank." *Physiol Meas*, vol. 33, no. 5, pp. 767–86, May 2012.

[26] M. Nahvi and B. S. Hoyle, "Wideband electrical impedance tomography," *Measurement Science and Technology*, vol. 19, no. 9, p. 094011, 2008.

[27] A. L. McEwan, J. Tapson, A. van Schaik, and D. S. Holder, "Code-Division-Multiplexed Electrical Impedance Tomography Spectroscopy." *IEEE Trans. Biomed. Circuits and Systems*, vol. 3, no. 5, pp. 332–338, 2009.

[28] M. Vauhkonen, W. R. B. Lionheart, L. M. Heikkinen, P. J. Vauhkonen, and J. P. Kaipio, "A MATLAB package for the EIDORS project to reconstruct two-dimensional EIT images," *Physiological Measurement*, vol. 22, no. 1, p. 107, 2001.

[29] M. Tsoeu and M. Inggs, "Electrical impedance tomography using code division multiplexing," in *AFRICON, 2015*, Sept 2015, pp. 1–5.

[30] ——, "Fully Parallel Electrical Impedance Tomography Using Code Division Multiplexing," *Biomedical Circuits and Systems, IEEE Transactions on*, vol. 10, no. 3, pp. 556–566, 2015.

[31] Z. Yu, A. Peyton, L. Xu, and M. Beck, "Electromagnetic inductance tomography (EMT): sensor, electronics and image reconstruction algorithm for a system with a rotatable parallel excitation field," *Science, Measurement and Technology, IEE Proceedings* -, vol. 145, no. 1, pp. 20–25, Jan 1998.

[32] W. Yang and S. Liu, "Electrical capacitance tomography with square sensor," *Electronics Letters*, vol. 35, no. 4, pp. 295–296, Feb 1999.

[33] Z. Yang, H. Pengfei, J. Shasha, and Z. Luying, "Quasi-orthogonal chirp signals design for multi-user CSS system," in *The 1st International Conference on Information Science and Engineering*, 2009, pp. 631–634.

[34] B. Sanchez, G. Vandersteen, R. Bragos, and J. Schoukens, "Basics of broadband impedance spectroscopy measurements using periodic excitations," *Measurement Science and Technology*, vol. 23, no. 2012, pp. 1–14, 2012.

[35] R. P. Patterson, "Electrical Impedance Tomography: Methods, History, and Applications (Institute of Physics Medical Physics Series)," *Physics in Medicine and Biology*, vol. 50, no. 10, p. 2427, 2005.

[36] B. R. Klein, *Introduction to medical electronics - for electronics and medical personnel*, 2nd ed. Robert. E Krieger Publishing Company, 1973.

[37] D. C. Barber and B. H. Brown, "Applied potential tomography," *Journal of Physics E: Scientific Instruments*, vol. 17, no. 9, p. 723, 1984.

[38] Y. Kim and H. W. Woo, "A prototype system and reconstruction algorithms for electrical impedance technique in medical body imaging," *Clinical Physics and Physiological Measurement*, vol. 8, no. 4A, p. 63, 1987.

[39] S. Gawad, T. Sun, N. G. Green, and H. Morgan, "Impedance spectroscopy using maximum length sequences: Application to single cell analysis," *Review of Scientific Instruments*, vol. 78, no. 5, pp. –, 2007.

[40] P. Bertermes-Filho, A. Felipe, and V. C. Vincence, "High accurate Howland current source: output constranints analysis," *Circuits and Systems*, vol. 4, pp. 451–458, 2013.

[41] P. Horowitz and W. Hill, *The Art of Electronics*. Cambridge University Press, 1989.

[42] A. S. Ross, G. J. Saulnier, J. C. Newell, and D. Isaacson, "Current source design for electrical impedance tomography," *Physiological Measurement*, vol. 24, no. 2, p. 509, 2003.

[43] Y. Granot and B. Rubinsky, "Frequency Marked Electrodes in Electrical Impedance Tomography," in *13th International Conference on Electrical Bioimpedance and the 8th Conference on Electrical Impedance Tomography*, ser. IFMBE Proceedings, H. Scharfetter and R. Merwa, Eds. Springer Berlin Heidelberg, vol. 17, pp. 380–383.

[44] J. C. Baeg, W. Hun, T. Oh, A. McEwan, and E. Woo, "An amplitude-to-time conversion technique suitable for multichannel data acquisition and bioimpedance imaging," *IEEE Trans Biomed Circuits Syst*, vol. 7, no. 3, pp. 349–354, 2013.

[45] P. Hua, E. Woo, J. Webster, and W. J. Tompkins, "Using compound electrodes in electrical impedance tomography," *Biomedical Engineering, IEEE Transactions on*, vol. 40, no. 1, pp. 29–34, Jan 1993.

[46] V. Kolehmainen, M. Vauhkonen, P. Karjalainen, and J. Kaipio, "Assessment of Errors in Static Electrical Ime pdance Tomography with Adjacent and Trigonometric Current Patterns," *Physiological Measurement*, vol. 18, no. 4, pp. 289–303, 1997.

[47] "eidors3d.sourceforge.net/tutorial/strange_effects/opposite_eas.shtml, [Accessed January 2014]."

[48] E. Woo and J. Seo, *Nonlinear Inverse Problems in Imaging*. John Wiley and Sons Ltd., 2013.

[49] D. J. Griffiths, *Introduction to Electrodymancs*. Prentice Hall, 1999.

[50] J. Walker, R. Resnick, and D. Halliday, *Fundamentals of Physics*, 2nd ed. John Wiley and Sons, 2011.

[51] C. Johnson, *Numerical solution of partial differential equations by the finite element method*. Dover Publications INC, 1987.

[52] S. Chapra and R. Canale, *Mumerical methods for engineers*, 6th ed. McGraw-Hill Co., 2010.

[53] J. Fish and T. Belytschko, *A first course in finite elements*. John Wiley and Sons Ltd., 2007.

[54] W. Bangerth, R. Hartmann, and G. Kanschat, "Deal.II&Mdash;A General-purpose Object-oriented Finite Element Library," *ACM Trans. Math. Softw.*, vol. 33, no. 4, Aug. 2007.

[55] G. Teague, J. Tapson, and Q. Smit, "Neural network reconstruction for tomography of a gravel-air-seawater mixture," *Measurement Science and Technology*, vol. 12, no. 8, p. 1102, 2001.

[56] G. Goldswain and J. Tapson, "Kernel ridge regression for volume fraction prediction in electrical impedance tomography," *Measurement Science and Technology*, vol. 17, no. 10, p. 2711, 2006.

[57] D. Barber, "A sensitivity method for electrical impedance tomography," *Clin Phys Physiol Meas.*, vol. 10, no. 3, pp. 368–371, Nov 1989.

[58] A. Adler and W. R. B. Lionheart, "Uses and abuses of EIDORS: an extensible software base for EIT," *Physiological Measurement*, vol. 27, no. 5, p. S25, 2006.

[59] C. Barber, B. Brown, and I. Freeston, "Imaging spatial distributions of resistivity using applied potential tomography," *Electronics Letters*, vol. 19, no. 22, pp. 933–935, October 1983.

[60] S. Smith, *The Scientist and Engineer's guide to digital signal processing.* California Technical Publishing, 1997.

[61] A. P. Calderón, "On an inverse boundary value problem," *Computational & Applied Mathematics*, vol. 25, pp. 133–138, 00 2006.

[62] W. R. Breckon and M. K. Pidcock, "Mathematical aspects of impedance imaging," *Clinical Physics and Physiological Measurement*, vol. 8, no. 4A, p. 77, 1987.

[63] T. J. Yorkey, J. G. Webster, and W. J. Tompkins, "Comparing reconstruction algorithms for electrical impedance tomography." *IEEE Trans Biomed Eng*, vol. 34, no. 11, pp. 843–52, Nov. 1987.

[64] G. Dreyfus, *Neural netowrks: methodology and applications.* Springer-Verlag, 2005.

[65] J. Freeman and D. Skapura, *Neural networks algorithms, applications, and programming techniques*, ser. Computation and Neural Systems. Addison Wesley, 1991.

[66] A. Adler and R. Guardo, "A neural network image reconstruction technique for electrical impedance tomography." *IEEE Trans. Med. Imaging*, vol. 13, no. 4, pp. 594–600, 1994.

[67] R. Guardo, C. Boulay, and M. Bertrand, "A Neural Network Approach To Image Reconstruction In Electrical Impedance Tomography," in *Engineering in Medicine and Biology Society, 1991. Vol.13: 1991., Proceedings of the Annual International Conference of the IEEE*, Oct 1991, pp. 14–15.

[68] M. Seymour and M. Tsoeu, "A mobile application for South African signl language (SASL) recognition," in *Proceedings of IEEE AFRICON*, 2015, pp. 1–5.

[69] C. Thornton, "Separability is a Learner's Best Friend," in *4th Neural Computation and Psychology Workshop, London, 9–11 April 1997*, ser. Perspectives in Neural Computing, J. Bullinaria, D. Glasspool, and G. Houghton, Eds. Springer London, pp. 40–46.

[70] J. Greene, "Feature subset selection using thornton's separability index and its applicability to a number or sparse proximity-based classifiers," 12^{th} *Annual Symposium of the South African Pattern Recognition Association*, 2001.

[71] I. Jolliffe, *Principal component analysis*. John Wiley and Sons Ltd., 2005.

[72] G.-B. Huang, Q.-Y. Zhu, and C.-K. Siew, "Extreme learning machine: Theory and applications," *Neurocomputing*, vol. 70, no. 1–3, pp. 489–501, 2006, neural NetworksSelected Papers from the 7th Brazilian Symposium on Neural Networks (SBRN '04)7th Brazilian Symposium on Neural Networks.

[73] M. Egmont-Petersen, D. de Ridder, and H. Handels, "Image processing with neural networks—a review," *Pattern Recognition*, vol. 35, no. 10, pp. 2279–2301, 2002.

[74] Y. Sun, "Hopfield neural network based algorithms for image restoration and reconstruction. I. Algorithms and simulations," *Signal Processing, IEEE Transactions on*, vol. 48, no. 7, pp. 2105–2118, Jul 2000.

[75] R. Steriti and M. Fiddy, "Regularized image reconstruction using SVD and a neural network method for matrix inversion," *Signal Processing, IEEE Transactions on*, vol. 41, no. 10, pp. 3074–3077, Oct 1993.

[76] Q. Marashdeh, W. Warsito, L.-S. Fan, and F. L. Teixeira, "A nonlinear image reconstruction technique for ECT using a combined neural network approach," *Measurement Science and Technology*, vol. 17, no. 8, p. 2097, 2006.

[77] A. S. Miller, B. H. Blott, and T. K. Hames, "Neural networks for electrical impedance tomography image characterisation," *Clinical Physics and Physiological Measurement*, vol. 13, no. A, p. 119, 1992. [Online]. Available: http://stacks.iop.org/0143-0815/13/i=A/a=023

[78] V. Srinivasan, Y. Han, and S. Ong, "Image reconstruction by a Hopfield neural network," *Image and Vision Computing*, vol. 11, no. 5, pp. 278–282, 1993. [Online]. Available: http://www.sciencedirect.com/science/article/pii/0262885693900052

[79] A. Adler and R. Guardo, "A neural network image reconstruction technique for electrical impedance tomography," *IEEE Transactions on Medical Imaging*, vol. 13, no. 4, pp. 594–600, Dec 1994.

[80] E. Ratajewicz-Mikolajczak, G. Shirkoohi, and J. Sikora, "Two ANN reconstruction methods for electrical impedance tomography," *Magnetics, IEEE Transactions on*, vol. 34, no. 5, pp. 2964–2967, Sep 1998.

[81] J. Lampinen and A. Vehtari, "Application of Bayesian neural network in electrical impedance tomography," in *Proceedings of 11th Scandinavian Conference on Image Analysis SCIA'99*, 1999, pp. 87–93.

[82] T. Sun, R. Mudde, J. Schouten, B. Scarlett, and C. van den Bleek, "Image reconstruction of an electrical capacitance tomography system using an artificial neural network," in *1st World Congress on Industrial Process Tomography*, April 1999, pp. 174–180.

[83] C. Wang, J. Lang, and H. Wang, "RBF neural network image reconstruction for electrical impedance tomography," in *Machine Learning and Cybernetics, 2004. Proceedings of 2004 International Conference on*, August 2004, pp. 2550–2552.

[84] P. Wang, L. J.S., and W. M., "An image reconstruction algorithm for electrical capacitance tomography based on simulated annealing particle swarm optimization," *Journal of applied research and technology*, vol. 13, pp. 197–204, 00 2015. [Online]. Available: http://www.scielo.org.mx/scielo.php?script=sci_arttext&pid=S1665-64232015000200005&nrm=iso

[85] S. Martin and C. T. M. Choi, *Electrical Impedance Tomography: A Reconstruction Method Based on Neural Networks and Particle Swarm Optimization*. Cham: Springer International Publishing, 2015, pp. 177–179. [Online]. Available: http://dx.doi.org/10.1007/978-3-319-12262-5_49

[86] J. Borish and J. B. Angell, "An Efficient Algorithm for Measuring the Impulse Response Using Pseudorandom Noise," *J. Audio Eng. Soc*, vol. 31, no. 7/8, pp. 478–488, 1983.

[87] E. Kamen and B. Heck, *Fundamentals of Signals and Systems Using the Web and MATLAB*. Prentice Hall, 2000.

[88] J. Schwarzenbach and K. F. Gill. Edward Arnold Publishers Ltd, 1978.

[89] P. Hua, E. Woo, J. Webster, and W. J. Tompkins, "Iterative reconstruction methods using regularization and optimal current patterns in electrical impedance

tomography," *Medical Imaging, IEEE Transactions on*, vol. 10, no. 4, pp. 621–628, Dec 1991.

[90] P. J. Riu and D. Anton, "Performance assessment of EIT measurement systems," *Journal of Physics: Conference Series*, vol. 224, no. 1, p. 012015, 2010.

[91] M. Yasin, S. Böhm, P. O. Gaggero, and A. Adler, "Evaluation of EIT system performance," *Physiological Measurement*, vol. 32, no. 7, p. 851, 2011.

[92] T. I. Oh, K. H. Lee, S. M. Kim, H. Koo, E. J. Woo, and D. Holder, "Calibration methods for a multi-channel multi-frequency EIT system," *Physiological Measurement*, vol. 28, no. 10, p. 1175, 2007.

[93] A. McEwan, G. Cusick, and D. S. Holder, "A review of errors in multi-frequency EIT instrumentation," *Physiological Measurement*, vol. 28, no. 7, p. S197, 2007.

[94] L. Fabrizi, A. McEwan, T. Oh, E. J. Woo, and D. S. Holder, "A comparison of two EIT systems suitable for imaging impedance changes in epilepsy," *Physiological Measurement*, vol. 30, no. 6, p. S103, 2009.

[95] R. J. Yerworth, R. H. Bayford, B. Brown, P. Milnes, M. Conway, and D. S. Holder, "Electrical impedance tomography spectroscopy (EITS) for human head imaging," *Physiological Measurement*, vol. 24, no. 2, p. 477, 2003.

[96] D. Knuth, *The art of computer programming*, 2nd ed., ser. Computer Science and Information Processing. Addison Wesley, 1981, vol. 2.

[97] D. Sarwate and M. Pursley, "Crosscorrelation properties of pseudorandom and related sequences," *Proceedings of the IEEE*, vol. 68, no. 5, pp. 593–619, May 1980.

[98] R. Gold, "Optimal binary sequences for spread spectrum multiplexing (Corresp.)," *Information Theory, IEEE Transactions on*, vol. 13, no. 4, pp. 619–621, October 1967.

[99] S. Glisic, *Adaptive WCDMA: Theory and Practice*. John Wiley and Sons Ltd., December 2002.

[100] ——, *Advanced wireless communications: 4G cognitive and cooperative broadband*. John Wiley and Sons Ltd., 2007.

[101] D. S. Holder, "Electrical impedance tomography (EIT) of brain function," *Brain Topography*, vol. 5, no. 2, pp. 87–93.

[102] X. Yue and C. McLeod, "FPGA desing and implementation for EIT data acquisition," *Physiol. Meas.*, vol. 29, no. 2008, pp. 1233–1246.

[103] B. Miao, R. Zane, and D. Maksimovic, "System identification of power converters with digital control through cross-correlation methods," *Power Electronics, IEEE Transactions on*, vol. 20, no. 5, pp. 1093–1099, Sept 2005.